FORMATION OF CALCIUM PHASES IN THE POLYCRYSTALLINE α-ALUMINA CERAMICS

by

FOROUGH MAHDIPOUR

Submitted to the Graduate School of Engineering and Natural Sciences in partial fulfillment of the requirements for the degree of Master of Science

Sabanci University

December 2022

ABSTRACT

FORMATION OF CALCIUM PHASES IN THE POLYCRYSTALLINE α-ALUMINA CERAMICS

FOROUGH MAHDIPOUR

Materials Sciences and Nano Engineering, Master Thesis, December 2022

Supervisor: Prof. Dr. Mehmet Ali Gülgün

***Keywords*:** Alpha-Alumina, Calcium Hexa-Aluminate, Ca Doped Alumina, Grain Boundary Segregation, Formation Mechanisms, Diffusion

The distribution of impurities, intergranular films, and second-phase particles, in addition to the composition and structure of the phases, all influence the characteristics of ceramic materials. Changes in the microstructure of calcium doped α-Al2O3 (alumina) with increasing sintering temperatures of 1300°C, 1400°C, and 1550°C were studied using electron microscopy techniques. To find the early stages of formation of calcium hexaaluminate, the sintering process was also performed for the calcium-doped alumina samples at 1300°C for various sintering time ranges between 1h to 10 h. A first principle calculation was done after studying the phase composition and microstructure evolution of the sintered specimen. Variations in the average grain sizes were related to the excess calcium concentrations (Γ_{Ca}). Analytical electron microscopy was used to study these calcium doped alumina ceramics. The alumina grains were homogeneous and equiaxed at all sintering conditions. As the sintering time and temperature increased, the calcium-

rich grain morphologies elongated. An X-ray energy dispersive spectrometer attached to a scanning electron microscope showed the precipitation of calcium-rich second phases. These precipitates were identified as different calcium aluminate phases like mono calcium aluminate (CA), calcium dialuminate (CA_2), and calcium hexaluminate (CA_6) by X-ray energy dispersive analysis. Calcium precipitates at high temperatures appeared to be large and elongated grains. On the other hand, at low sintering times, tiny grains were detected as the calcium rich grains. The results demonstrate that a small amount of CA_6 forms at 1300°C in the reaction system of Al_2O_3 doped with Ca sintered for 4 h, and more significant amounts form at higher times and temperatures. The reaction of formation mechanism is as regards: $CaO.2Al_2O_3$ (CA_2) combines with $4Al_2O_3$ results in CA_6. According to the $CaO\text{-}Al_2O_3$ phase diagram, there is a diffusion process of Al^{3+} cations in Al_2O_3 towards CA_2 to generate CA_6.

ÖZET

POLİKRİSTALİN α-ALÜMİNA SERAMİKLERDE KALSİYUM FAZLARININ OLUŞUMU

FOROUGH MAHDIPOUR

Malzeme Bilimi ve Nano-mühendislik, Yüksek Lisans Tezi, Aralık 2022

Danışman: Prof. Dr. Mehmet Ali Gülgün

***Anahtar Kelimeler*:** Alfa-Alümina, Kalsiyum Heksa-Alüminat, Ca Katkılı Alümina, Tane Sınır Ayrımı, Oluşum Mekanizmaları, Difüzyon

Seramik malzemelerin özellikleri sadece bileşim tarafından belirlenmez ve mevcut fazların yapısı, aynı zamanda safsızlıkların dağılımı, taneler arası filmler ve ikinci aşamalar.kalsiyum katkılı α-Al_2O_3'ün (alümina) mikro yapısındaki değişiklikleri, 1300°C, 1400°C ve 1550°C'lik artan sinterleme sıcaklıkları elektron mikroskobu teknikleri kullanılarak incelenmiştir. Kalsiyum hekzaalüminat oluşumunun erken aşamalarını bulmak için, kalsiyum katkılı alümina numuneleri için de 1300°C'de 1 saat ile 10 saat arasında çeşitli sinterleme zaman aralıklarında sinterleme yapılmıştır. Sinterlenmiş numunenin faz bileşimi ve mikroyapı evrimi incelendikten sonra ilk prensip hesaplaması yapıldı. Ortalama tane boyutlarındaki değişimler aşırı kalsiyum konsantrasyonları (Γ_{Ca}) ile ilişkilidir. Bu kalsiyum katkılı alümina seramikleri incelemek için analitik elektron mikroskobu kullanıldı. Tüm sinterleme koşullarında, alümina taneleri üniform ve eş eksenlidir. Kalsiyumca zengin tane morfolojileri, sinterleme süresi

ve sıcaklık arttıkça uzadı. Bir taramalı elektron mikroskobuna bağlı bir X-ışını enerji dağılım spektrometresi, kalsiyum açısından zengin ikinci fazların çökeldiğini gösterdi. Bu çökeltiler, X-ışını enerji dağılım analizi ile mono kalsiyum alüminat (CA), kalsiyum dialüminat (CA_2) ve kalsiyum hekzalüminat (CA_6) gibi farklı kalsiyum alüminat fazları olarak tanımlandı. Yüksek sıcaklıklarda kalsiyum çökeltileri büyük ve uzun taneler olarak ortaya çıktı. Öte yandan, düşük sinterleme sürelerinde, kalsiyum bakımından zengin taneler olarak küçük taneler tespit edildi. Sonuçlar, Ca_6 katkılı Al_2O_3'ün 4 saat boyunca sinterlenmiş reaksiyon sisteminde 1300°C'de az miktarda CA_6 oluştuğunu ve daha önemli miktarların daha yüksek süre ve sıcaklıklarda oluştuğunu göstermektedir. Oluşum mekanizmasının reaksiyonu şu şekildedir: $4Al_2O_3$ ile $CaO.2Al_2O_3$ (CA_2), CA_6 ile sonuçlanır. $CaO\text{-}Al_2O_3$ faz diyagramına göre Al_2O_3 içindeki Al^{3+} katyonlarının CA_2'ye doğru difüzyonu CA_6'yı oluşturur.

ACKNOWLEDGMENTS

There are no words to express my honest appreciation and respect for my thesis advisor, Prof. Dr. Mehmet Ali Gülgün (Mali hoca), for his inspiration and constant encouragement. For teaching me how to conduct research and introducing me to the world of ceramics. I have learned so much from him that broadened my vision in both my academic and personal life.

Besides my supervisor, I would like to thank the rest of my thesis committee: Prof. Dr. Burç Mısırlıoğlu and Prof. Dr. Sedat Alkoy. They kindly took their time to give me constructive feedback on my work.

Special thanks must go to Dr. Pelin Sungur for fruitful discussions during this study and for passing me a bit of her excellent knowledge on the transmission electron microscope.

I am most grateful to the collaborators from the ceramic group for providing me with their knowledge and insight to solve my technical and scientific problems: Dr. Pozhhan, Kosar, Dr. Sirous, Dr. Eymen, Darya, Melike, Mehmet Can, Dr. Ali, Mohammed, Yasemin, and Karya. It was my pleasure to be a member of such a strong research team with a pleasant research and fun environment.

I am grateful to our thoughtful laboratory specialists, Bilge Esenkel, Cansu Yılmaz Baker, and Anıl Tez, who were always available to help.

I cannot forget my friends from Sabanci University who supported me during difficult times, cheered me on, and celebrated each success: Meryem Çiğdem, Gizem, Aybüke Buşra, Gülşah, Faezeh, Maryam, Beril, Mahdiyeh, and Negar.

My special thanks go to Hana, the one true friend with her kindness, encouragement, and support during this marathon.

I would like to thank my parents-in-law, Baba Mazaher and Maman Zohreh, for their emotional support. I also thank my brother-in-law's family for all their love: Dadash Amir, Behnaz, and their lovely daughter Mehraein.

I sincerely thank my parents, Baba Mahdipour and Maman Rafieh, for their unconditional trust, encouragement, and endless patience. It was their love that raised me when I got wearied. Thanks to my one and only brother Farzin and his wife, Fayezeh, for their support, and endless love.

Finally, I extend my sincere gratitude to my fiance, Ardeshir. My best friend and closest one, who knows me best, has loved, supported, and assisted me in the best way possible in getting through this challenging time.

To the Innocent Victims of Iran Revolution 1401

For

*"**Woman, Life, Freedom**"*

TABLE OF CONTENTS

LIST OF TABLES

LIST OF FIGURES

LIST OF SYMBOLS

T	Temperature
T_m	Melting temperature
hr	Hour
X_t	Total concentration of dopant ion
X_t^*	Bulk solubility limit
A	Total interface area
S_V	Total grain boundary area
Ω	Volume per cation in α-alumina
S	Entropy
V	Volume
D	Mean grain diameter
G	Grain size
C_0	Solute concentration in the bulk
C_{GB}	Grain boundary concentration
C_{Bulk}	Bulk concentration
V_{GB}	Grain boundary velocity
K	Partitioning coefficient
ΔG_{seg}	Gibbs free energy change due to segregation
k	Boltzman constant
Γ_C	Critical surface coverage
Γ_0	Planar density of available grain boundary sites for adsorption
Γ_Y	Yttrium excess concentration at the grain boundaries
Γ_{Ca}	Calcium excess concentration at the grain boundaries
D_{GB}	Atomic mobility diffusion coefficient
L	Mean linear intercept length
γ_{GB}	Grain boundary energy
μ	Micron

nm	Nanometer
mm	Millimeter
°C	Degrees Celsius
ρ	Density
Z	Atomic number
N_A	Avogadro‘s number
M_{GB}	Grain boundary mobility
M_P	Particle or pore mobility
n_A	Number of atoms
N_A	Avogadro’s number
N_Z	Particle or pore density at the grain boundary
α	Activity
O	Oxygen
r	Particle or pore radius
r_1, r_2	Radii of curvature perpendicular with each other at the interface between adjacent grains
CA_6	Calcium Hexaaluminate ($CaO.6Al_2O_3$,$CaAl_{12}O_{19}$)
CA_2	Calcium Dialuminate ($CaO.2Al_2O_3$, $CaAl_4O_7$)
CA	Calcium Aluminate ($CaAl_2O_3$)
C_2A	Dicalcium Aluminate ($Ca_2Al_2O_5$)
N_L	Mean number of intercepts
γA	Total interfacial energy
Δγ	Particle interfacial energy
ΔA	Interface area
γ	Surface/interface energy
U	Internal energy
μ_i	Chemical potential of species i,
Ni	Number of molecules of species i
ΔP	Pressure difference
μ_0	Standard chemical potential
c	Solubility,

p	Vapor pressure,
c_0	Equilibrium solubility
p_0	Equilibrium vapor pressure

LIST OF ABBREVIATIONS

α-Al_2O_3	Alpha alumina
β-alumina	Beta alumina
AGG	Abnormal grain growth
YAG	Yttrium alumina garnet
TEM	Transmission electron microscope
STEM	Scanning transmission electron microscope
HRTEM	High resolution transmission electron microscope
HAADF	High Angle Annular Dark Field
SAD	Selected Area Diffraction
AEM	Auger electron microscope
SEM	Scanning electron microscope
EDS	Energy dispersive spectrometer
ICP-OES	Inductively coupled plasma-optical emission spectroscopy
rpm	Revolution per minute
ppm	Part per million
%TD	Percent theoretical density
wt%	Weight percent
BF	Bright Field
BSE	Backscattered Electron
FIB	Focused Ion Beam
PIPS	Precision Ion Polishing System
JEMS	Java Electron Microscopy Software
CIF	Crystallographic Information File
CIP	Cold isostatic pressing
DP	Diffraction Pattern
DTG	Differential Thermogravimetry
GB	Grain Boundary

EDX	Energy Dispersion X-ray
Ar	Argon
ATM	Analytical Transmission Microscope
MP	Magnetoplumbite

1. INTRODUCTION

The microstructure of materials is crucial in determining their properties. The mechanical, optical, electrical, and dielectric properties of a material can be significantly influenced by insignificant amounts of impurities. The impact of calcium impurities in different temperatures on the microstructure of Al_2O_3 has been investigated in this thesis.

α-Alumina (α- Al_2O_3) is one of the most researched ceramic materials. Alumina is one of the rigids, most vital, and most abrasion-resistant oxides, making it ideal for abrasive materials, bearings, and cutting tools. Since alumina has a high electrical resistance, it is applied as a pure material and a component in electrical insulators and components. The optical transparency of alumina is also distinctive. It can be applied as high-temperature components, catalyst substrates, and biomedical implants due to its high melting temperature of 2,054°C, chemical stability, and reactivity. On the other hand, the usefulness of alumina is due to its high strength, melting temperature, abrasion resistance, optical clarity, and electrical resistivity.

The effects of impurities and dopants on sintering, microstructure, and in some cases, the migration rates of specific grain orientations of polycrystalline alumina have been a prominent issue for some time. Many studies have focused on the possible roles of dopants in promoting sintering and limiting grain growth, with particular emphasis on Ca. The segregation of dopants to grain boundaries influences sintering and grain growth, but the exact mechanism is still unclear. Specific dopants and impurities, such as Ca, Mg, and Si, have significantly affected the grain growth rate in polycrystalline alumina. The segregation of Ca to grain boundaries appears to increase grain boundary mobility. As a result, determining the solubility limit of dopants and impurities at sintering temperatures is crucial.

Furthermore, grain boundary mobility must be determined to link mobility and grain development kinetics in alumina. The primary goal of this research identifies the segregation of Ca in grain boundaries of α- Al_2O_3, which is necessary to determine the role of segregation in the evolution of alumina microstructures. To accomplish this,

polycrystalline alumina was sintered at a Ca concentration that resulted in two phases of Ca, $CaAl_4O_7$ and $CaAl_{12}O_{19}$, saturating the alumina grains with Ca, and then cooled in the furnace.

The current study investigated the formation of these two phases, crystal structure, and morphology of sintered polycrystalline alumina. The effect of sintering temperature on the formation of Ca phases is also studied.

1.1. Alumina

Alumina (Al_2O_3) is a very significant ceramic material, both as a pure material and as a component of ceramics and glass. It has been revealed that adding dopants to polycrystalline alumina establishes different microstructures. These additives can modify the alumina manufacturing process to obtain specific attributes [1]. Many metastable crystallographic structures exist in aluminum oxide. However, α-Al_2O_3 is the stable alumina structure with a rhombohedral (corundum) structure and a space group of $R3\overline{C}$ [2, 3]. For clarity, a hexagonal unit cell is generally used to describe α-alumina, which consists of 30 atoms [4]: 12 aluminum and 18 oxygen atoms, as illustrated in Figure 1.1 [5]. The lattice parameters of the hexagonal unit cell are a=b=0.4754 nm, c=12.99 nm, α=β=90˚, γ=120˚. Swanson et al. [6] calculated that the theoretical density of alumina is 3.97 gr/cm^3.

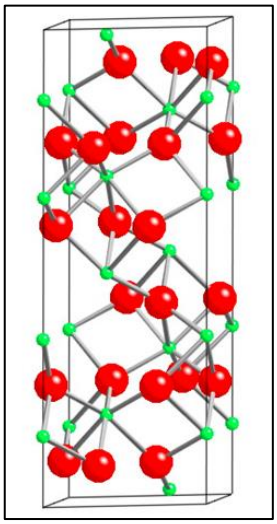

Figure 1. 1. The hexagonal unit cell illustrates the α-alumina crystal structure. O is shown by red circles, while green (small) circles express Al.

The density of metastable polymorphs of alumina structures is lower than corundum. Many other allotropic structures have been reported, but they have gotten less attention than the ones in Table 1.1. All these metastable polymorphs of alumina contain oxygen packings close to cubic. Typically, eta or gamma alumina are created at low temperatures and transform in the pattern gamma→delta→theta→alpha→alumina as temperature rises. The transformation mechanism and the pattern of phases can be driven by variables such as particle size, heating rate, impurities, and atmosphere. Only the alpha phase (corundum) is generally prevalent at above 1,200°C.

Table 1. 1. Structures of stable alumina (corundum) and unstable alumina.

		Lattice parameters, (Angle °A)		
Designation	Structure	a	b	C
Corundum	Hexagonal(rhombohedral)	4.758		12.991
Eta	Cubic (spinal)	7.90		
Gamma	Tetragonal	7.95		7.79
Delta	Tetragonal	7.97		23.47
Theta	Monoclinic	5.63	2.95	11.86
Kappa	Orthorhombic	8.49	12.73	13.39

For many years, alumina has been studied as a concept for oxide ceramics. The effect of additives and impurities on sintering, grain growth, and microstructure-dependent properties has received significant attention [7-9]. It has been demonstrated that adding specific dopants induces polycrystalline alumina to establish different microstructures. Therefore, these additives can be used to develop the alumina manufacturing process to attain unique features [10]. Various scientists have intensively investigated the influences of numerous impurities including Si, Ca, Mg, and Y on the microstructure of α-alumina for many years. One of the most common impurities in alumina is calcium, which is thought to influence interface-related behaviors like sintering, intergranular fracture, and grain growth.

1.2. The Crystallography of α-Al_2O_3

The crystal structure of α-Al_2O_3 generally exhibits O^{2-} anions in an estimated hcp structure with Al^{3+} cations filling two-thirds of the octahedral interstices, as symbolized in Figure 1.2.

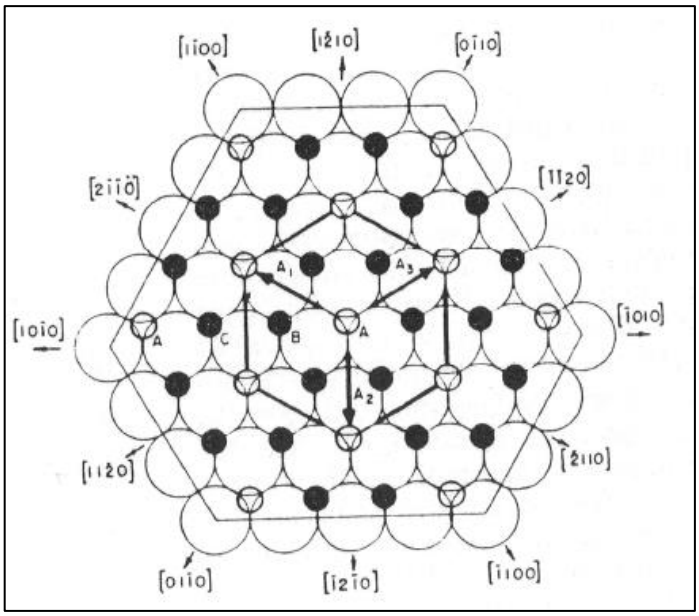

Figure 1. 2. The basal plane of sapphire shows the hexagonal close-packed anion sublattice and the cations occupying two-thirds of the octahedral interstices.

The corners of the unit cell are described using the empty sites of the cation sublattice, as represented in Figure 1.3 [5].

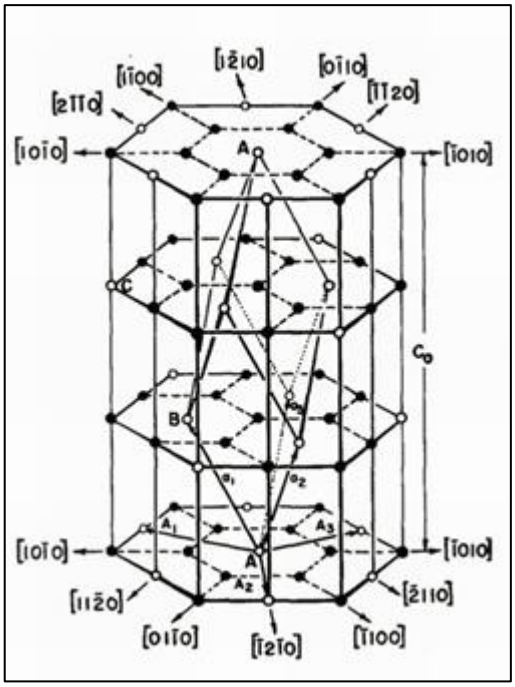

Figure 1. 3. The cation sublattice in sapphire. The vacant octahedral sites define the corners of a morphological unit cell.

In alumina, impurities predominantly segregate into different planes. As a result, discussing the common crystallographic planes in sapphire is also necessary. Planes in

sapphire are displayed in Figure 1.4. Moreover, the names, Miller indices, and d spacing of these planes are provided in Table 1.2 [11].

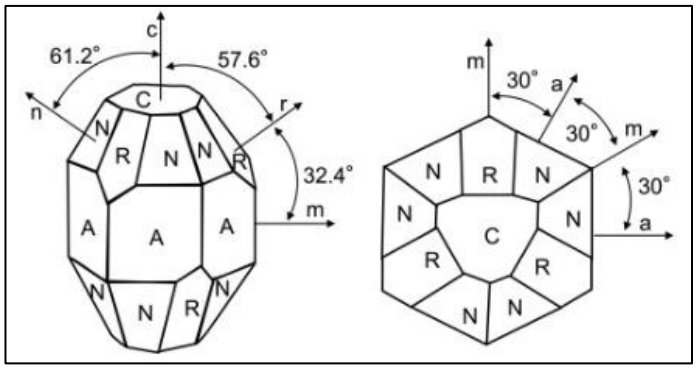

Figure 1. 4. Labeling of planes in hexagonally symmetric sapphire. The left panel shows the view along the c-axis, while the right panel shows the surface planes.

Table 1. 2. Specifications of the common crystallographic planes in sapphire

Plane	Plane name	Miller indices	d spacing
a	prismatic	$[1\bar{1}20]$	2.379
c	basal	[0001]	2.165
m	prismatic	$[10\bar{1}0]$	1.375
n	n	$[1\bar{1}23]$	1.147
r	rhombohedral	$[\bar{1}102]$	1.740
s	pyramidal	$[10\bar{1}1]$	1.961

Generally, the basal and the rhombohedral have the lowest energies [12].

1.3. Calcium Di-aluminate ($CaAl_4O_7$, $CaO.2Al_2O_3$, CA_2)

In 1937, two separate studies reported the discovery of a new compound, $CaO.2Al_2O_3$ [13]. Goldsmith [14] reported in 1948 that CA_2 is monoclinic based on X-ray diffraction data, while optical characteristics suggested that the compound should be hexagonal or tetragonal. For many years, the exact crystal structure of the CA_2 was a point of conflict. Boyko and Wisnyi [15] claimed that CA_2 crystallizes as a monoclinic structure with the space group C2/c, while Cockayne and Robertson [16] asserted that this phase is complex hexagonal. The monoclinic structure was eventually confirmed by Goodwin and Lindop [17], and the findings of that investigation have since 1970 remained as the accepted crystal data for CA_2. Tables 1.3 and 1.4 contain the structural information for CA_2 and

the atomic locations in the crystal. Figure 1.5 depicts the CA_2 unit cell projected in the [001] and [010] directions.

Table 1. 3. Structural information of the CA_2

Formula: $CaO.2Al_2O_3$	**Lattice Parameters**
Space Group: C2/c	a=12.8398 Å
Volume: 591.54 $Å^3$	b=8.8624 Å
# of formula units/unit cell: 4	c=5.4311 Å
Density: 2.915 g/cm^3	α= γ=90° β =106°

Table 1. 4. Atomic locations in the CA_2 crystal

Atom	Coordination	x	y	z
A(1)	4	0.16410	0.08670	0.30300
A(2)	4	0.11980	0.44060	0.24100
Ca	6	0	0.80910	0.25000
O(1)	4 Al	0	0.52310	0.25000
O(2)	2 Al + 2 Ca	0.11550	0.05120	0.56590
O(3)	2 Al + 1 Ca	0.11850	0.25530	0.14910
O(4)	3 Al	0.19240	0.44360	0.57970

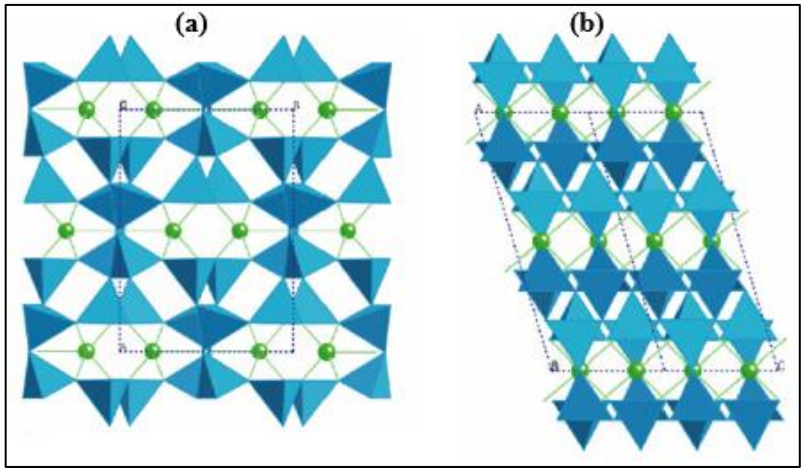

Figure 1. 5. Projection of the CA_2 unit cell on the: (a) [001] direction, (b) [010] direction. The green atoms represent the Ca_{2+} ions and blue atoms represent the Al^{3+} ions.

The mineral grossite, which contains CA_2, is found in nature. In 1977, Schulamit Gross [18] identified grossite in argillaceous limestone, 40 years after the initial reports of synthesized CA_2. The International Mineralogical Society (IMA) did not approve the

mineral until 1994, when Weber and Bishoff [19, 20] reported detecting it in meteorites and terrestrial rocks.

1.4. Calcium Hexa-Aluminate ($CaAl_{12}O_{19}$, $CaO.6Al_2O_3$, CA_6)

At the high-alumina end of the binary phase diagram, CA_6 is a stable aluminate [21]. As the mineral hibonite, it can also be found in nature. Paul Hibon, who found the mineral in 1956, gave it the name “Hibonite”.

Kato and Saalfeld [22] examined the crystal structure of CA_6 and determined that it is similar to that of the mineral magnetoplumbite (MP) [23, 24]. The MP structure is quite similar to the β-alumina structure [25, 26]. Both of these structures are layered structures formed of alternate layers of interspinel and blocks of spinel. Spinel blocks have the same rigid structure as spinel and are formed of Al^{3+} and O^{2-} ions. The interspinel layer, which is also a mirror plane, is responsible for contain cations such as Na^+ and K^+ in the β-alumina structure and Pb^{2+} and Ca^{2+} in the MP structure. The types and configurations of the ions within the interspinel layer are the main distinction between MP and β-alumina. This layer in MP includes $3O^{2-}$ ions and a large cation such as Ba^{2+} or Ca^{2+}. However, in β-alumina there is only one O^{2-} ion and one Na^+ and K^+ ion. Figure 1.6 compares the mirror planes of these two structures and the 3D schematic of the unit cells for these two systems.

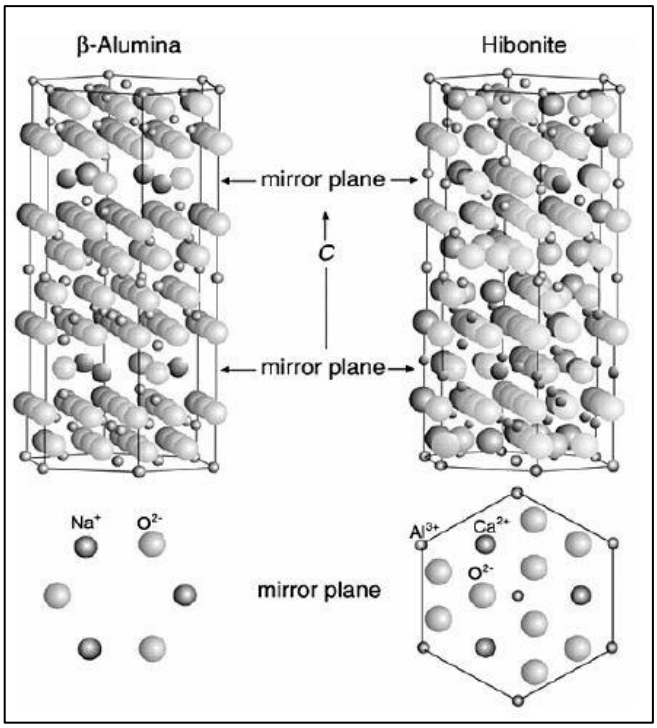

Figure 1. 6. Illustration of the unit cell and mirror plane of β-Al_2O_3 and hibonite.

CA_6 has a hexagonal space group $P6_3/mmc$ structure and can be expressed symbolically as $CaAlO_3[Al_{11}O_{16}]$. The interspinel layer is the area between the brackets, which symbolizes the spinel block. The Ca ions are dodecahedrally (12-fold) coordinated in the interspinel layer of the CA_6 structure. Al ions are dispersed throughout three octahedral, one tetrahedral, and one bipyramidal crystallographically independent sites. The split atom concept was initially applied to describe the accurate position of the Al atom in the trigonal bipyramidal site [27]. Al^{3+} was found to occupy statistically one of the two equivalent sites that are displaced from the mirror plane [27]. The atomic locations with the coordinations and structural details of the CA_6 crystal are provided in Tables 1.5 and 1.6, respectively. Figure 1.7 also displays projections of the CA_6 structure in the $[01\bar{1}0]$ direction to display the arrangement of the layers and the atomic coordination numbers.

Table 1. 5. Structural information of the CA_6 crystal

Formula: $CaO.6Al_2O_3$	**Lattice Parameters**
Space Group: $P6_3/mmc$	a=5.5587 Å
Volume: 585.83 $Å^3$	c=21.8929 Å
# of formula units/unit cell: 2	α=β=90°
Density: 3.79 g/cm^3	γ=120°

Table 1. 6. Atomic locations in CA_6 crystal.

Atom	Position (Wykchoff)	Coordination	x	y	z
A(1)	2a	6	0	0	0
A(2)	4e	4	0	0	0.25771
A(3)	4f	4	0.33333	0.66667	0.02808
A(4)	4f	6	0.33333	0.66667	0.19102
A(5)	12k	6	0.16855	0.33710	0.89086
Ca	2d	12	0.66667	0.33333	0.25000
O(1)	4e	4 Al	0	0	0.14907
O(2)	4f	4 Al	0.66667	0.33333	0.05461
O(3)	6h	4 Al	0.18107	0.36214	0.25000
O(4)	12k	4 Al	0.15505	0.31010	0.05213
O(5)	12k	3 Al+ 1 Ca	0.50325	0.00650	0.14912

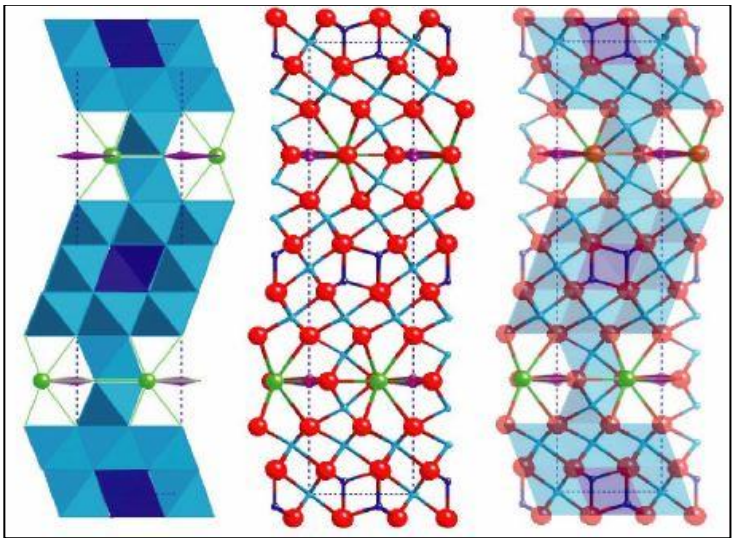

Figure 1. 7. The projection of the [01$\bar{1}$0] direction of CA_6 unit cell. There are two models presented: ball-stick and polyhedral. To show how these models relate to one another, they are also superimposed. O^{2-}ions are represented by red atoms, Ca^{2+} ions are given by green atoms, and Al^{3+} ions are shown by blue and purple atoms.

1.5. Sintering

Sintering is the process of compacting particles into a single dense solid by providing thermal energy to a powder (typically $0.5T_m<T<0.8T_m$), which helps to improve

mechanical characteristics such as strength, electrical conductivity, and thermal conductivity. In ceramics, to form the dense solids, small powders are frequently milled, mixed, and shaped into the aimed shape using some techniques. A powder compact is heated during the sintering process, which converts it into a hard, dense ceramic form. It is a complicated principle in which many mechanisms work concurrently. Since the driving force for sintering is small, reaching full density during the process is not easy. Sintering is the final stage of the process in which the green body is heated to higher temperatures, resulting in a dense and packed ceramic material with fewer pores.

1.5.1. Solid State Sintering

Sintering can happen with or without a liquid phase. The compositions and firing temperatures utilized in liquid phase sintering are applied so that some liquid is formed during the process. The process is known as solid-state sintering in the absence of a liquid phase. Densification of a green body by solid-state sintering is accomplished through particle shape changes and mass transport. The reduction of total surface/interfacial energy is the driving force for pore densification and shrinkage throughout the sintering. The driving force can be represented as follows [28].

$$\Delta(\gamma A) = \Delta\gamma A + \gamma\Delta A \qquad (1.1)$$

Where γ is the surface/interface energy, and A is the total interface area, generating γA as the total interfacial energy of the compacted green body. The total interfacial energy (γA) can be decreased by either densification, which results in a reduction of particle interfacial energy (Δγ) by displacing free surfaces with grain boundaries, or grain coarsening, which results in a drop of interface area (ΔA) (see Figure 1.8.).

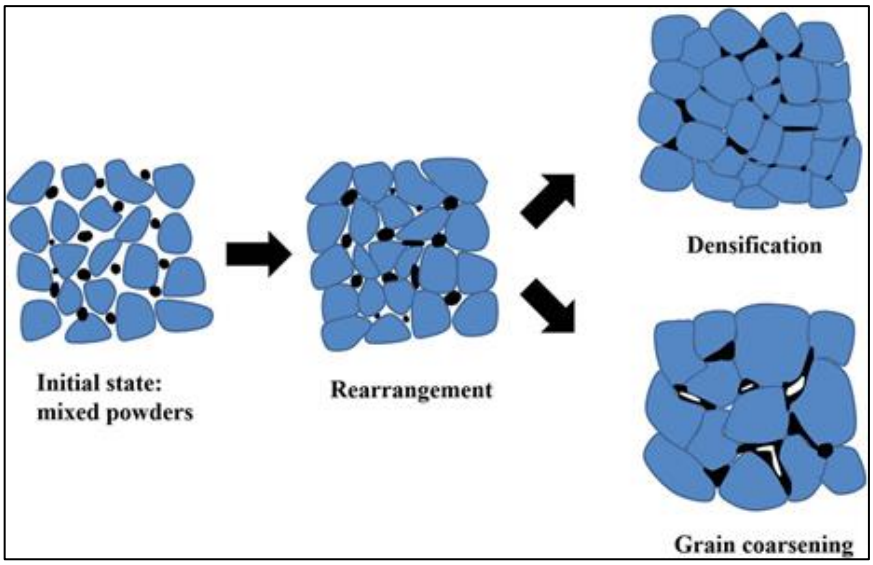

Figure 1. 8. Schematic of two possible paths whereby an accumulation of particles can reduce its energy. (a) Densification, accompanied by grain growth. (b) Coarsening, in which large grains grow at the expense of smaller ones.

Densification and coarsening are completive processes that can happen at the same time [29]. Densification is a process that removes solid-vapor interfaces while forming new low-energy solid-solid interfaces as particle interfacial energy decreases [30].

Grain coarsening occurs as a result of Ostwald ripening [31], a concept in which large particles grow at the expense of smaller ones, as clarified by Hillert [32] and defined as the von Neumann - Mullins equation [33], which leads to a reduction in the interface area ΔA.

$$\frac{ds}{dt} = \frac{\pi M_{GB} \gamma_{GB}}{3} (n - 6) \qquad (1.2)$$

Where s is the total area of the grain and n is the number of grain neighbors, M_{GB} is the grain boundary mobility, and γ_{GB} is the grain boundary energy.

If densification is the overall process, the compact shrinks and the pores gradually become smaller and disappear. Density rises because of pore shrinkage and initial pore annihilation. If coarsening is apparent, both particles and pores will grow over time. Full density is derived only when the atomic functions correlated with ripening are inhibited. In general, a solid-state sintered ceramic is an ambiguous material with retained porous and grains that are substantially larger than the initial particle sizes. Barsoum [29] explained the significant aspects affecting solid-state sintering as follows.

Temperature: Because sintering is caused by diffusion, increasing the temperature accelerates sintering kinetics. Bulk diffusion typically has higher activation energies than surface and grain boundary diffusion. Consequently, raising the temperature dramatically improves the bulk diffusion processes that increase the density.

Green density: There is generally a relationship between the green (pre-sintering) density and the final density, as the higher the density, the less pore volume that must be eliminated.

Green microstructure homogeneity: The uniformity of the green microstructure and the lack of agglomerates are more critical than the green density.

Atmosphere: The influence of the atmosphere on the compaction of a powder can be crucial. The diffusivity of a species that regulates rate is often increased by the atmosphere. In other circumstances, the existence of a specific gas can enhance ripening by increasing the vapor pressure and completely suppressing densification.

Impurities: Impurity roles have been widely researched, and the following influences have been clarified:

1. Sintering facilitates: The additive is added to create a liquid phase.
2. Reduce coarsening by raising surface diffusion and reducing the evaporation rate.
3. Prevent grain growth and decrease grain boundary mobility.
4. Accelerate the rate of diffusion.
5. Size dispersion: Narrow size distributions reduce the possibility of abnormal grain growth (AGG).

Particle size: Because the surface area reduction is the driving force for densification, the driving power increases with primary surface area. Moreover, there are several other problems when using very small particles. Electrostatic and other surface forces get stronger when the particle surface to volume ratio rises, eventually causing agglomeration. Agglomerates have the potential to sinter together into greater particles when heated, dispersing the driving force for densification. Consequently, between the slightly sintered agglomerates, huge pores form that are hard to eradicate.

1.5.2. Driving Force for Sintering

The fact that the interfaces are not flat but curved significantly impacts the rates of sintering and coarsening. A pressure difference between the inside and outside of an equilibrium particle is a severe problem. In the following equation, k is shown as the curvature of a curved interface.

$$k = (\frac{1}{r_1} + \frac{1}{r_2}) \tag{1.3}$$

Where r_1 and r_2 are the curvature radii perpendicular to each other at the interface. The sign for curvature is considered negative for concave surfaces and positive for convex surfaces. The temperature and chemical potentials are the same at equilibrium, but the pressure across the interface is different. The Gibbs equation [34] for the energy of a phase interface is illustrated in equation (1.4):

$$dU = TdS - P^{\alpha}dV^{\alpha} - P^{\beta}dV^{\beta} + \sum_i \mu_i\left(dN_i^{\alpha} + dN_i^{\beta}\right) + \gamma dA \tag{1.4}$$

Here U is the internal energy, T is the temperature, S is the entropy, V is the volume, A is the area of the interface, and μ_i and Ni are the chemical potential and number of molecules of species i, respectively. The total volume and entropy are fixed in equation (1.4), resulting in dU=TdS=0. It is essential to mention that the number of molecules in the system $dN_i^{\alpha}+dN_i^{\beta}=0$ must be conserved, and the interface area is $A=4\pi r^2$. When equation (1.4) is rearranged, it produces:

$$P^{\beta} - P^{\alpha} = \Delta P = \gamma(\frac{1}{r_1} + \frac{1}{r_2}) \tag{1.5}$$

ΔP denotes the pressure difference between adjacent grains, also known as the Young-Laplace equation. For clarity, we will suppose a spherical particle with $r_1=r_2$, and equation (1.5) can be described as follows:

$$\Delta P = \frac{2\gamma}{r} \tag{1.6}$$

This formula is referred to as the Gibbs-Thomson equation [35]. It links the pressure difference at an interface to the surface tension and curvature of the interface. Consequently, the migration of atoms from convex to concave regions, or migration of vacancies from concave to convex regions, is the driving force for solid-state sintering.

1.5.3. Mass Transfer Mechanisms

During the sintering process, mass is transferred from high chemical potential regions (described as sources) to lower potential chemical regions (defined as sinks or necks) via diffusion. Figure 1.9 illustrates the various methods for a simple model of three spherical particles [36]. In a powder compact, there are five atomic paths by which mass can be transported [29].

1. Surface diffusion
2. Lattice/volume diffusion: Mass can move from the surface to the neck or from the grain boundary to the neck.
3. Evaporation-condensation: Through a gas phase to the neck.
4. Grain boundary diffusion: Mass can also transfer within the particle volume or from the grain boundary.
5. Viscous or creep flow: This mechanism can result in plastic deformation or the viscous migration of particles from high-stress regions to low-stress regions, which can lead to densification.

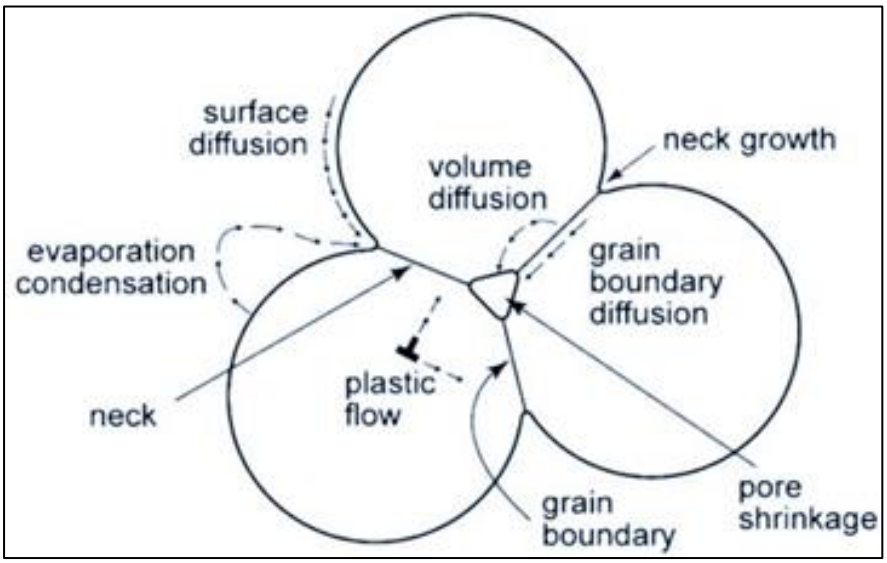

Figure 1. 9. Material transport paths during sintering.

1.5.4. Densification Mechanisms

It appears that not all the mechanisms are involved in the densification of the materials. Surface diffusion, lattice/volume diffusion, and evaporation-condensation mechanisms do not reduce the distance between particle centers. Thus, they do not cause shrinkage or densification but cause neck growth. Because of their impact on the curvature, which is the driving force for sintering, these mechanisms cannot be overlooked. Porosity must be reduced for densification to occur, which can be accomplished through grain boundary diffusion, lattice/volume diffusion from the grain boundary to the neck, or viscous flow from the volume of the particle to the neck. As illustrated in Figure 1.10, densification is conducted by changing the shape of the holes and the size of the pores [30].

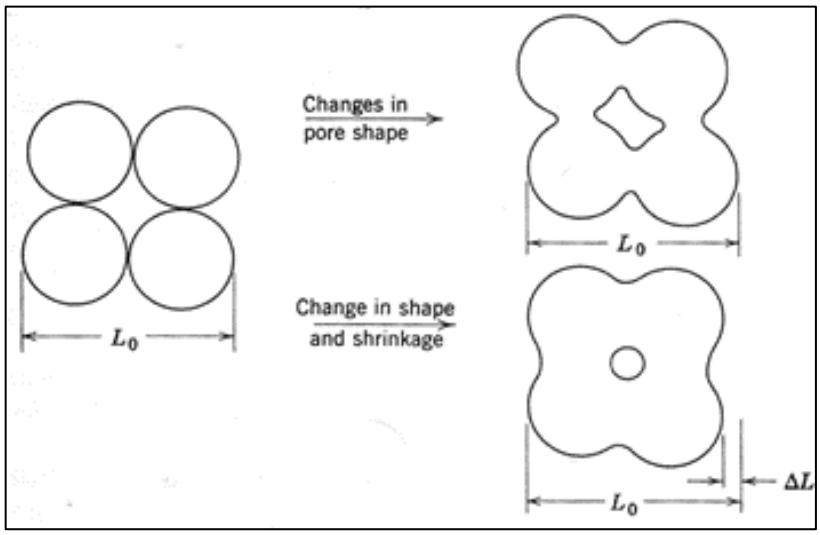

Figure 1. 10. Effect of change in pore shape and size on shrinkage.

1.6. Grain Growth

In addition to eliminating pores during the final stages of sintering, grain growth causes a general coarsening of the microstructure. The average grain size increases throughout time as little grains are devoured by larger grains during this process. For two reasons, it is crucial to manage and interpret the processes that lead to grain growth. The first is

linked to particle size, which is critical for controlling several ceramic properties, including the mechanical, electrical, magnetic, and optical features. Second reason is associated with preventing abnormal growth, the procedure by which a few grains surpass their normal size.

1.6.1. Grain Boundary Migration

Grain growth is a process that involves the migration of grain boundary (GB) to reduce the overall grain boundary area and, thus, the total free energy of a system. To conserve volume, the total number of grains must reduce as the grain growth causes an increase in average grain size. The rate of grain disappearance can be evaluated as a primary way to look at grain growth. There is a change in atomic chemical potential over a curved grain boundary which causes the boundary to migrate into the center of curvature [37]. Compared to a planar surface, a change in vapor pressure or solubility across a curved surface is one effect of the pressure differential. The curved surface applies pressure on the liquid or solid, increasing its chemical potential. It also causes pressure on the vapor phase in equilibrium with it. A convex surface with positive r has a higher vapor pressure than a convex surface with negative r. Additionally, it exhibits a remarkable equilibrium vapor pressure compared to a planar surface with infinite r. One mole of material moving from a flat surface to a spherical surface by a liquid or vapor can be used to determine the value of this increment. The change in chemical potential reflects the work done ($\mu=\mu_0+RT\ln\alpha$, where μ_0 and α represents the standard chemical potential and activity, respectively). While temperature, external pressure, and composition are maintained steady. The potential chemical difference is derived as follows [30], considering a constant activity coefficient:

$$\Delta\mu = RT\ln c - RT\ln c_0 \text{ or } \Delta\mu = RT\ln p - RT\ln p_0 \quad (1.7)$$

Where c implies solubility, p indicates vapor pressure, and c_0 and p_0 represent the equilibrium solubility and vapor pressure through a flat surface, respectively.

A grain boundary movement (illustrated in Figure 1.11) is a short-term diffusion process in which atoms or ions migrate across the boundary and join the orientation of the growing grain. As a result, grain boundary motion is directed in the opposite way of the mean atomic flux.

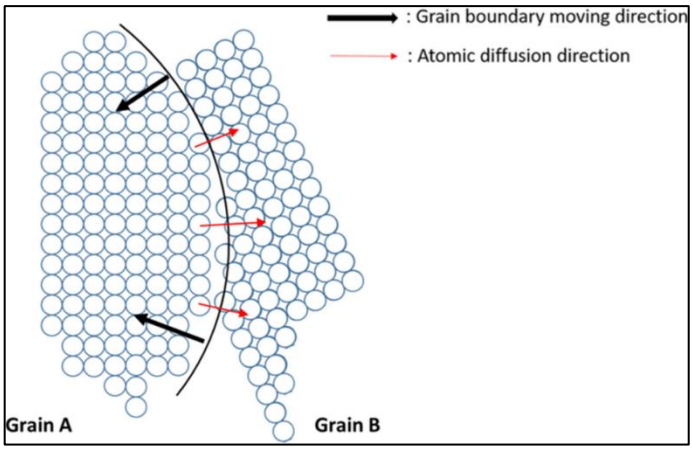

Figure 1. 11. Scheme diagram of grain boundary migration by the atomic transition from grain A to grain B.

The difference in chemical potential, which presents the boundary curvature (pressure differential) between adjacent grains, is the local driving force [38].

$$\Delta P = \gamma_{GB}\left(\frac{1}{r_1}+\frac{1}{r_2}\right) = \frac{\alpha\gamma_{GB}}{G} \tag{1.8}$$

Where ΔP is the difference in pressure between adjacent grains, γ_{GB} is the grain boundary energy, and r_1 and r_2 are the principal radii of curvature perpendicular to each other at the interface between the adjacent grains. α is a geometrical factor that relies on the shape of the boundary, and G represents the grain size.

The grain boundary in a single-phase system will migrate with a velocity V_{GB} under the effect of a curvature-induced driving force, F_{GB}. V_{GB} and F_{GB} are interdependent and can change considerably in the same system according to grain size and curvature differences. Therefore, it is simple to normalize V_{GB} and F_{GB} into a single term known as grain boundary mobility M_{GB} [1].

$$M_{GB} = \frac{V_{GB}}{F_{GB}} \tag{1.9}$$

The difference can be determined in cases where a change in the driving force only results in a velocity difference (M_{GB} remains constant) and when the grain growth process has changed, and a difference in grain boundary mobility is apparent. Moreover, it is essential to examine the grain boundary mobility since a change in M_{GB} can represent a change in the system.

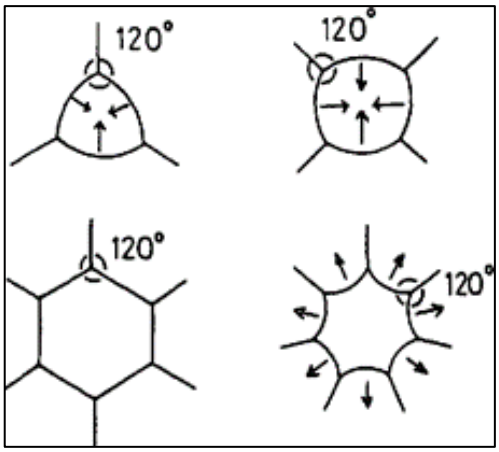

Figure 1. 12. Two-dimensional grain boundary configurations. The arrows represent the directions in which grain boundaries will migrate during grain growth.

Angles of 120° are formed when grain boundaries of equal energy meet at three-grain junctions. Grain boundaries with no curvature only occur for six-sided grains when all boundaries must intersect at an angle of 120°, as shown in Figure 1.12. When viewed from the center of the grain, the boundaries of grains with shorter sides look concave. These grains begin to shrink and eventually disappear as their boundaries get closer to their centers of curvature. Convex boundaries in grains that have more than six sides migrate outward and tend to grow wider. The direction of migration in three dimensions is determined by the net curvature [30].

1.6.2. Effect of Microstructure and Grain Boundary Chemistry on Boundary Mobility

The existence of “second phases” or solutes at the boundary can significantly influence their mobility, and these phases generally move at a rate that is limited. A few possible rate-limiting mechanisms can be discussed to demonstrate the complexity of the problem.

1. Intrinsic grain boundary migration: The intrinsic grain boundary mobility is determined by the rate of movement of atoms or ions across the boundary. An intrinsic drag force F_0 is produced with no other sources of drag, giving F_0 equal to atom diffusion within the potential chemical gradient (m), which exists all over the grain boundary width (δ_{GB}) [1].

$$F_0 = \frac{d\mu}{dx} = \frac{d(\Omega\Delta P)}{dx} = \frac{1}{\delta_{GB}}\frac{\Omega\gamma_{GB}\alpha}{G} \quad (1.10)$$

Where Ω represents the atomic volume.

Burke and Turnbull's model shows that the grain boundary velocity is roughly equivalent to the instantaneous grain growth rate [39]. The intrinsic mobility is derived by integrating this hypothesis with the intrinsic drag force, expressed as a pressure difference, and a potential chemical gradient across the grain boundary. The boundary velocity can also be stated as [40]:

$$V_{GB} = \frac{D_{GB}}{kT}\frac{\Omega}{\delta_{GB}}\frac{\gamma_{GB}\alpha}{G} \quad (1.11)$$

Where D_{GB} is the atomic mobility diffusion coefficient over the grain boundary, k indicates the Boltzmann constant, and T denotes temperature.

2. Extrinsic or solute drag: Impurities or dopants in a polycrystalline material below their solubility limit segregate to the grain boundary via equilibrium (Gibbsian) segregation, which is induced by a decrease in grain boundary energy.

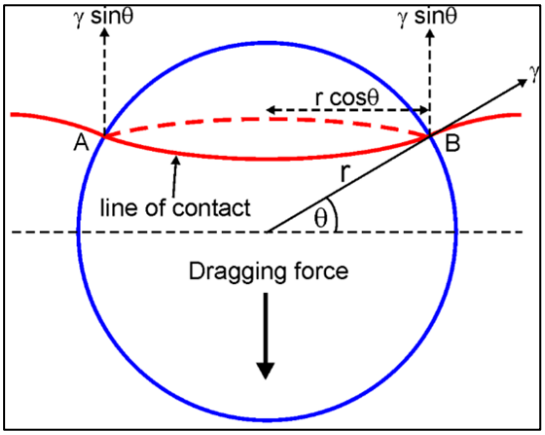

Figure 1. 13. The interaction of a boundary and a particle.

3. Second phases at the grain boundaries: According to the phase diagram, impurities or dopants in a polycrystalline material beyond their solubility limit at equilibrium will precipitate as a second phase. The mobility of larger inclusions is lower compared to smaller inclusions. Additionally, as the volume fraction of a particular inclusion increases, the resistance to boundary mobility increases. Zener is the first effect of a second phase that influences grain boundary velocity [1, 39, 40]. A drag force is generated on the boundary when a particle interacts with the boundary, as shown in Figure 1.13 [40].

The drag force of a single particle is defined as:

$$F_Z = \gamma_{GB} \sin\theta \times 2\pi r \cos\theta = \pi r\, \gamma_{GB} \sin 2\theta \quad (1.12)$$

Furthermore, the highest drag force is obtained when θ=45°:

$$F_Z^{max} = \pi r \gamma_{GB} \quad (1.13)$$

As a result, the grain boundary velocity is lowered as follows:

$$V_{GB} = M_{GB}(F_{GB} - N_Z F_Z) \quad (1.14)$$

Where N_Z refers to the particle or pore density at the grain boundary.

In addition, the following interactions between pores and grain boundaries may occur [41].

A. When the grain boundary has a higher velocity than the pore ($V_{GB}>V_p$), a particle will separate from the grain boundary. This condition is represented in terms of driving force:

$$F_{GB} > N_Z F_Z + \frac{F_Z M_P}{M_{GB}} \quad (1.15)$$

Where M_p denotes spherical pore mobility. Separation is affected by pore density and mobility, which is inversely related to pore radius to the fourth power.

B. When the pore is attached to the grain boundary, they all move at the same velocity ($V_{GB}=V_p$). It can be represented in terms of grain boundary velocity as:

$$V_{GB} = F_{GB} \frac{M_P M_{GB}}{N_Z M_{GB} + M_P} \quad (1.16)$$

Equation (1.16) has two conditions:

i. When $N_Z M_{GB} >> M_p$, in which the grain boundary migration is limited by pore mobility, also known as pore control (Figure 1.14(a))

ii. When $N_Z M_{GB} << M_p$ in which the pore has no effect on the migration rate of the grain boundary, also known as boundary control (Figure 1.14(b)).

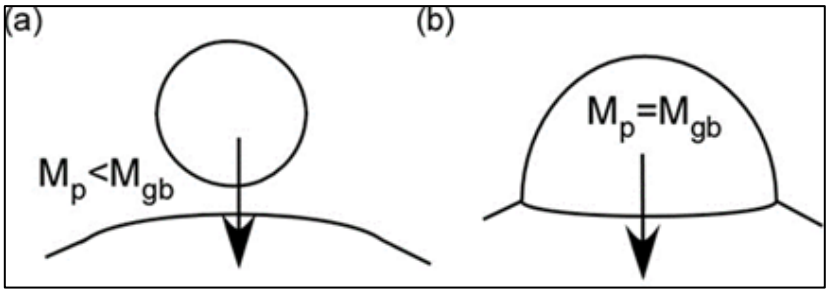

Figure 1. 14. Schematic drawings of possible interactions between a second phase particle (or pore) and a grain boundary. (a) When the grain boundary migration rate surpasses the particle mobility ($M_{GB}>M_p$), the particle is separated from the moving grain border. The particle is finally obliterated by the growing grain. (b) When $M_{GB}=M_p$, the particle mobility limits grain boundary motion.

1.6.3. Impurity Segregation at Grain Boundary

Impurities can be found in various configurations in a material, as shown in Figure 1.14. They can exist as a solute in the bulk or an adsorbate at the grain boundaries. They can precipitate as second-phase particles at multigrain junctions after they achieve their solubility limit. They can also be detected in amorphous triple point pockets and grain boundary films (amorphous or crystalline).

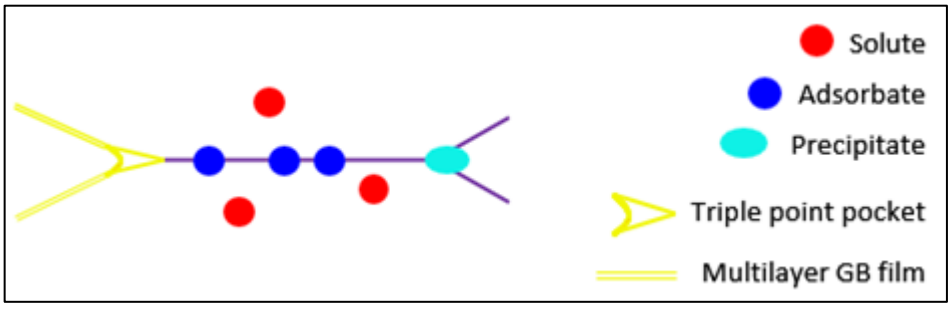

Figure 1. 15. Impurity distribution.

Impurities appear as a solute in bulk and segregate at grain boundaries at any concentration. When the concentration of solute in bulk is less than the bulk solubility limit ($X_t<X_t^*$), the ratio of grain boundary concentration (C_{GB}) to bulk concentration (C_{bulk}) is determined by the free energy change due to segregation ΔG_{seg} and is calculated by:

$$C_{GB}/C_{bulk} = K = exp\frac{\Delta G_{seg}}{kT} \quad (1.17)$$

In comparison to the bulk, grain boundaries are regions of disorder that may easily contain ions with varied sizes. As a result, if ΔG_{seg} is high, the grain boundary chemistry may differ significantly from the bulk, emphasizing the influence of impurities [40]. Thus, both small and large ions will segregate to the grain boundary.

The simplified Langmuir-McLean relationship can be used to predict impurity segregation at grain boundaries. Gülgün et al. [42] also used this model to calculate the grain boundary coverage of yttrium in α-alumina for low yttrium concentrations. It was observed that impurity surface coverage (Γ) varies with impurity level and grain size. When the yttrium level approaches 100 ppm, the yttrium concentration reaches the bulk solubility limit ($X_L=X_L^*$) at grain sizes of 5-7 m and precipitates as yttrium alumina garnet (YAG). Γ_c is the critical surface coverage, indicating the segregation level in equilibrium with the second-phase precipitates. If there is an efficient nucleation barrier to second-phase precipitation, the transient (non-equilibrium) surface coverage could exceed this critical value of Γ_c.

ImageJ processing program was applied for this thesis to evaluate the morphology of particles, measure the particle size, and calculate calcium distribution at grain boundaries. The detailed calculations and discussions were given in section 3.2.5.1.

As previously stated, grain boundary segregation significantly depends on the grain size. Figure 1.16. which retrieved from M. Ruehle's research illustrated that when the grain size doubled, the concentration of the segregant at the grain boundaries increased twice the initial amount. The number of impurity atoms in this figure is the same for both drawings and the grain size of the second drawing is precise twice the first one.

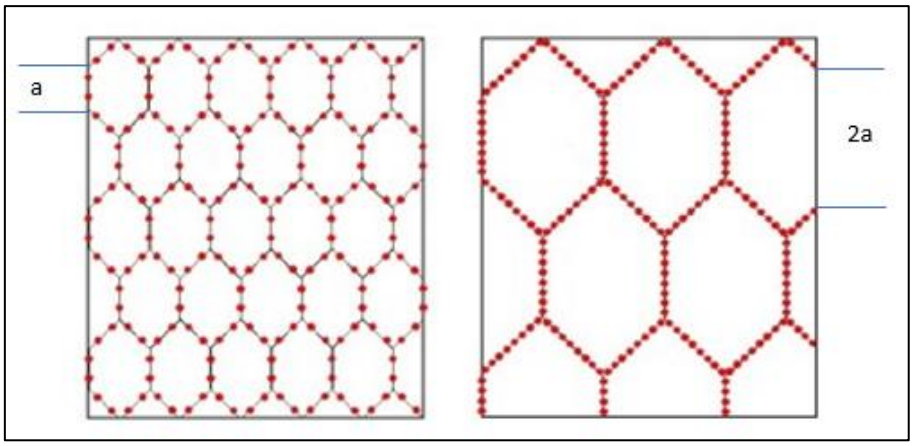

Figure 1. 16. Segregation at grain boundaries for different grain boundary densities {Manfred Ruehle}.

1.6.4. Abnormal Grain Growth

Abnormal grain growth (AGG), also known as excessive grain growth, occurs when a few grains grow to a large size, usually much more extensive than regular grains. Abnormal grains grow at the expense of regular grains, resulting in greater grain boundary mobility. As displayed in Figure 1.17 when a large grain grows, it will be surrounded by a significant number of neighbors (over six) [32].

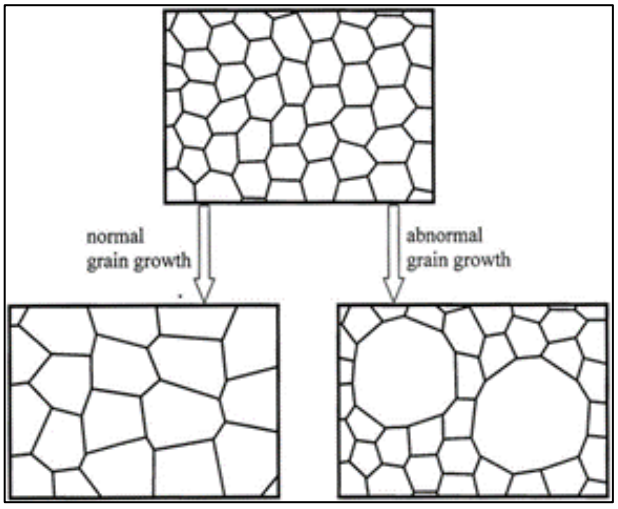

Figure 1. 17. Illustration of polycrystalline material, where a grain with more than six neighbors will grow during a grain with less than six neighbors will shrinkage.

Second phases and impurities are commonly thought to restrict normal grain growth, resulting in only grains with grain boundaries with a curvature more remarkable than the average curvature successfully migrating. Therefore, those specific grains will grow as the matrix remains regular in size.

I. J. Bae and Baik [43] have measured final densities and grain sizes after sintering ultrapure alumina. They showed that when small amounts of glass-forming impurities are introduced, some portion beyond their solubility limit will accumulate at grain boundaries at the final stage of densification and form thin intergranular glass films (IGFs). They observed that these impurities induce the sudden appearance of abnormal grains by raising the mobility of grain boundaries. Small amounts of SiO_2 in ultrapure alumina (>99.999%) were used to test the hypothesis experimentally. The concentration of SiO_2 was inversely related to average grain sizes in the appearance of abnormal grain growth. Therefore, the critical concentration of SiO_2 is defined at the onset of abnormal grain growth.

1.6.5. Measuring The Grain Boundary Mobility

Measuring grain boundary mobility is a complicated process. Nonetheless, many researchers have described the grain boundary mobility in undoped samples. Measuring the average grain size after an annealing treatment (grain growth) is one of the most common methods for evaluating grain boundary mobility.

$$V_{GB} = \frac{d\bar{G}}{dt} = \frac{2M_{GB}\gamma_{GB}}{\bar{G}} \tag{1.18}$$

The grain growth law can be obtained by integrating equation (1.18):

$$\bar{G}_t^2 - \bar{G}_0^2 = 4M_{GB}\gamma_{GB}t = kt \tag{1.19}$$

Where the adequate mobility is $M_{GB}.\gamma_{GB}=k_1/t$, $\overline{G_t}^2$ is the average squared grain size at time t, $\overline{G_0}^2$is the average squared grain size at t=0, and k refers the rate constant. The major drawback of this fast method is that we can only evaluate the mean adequate mobility without specifying the mobility of a specific plane.

A diffusion bonding technique is performed to measure the mobility of a specific plane. In this experiment, a specific grain with a particular surface orientation is diffusion

bonded to a polycrystalline sample. The growth of the single grain is studied as a function of time. The equations are like those used to describe the growth of polycrystalline samples.

$$\overline{\Delta l}^2(t) = kt \tag{1.20}$$

Where $\overline{\Delta l}^2$ is the average squared motion of the grain at time t.

1.7. Grain Boundary Mobility in Al_2O_3

Abnormal grain growth in alumina is not fundamental but is influenced by impurities added into the ceramic during powder synthesis, processing, or sintering. It controls numerous interfacial properties, including sintering, densification, creep, and intergranular fracture. Several theories have been suggested to explain abnormal grain growth in alumina. For example, a wide initial particle size distribution, grain boundary separation from pinning particles, pore-boundary separation, inhomogeneous packing, and densification, nonuniform grain boundary mobilities, the existence of certain fluxing impurities such as Na and K in alumina, irregular distribution of impurities such as Ca and Si, or formation of liquid phase during sintering have all been considered earlier. The presence of impurities, particularly CaO and SiO_2, is critical for initiating abnormal grain growth in the final sintering stage. Such impurities are thought to generate glassy films in grain boundaries. To obtain high density in alumina by sintering, it is critical to prevent abnormal grain growth in the last stage of densification. In Coble's experiments in the early 1960s [44], adding a small amount of MgO was an essential step in controlling abnormal grain growth and generating completely dense, translucent alumina.

1.7.1. MgO Doped Al_2O_3

The addition of MgO to alumina influences the microstructural evolution considerably. It prevents abnormal grain growth and decreases the mean grain boundary mobility. Compared to undoped alumina, grain sizes in sintered material are small [9, 10, 45].

In a study by Bennison and Harmer [10], the kinetics of grain growth in fully dense Al_2O_3 with and without MgO solute additions were measured. The MgO was found to retard boundary migration and develop more uniform microstructures. The growth-rate constants for pure and MgO-doped Al_2O_3 were determined to be 1.74×10-19 m3/s and 3.9×10-20 m^3/s, respectively. Therefore, when present in solid solution, MgO decreases the overall boundary migration rate in fully dense Al_2O_3, and comparison at equivalent grain sizes indicates that the growth rate for undoped Al_2O_3 is five times that for MgO-doped samples.

The composition and concentration of background impurities and particles in the alumina matrix have influenced how Al_2O_3 responds to MgO doping. When common impurities like CaO and SiO_2 are introduced, Handwerker et al. [7] found that MgO prevents second-phase creation and decreases impurity concentration at the grain boundary. The relation between MgO doping and Si segregation to grain boundaries shows that a precise cation ratio is required to achieve a dense microstructure. Moreover, these observations indicate that a co-doping effect is involved and that MgO lowers the solubility limit of impurities.

It has been found that MgO significantly impacts the location of Ni nanoparticles in alumina in nanocomposites. Gluzer et al. [46] showed that particle occlusion increased with sintering time and temperature. It was related to detected Mg segregation at the Ni–alumina interfaces, resulting in partial Mg depletion at the alumina grain boundaries and increased mobility.

Gavrilov et al. [47] investigated the distributions of SiO_2 and MgO in sintered alumina using scanning secondary ion mass spectrometry (SIMS). They showed that when doped with each additive individually, evidence is seen for strong silicon segregation to grain boundaries in SiO_2-doped alumina and strong magnesium segregation to grain boundaries in MgO-doped alumina. However, when codoped with both SiO_2 and MgO, the segregation of both ions to grain boundaries is decreased by five or more over single doping. The additives in the grains grow correspondingly, and both dopants become more evenly distributed across the bulk. It is concluded that co-doping with these additives increases the solid bulk solubility and decreases the interfacial segregation over single doping. According to their results, the beneficial effect of MgO additions in controlling microstructure development in alumina and improving corrosion resistance is based on the ability of MgO to redistribute silicon ions from grain boundaries into the bulk.

1.7.2. CaO Doped Al_2O_3

The surface enrichment of Ca on different crystallographic planes of CaO-doped sapphire as a function of annealing temperature was measured by Baik et al. [48] using Auger electron spectroscopy. In the temperature range between 800° and 1500°C, no Ca segregation was detected to the [0001] basal plane. However, at temperatures over 1300°C, the surface phase transition was observed without evidence of impurity. While there was a significant enrichment of Ca on the [10$\bar{1}$0] plane between 1300°-1500°C and a slight but noticeable amount of Ca was detected even below 1300°C. On this prism plane, Ca segregation was revealed to be homogeneous and restricted to the surface monolayer, and it appeared simultaneously with a 2D phase transition. Such anisotropy in Ca segregation was thought to cause the formation of nonuniform microstructures observed in sintered alumina, which typically contains a small amount of Ca as an impurity.

Mukhopadhyay and Baik [49] conducted similar studies on the segregation of magnesium and calcium to the [10$\bar{1}$0] prismatic plane of magnesium-doped sapphire. It was revealed that segregation behavior was greatly influenced by the annealing atmosphere. Mg segregation to the free surface was only identified in air annealing, whereas no Mg segregation was observed in vacuum annealing. Nevertheless, significant Ca segregation was observed in the absence of Mg on the surface, which explained the extensive vaporization of MgO at low oxygen pressures. The absence of Ca segregation upon annealing in the air was related to the surface efficiency of Mg in repelling Ca. It was estimated that Ca is the more effective segregant depending on the surface-to-bulk ratios of Ca and Mg concentrations and the more considerable mismatch between Ca^{+2} and Al^{+3} than Mg^{+2} and Al^{+3}. The scientists suggested that because the mobility of the Mg^{+2} containing defect was significantly larger than that for the corresponding Ca^{+2} defect, the Mg could establish its surface concentration much faster.

Kaplan et al. [50] discovered Ca segregation to alumina basal surfaces in melt-infiltrated polycrystalline alumina-aluminum composites, which contradicted the findings of the previous investigations. High-resolution transmission electron microscopy (HRTEM), in

combination with analytical electron microscopy (AEM), revealed the presence of Ca at the embedded basal surfaces of α-Al_2O_3. More than seven different basal α- Al_2O_3/Al interfaces were measured in the study, and Ca excess was found to be Γ_{Ca}=2.5±0.5Ca atoms/nm^2 at the same interfaces. It was detected at the surface and distributed throughout four cation layers, resulting in a surface phase with the nominal composition of $CaO.6Al_2O_3$. Ca also is segregated to basal twin boundaries, albeit with a smaller total excess than at free basal surfaces. They also demonstrated that alumina grains with Ca segregation have an elongated morphology.

Cook et al. [51] used Auger electron spectroscopy and scanning electron microscopy to investigate the segregation behavior of Ca at grain boundaries in a series of CaO-doped polycrystalline alumina. As fractured and sputtered surface spectra and the proportion of transgranular failure exposed to the probe beam were examined to determine the grain boundary concentrations from spectroscopy on the fracture surfaces. Polycrystalline alumina spectra were identified by the presence of a Ca_{LMM} signal and a reduced low-energy Al_{LMM} signal compared to single-crystal sapphire spectra. The Ca_{LMM} signal disappeared and the Al_{LMM} signal restored to that observed in sapphire after sputtering the polycrystalline surface. This result illustrates that Ca atoms were segregating substitutionally to Al_2O_3 grain boundaries. It was also reported that the segregation of Ca to the grain boundaries formed by the fracture process was quickly saturated. According to the findings, when grain boundary Ca segregation increased, the fraction of transgranular failure increased significantly, with adverse effects on fracture properties such as toughness. Before a specific conclusion can be obtained, the dependence of the fracture behavior of the material on grain size must be considered. Transgranular failure could be explained by abnormal grain growth caused by adding Ca to alumina.

Grain boundary mobility in CaO-doped alumina samples is attractive since the appearance of elongated abnormal grains is related to the presence of CaO in alumina. Bae and Baik [8] and Jung and Baik [43] investigated the effect of CaO on abnormal grains as a function of CaO concentration, sintering temperature, and time. They discovered that a significant Ca concentration caused abnormal grain growth and associated it with developing IGFs with a minimum thickness of 0.35nm and a nominal composition like calcium hexaaluminate ($CaO.Al_2O_3$).

Dillon et al. [52, 53] investigated the kinetics of grain growth in alumina doped with CaO or SiO_2 over a wide range of sintering temperatures. This experiment was carried out to clarify the conflicting results of previous studies on AGG in doped alumina. Some investigations indicated the presence of intergranular films related to AGG. In contrast, others stated that AGG is caused by grain boundary faceting or the lack of it, and others connected excessive growth to grain morphology [54, 55]. Because of the complexity of internal interfaces, it has been a struggle to connect alumina grain growth behavior (particularly the onset of AGG) to internal interface structure, chemistry, and the corresponding atomic transport rate. In terms of the new idea of interface complexions, Dillon and Harmer [52] investigate the normal and abnormal grain growth in calcium-doped alumina, a material known for its complex AGG behavior. In the temperature range of 1325°–1870°C, calcium-doped alumina revealed four different grain-boundary complexions and abnormal grain growth due to the addition of CaO to alumina, as shown in Figure 1.18.

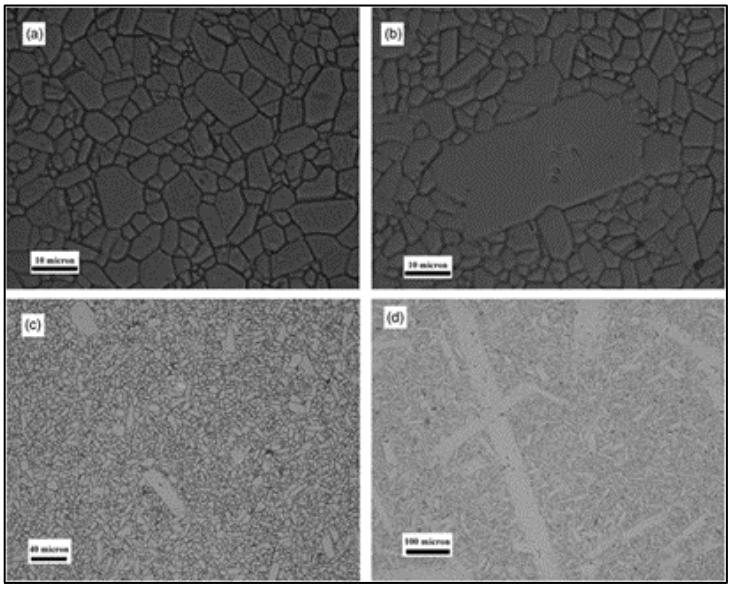

Figure 1. 18. Normal grain microstructure in calcium-doped alumina sintered at (a) 1400°C for 1230 min and (b) an abnormal grain from the same sample. Microstructure of samples sintered at (c) 1475°C and (d) 1675°C.

At the same temperature, all four complexions may occur. Each complexion has distinct grain-boundary mobility, as shown in Figure 1.19. It is related to the amount of CaO excess at the grain boundary, affecting the chemistry and structure of the grain boundary. All of which increase grain growth kinetics as compared to undoped alumina.

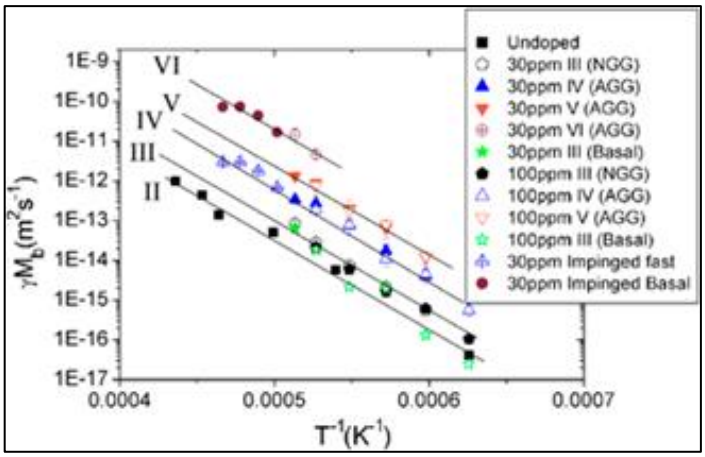

Figure 1. 19. Grain-boundary mobilities for various normal, impinged, and unimpeded abnormal grains in calcium-doped alumina.

They were successful in associating distinct grain boundary motilities with six different complexions. They studied the apparent thickness of the complexions using high-resolution transmission electron microscopy (HRTEM) or high-angle annular dark field (HAADF) scanning TEM (STEM), as illustrated in Figure 1.20.

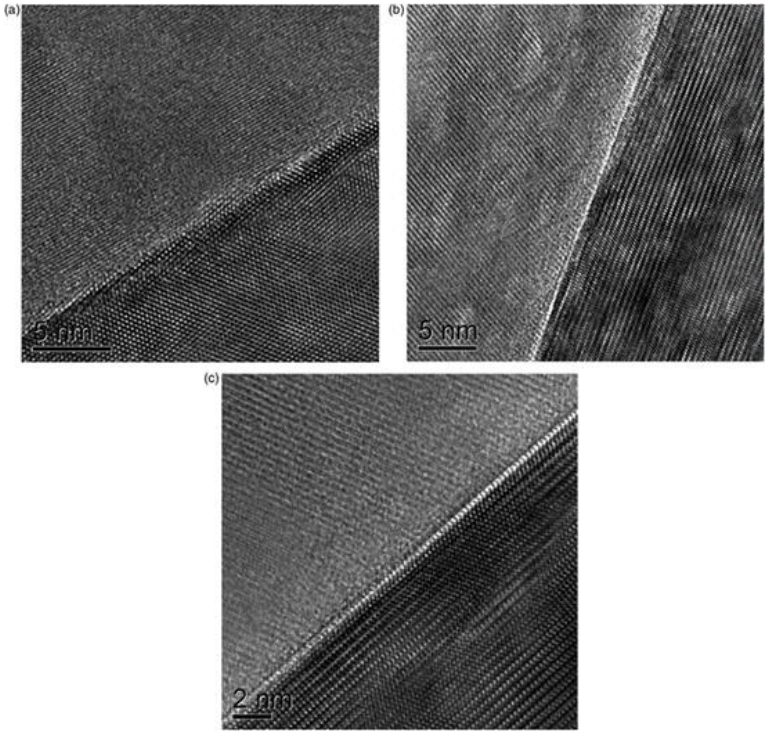

Figure 1. 20. Transmission electron micrographs of the grain boundaries of (a) normal grain, (b) the basal plane of a normal grain, and (c) the basal plane of an abnormal grain.

It should be noted that Dillon and Harmer did not correlate the mobility with the actual grain boundary chemistry but rather the apparent width of the grain boundaries.

Akiva et al. [56] investigated the mobility of CaO or MgO-doped alumina samples with dopant levels evaluated in the final material. They discovered that, below the solubility limit, MgO and CaO behaved as expected. They lowered and enhanced grain boundary mobility, respectively. The influence of CaO was because of the adsorption and not the formation of a liquid phase. Furthermore, excess measurements between the basal plane of sapphire and polycrystalline CaO-doped alumina revealed the presence of CaO at the interface, which confirms the presence of Gibbsian segregation.

Avishai et al. [57] also investigated the presence of complexions and their effect on the evolving microstructure of alumina-based nanocomposites. The occlusion of metal particles was observed in Ni-reinforced alumina nanocomposites doped with CaO or SiO_2. However, undoped samples did not contain an occluded particle microstructure. The presence of an IGF in the doped samples was confirmed and associated with increased grain boundary mobility. However, it should be emphasized that the doping levels in this work were over the reported solubility limits for both CaO and SiO_2, resulting in the development of anorthite glass at the triple junctions, which undoubtedly influenced the mobility of the triple junctions [58].

Park and Yoon [54] demonstrated the effect of adding CaO and SiO_2 to their samples. They doped their samples with 50 ppm CaO and sintered them at various times and temperatures. They discovered large, elongated grains with faceted grain boundaries with no frozen liquid at the triple point junctions and grain boundaries, as shown in Figure 1.21.

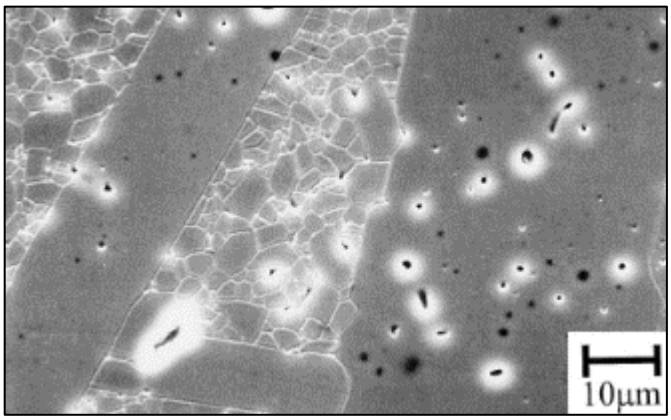

Figure 1. 21. Microstructure of alumina doped with 100 ppm of SiO_2 and 50 ppm of CaO indicating abnormal elongated grain.

The results indicated normal growth for undoped alumina. In contrast, adding CaO and SiO_2 with increasing time and temperature resulted in abnormal grain growth, where the abnormal grains were elongated in directions that were probably parallel to the basal [0001] planes. They found a correlation between the occurrence of AGG in alumina and the formation of faceted and straight-grain boundaries. It was claimed that these grain boundaries contain single-ordered structures with low boundary energy and that their growth by lateral step movement can induce AGG. The addition of MgO leads to grain boundary roughening and, therefore, normal grain growth.

Altay and Gülgün [59] investigated different calcium doping concentrations affecting the polycrystalline alumina microstructure. They associated grain growth with a hypothetical Ca concentration at grain boundaries, assuming no Ca in solution in the grains rather than measuring the concentration in the alumina grains. They discovered a critical grain boundary concentration, Γ_{Ca}=3Ca atoms/nm^2. They indicated that calcium impurities caused elongated (slab like) grain morphology when excess at this critical concentration level at the grain boundaries (as shown in Figure 1.22).

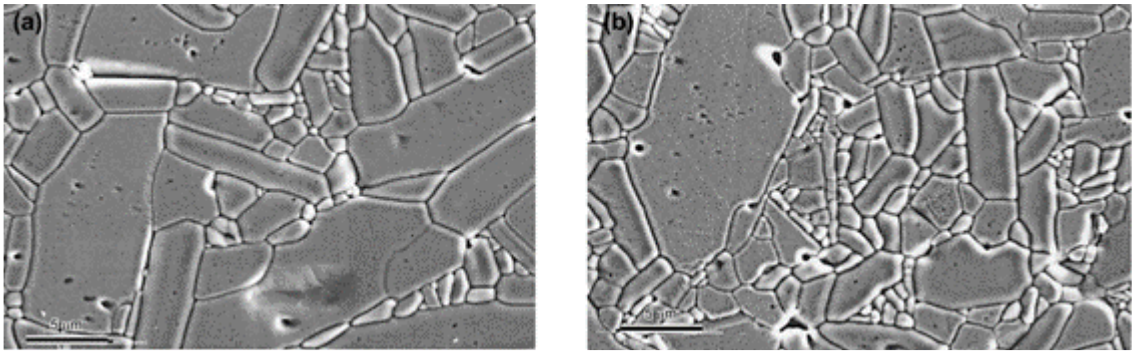

Figure 1. 22. SEM micrograph of (a) 344-ppm-Ca-doped α-Al_2O_3 sintered at 1500°C for 12 h showing abnormally grown grains. (b) 650-ppm-Ca-doped α-Al_2O_3 sintered at 1500°C for 12 h with abnormally grown, elongated grains.

1.8. Phase Equilibria in CaO-Al_2O_3 System

Phase diagrams illustrate which equilibrium phases are present in a material system at different temperatures, compositions, and pressures when the system is allowed to reach equilibrium [29].

Phase diagrams, in principle, provide the following information:

i. The phases present at equilibrium
ii. The phase composition at any time during heating or cooling
iii. The amount of each phase present
iv. The range of solid solubility of one element or compound in another.

Calcium aluminates are produced by heating calcium oxide and aluminum oxide at elevated temperatures. The measured phase equilibrium diagram of the CaO-Al_2O_3 system is illustrated in Figure 1.23. There are five stable compounds in the calcium aluminates phase diagram as shown in Figure: (1) tricalcium aluminate/$3CaO.Al_2O_3$ (C_3A), (2) dodecacalcium hepta-aluminate/$12CaO.7Al_2O_3$ ($C_{12}A_7$), (3) monocalcium aluminate/$CaO.Al_2O_3$ (CA), (4) monocalcium dialuminate/$CaO.2Al_2O_3$ (CA_2), and (5) monocalcium hexa-aluminate/$CaO.6Al_2O_3$ (CA_6) [60]. The lowest melting temperature of these is for the $C_{12}A_7$ phase (1722°C), and the highest is for the CA_6 phase (2156°C) [61].

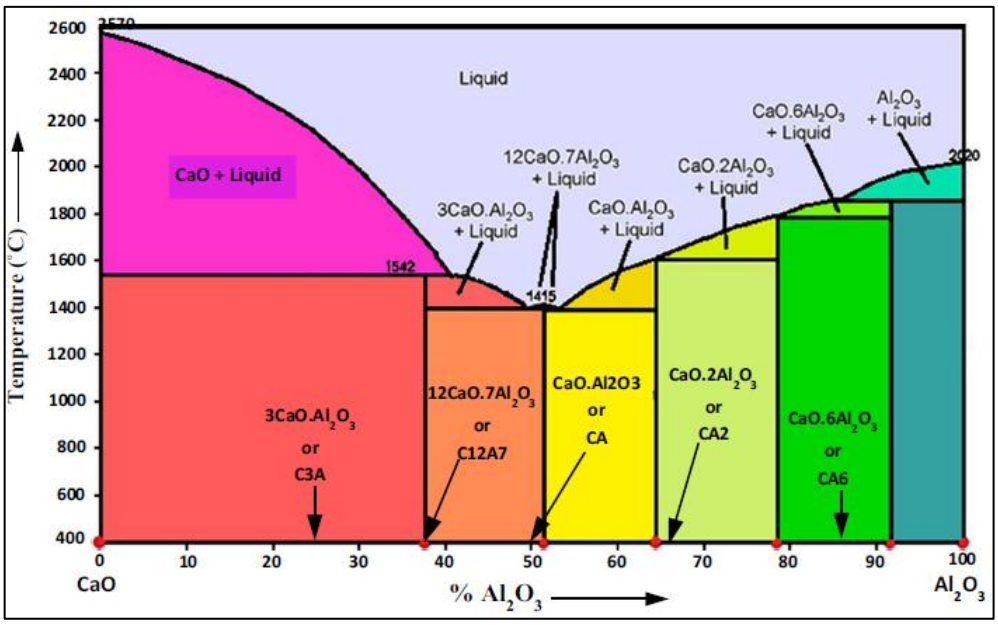

Figure 1. 23. Obtained diagram of the CaO-Al_2O_3 system.

Akiva et al. [62] measured the solubility limit of Ca in 99.99% pure α-Al_2O_3 (alumina) using a wavelength dispersive spectrometer (WDS) mounted on a scanning electron microscope. Al_2O_3 samples were equilibrated at a concentration that ensured Al_2O_3 grains were saturated with Ca and were quenched in water from 1600°C. The solubility limit of

Ca was determined from samples saturated with Ca, which was found to be 51 ± 1 ppm. In this work, the presence of Ca above the solubility limit is correlated with elongated alumina grains and a grain boundary enrichment of ~ 6Ca atoms/nm^2. Analytical TEM was conducted on quenched samples to confirm Ca enrichment (as the samples contained Ca above the solubility limit) at the grain boundaries as shown in Figure 1.24.

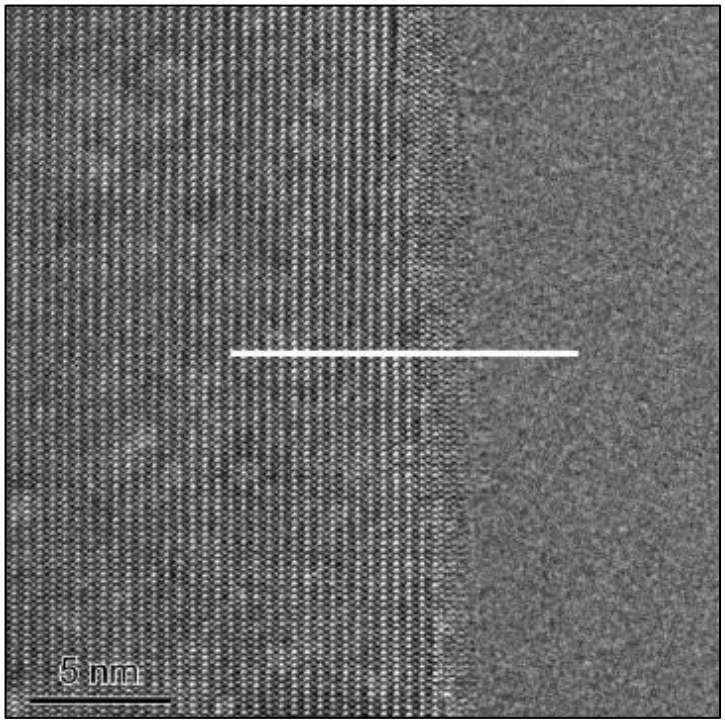

Figure 1. 24. HRTEM micrograph of an alumina grain boundary, after orienting the grain on the left into the [$2\bar{1}\bar{1}2$] zone axis with the boundary plane parallel to the incident electron beam.

2. RESEARCH GOALS

The primary purpose of this research is to investigate the morphological properties of polycrystalline alumina doped with Ca. Calcium is one of the most prevalent impurities identified in commercial Al_2O_3 that is believed to affect the properties of alumina. Studies have investigated the influence of impurities on grain boundary mobility in alumina and believe that a new grain boundary structure is happening in different temperature ranges. The effects of different time and temperatures on the formation of calcium phases in polycrystalline α-alumina will be examined in this study. The diffusion process between the phases to generate a new phase is also described.

3. EXPERIMENTAL METHODS

The experimental methods mentioned below were applied in this study to understand the influence of impurities on the evolving microstructure of a ceramic material, specifically Ca-alumina nanocomposites. The formation process of calcium phases was also studied in this thesis. The processing techniques for alumina, characterization methods and methodology, will be discussed in this section.

3.1. Materials

Polycrystalline alumina samples were prepared using high purity (99.99%) AA-03 α-Al_2O_3 (Sumitomo Chemical Company, Ltd., Osaka, Japan), to which different amounts of ACS grade Ca $(NO_3)_2.4H_2O$ (MERCK) was added. To disperse and dope the powders homogeneously, ACS grade ethanol absolute (JT Baker) was used as the mixing media. Initial chemical compositions of the chemicals used are given in Tables 3.1-3.3 as reported by the manufacturers.

Table 3. 1. High purity alumina "AA-03" (Al_2O_3) analytical data Sumitomo Chemical Company, Ltd.

Crystal Structure	α
Purity (Al_2O_3)	max. 99.99%
Mean Particle Size (MT3300)	0.40μm
Loose Bulk Density	0.5 g/cm^3
Tapped Bulk Density	0.9 g/cm^3
B.E.T Specific Surface Area	5.6 m^2/g

Impurity Analysis	
Si	4 ppm
Fe	2 ppm
Na	3 ppm
Mg	1 ppm
Cu	1 ppm

Table 3. 2. Calcium nitrate tetrahydrate $Ca(NO_3)_2.4H_2O$ analytical data MERCK, GR for analysis, ACS

Assay (complexometric)	99.0-102.0%
Insoluble matter and precipitate by Ammonium Hydroxide	max. 0.005%
pH-value (5%; water; 25°C)	5.0-7.0
Chloride (Cl)	max. 0.005%
Nitrite (NO_2)	max. 0.001%
Sulphate (SO_4)	max. 0.002%
Heavy Metals (as Pb)	max. 0.0005%
Barium (Ba)	max. 0.005%
Copper (Cu)	max. 0.0002%
Iron (Fe)	max. 0.0005%
Potassium (K)	max. 0.005%
Magnesium (Mg)	max. 0.01%
Sodium (Na)	max. 0.01%
Strontium (Sr)	max. 0.01%
Corresponds to ACS	

Table 3. 3. Ethanol analytical data J.T. BAKER, Baker analyzed, ACS

Assay	min. 99.9%
Acetone, isopropylalcohol	passes tests
Color (APHA)	max. 10
Methanol (CH_3OH)	max. 0.1%
Residue after Evaporation	max. 0.001%
Solubility in Water	passes tests
Substances Darkened by H_2SO_4	passes tests
Substances Reducing $KMnO_4$	passes tests
Titrable Acid (meq/g)	max. 0.0005
Titrable Base (meq/g)	max. 0.0002
Water (H_2O)	max. 0.2%
Trace Impurities (in ppm)	
Aluminium (Al)	max. 0.5
Boron (B)	max. 0.02
Barium (Ba)	max. 0.1
Calcium (Ca)	max. 0.5
Cadmium (Cd)	max. 0.05

Cobalt (Co)	max. 0.02
Chromium (Cr)	max. 0.02
Copper (Cu)	max. 0.2
Iron (Fe)	max. 0.1
Magnesium (Mg)	max. 0.1
Manganese (Mn)	max. 0.02
Nickel (Ni)	max. 0.02
Lead (Pb)	max. 0.1
Tin (Sn)	max. 0.1
Zinc (Zn)	max. 0.1
Corresponds to ACS	

Pure alumina milling balls (99.7%, Friatec, Germany) and agate mortar and pestle were used for milling and grinding the powders. The powder mixture was used to form green bodies by dry pressing, followed by cold isostatic pressing (CIP). The green compacts were sintered inside high-purity alumina crucibles (Halden-Wanger, Germany). Once sintered, this resulted in the presence of calcium aluminate phases and alumina grains. The equilibrated two-phase sample means that the alumina grains are saturated with Ca. Each sample was cut, and the inner sections were mechanically polished using a diamond suspension on polishing cloths.

3.2. Sample processing

3.2.1. Green Bodies Preparation

Polycrystalline alumina samples were prepared using the same alumina powder mentioned above, to which water and calcium nitrate ($Ca(NO_3)_2.4H_2O$) were added. The amount of calcium nitrate added was varied to reach expected concentrations of 50, 100, 200, 500, 1000, 5000, and 10000 ppm of calcium in the alumina. All calculations were based on the calcium/alumina ratio in weight ppm as shown:

MW $_{Ca\ (NO3)2.4H2O}$ =236.15 gr/mol

MW $_{CaO}$=56.07 gr/mol

MW $_{Al2O3}$=101.96 gr/mol

236.15 gr of calcium nitrate gives 56.07 gr of calcium oxide. So, for 1 gr of oxide, 4.21 gr of nitrate is needed (% mol of CaO/Al_2O_3).

1 kg of Al_2O_3 is 9.80 moles of Al_2O_3. For 1000 mol ppm of CaO, 0.0098 moles of CaO are needed, that is 0.0098×56.17=0.55 gr of CaO, and it is equal to 2.20× (236.15/56.07) =2.32 gr of nitrate at ppm (Ca/Al). On the other hand, 1 kg of Al_2O_3 is 9.80 mol×2 atoms/mol=19.60 mol Al and 0.019 atom mole of Ca is required. Out of 236.15 gr of nitrate comes 1 mole atom of Ca. Thus 0.019 mole atom Ca comes from 236.15×0.019=4.63 gr of calcium nitrate.

1 kg Al_2O_3	4.63 gr Ca $(NO_3)_2.4H_2O$
20 gr Al_2O_3	χ gr Ca $(NO_3)_2.4H_2O$

χ=0.092 gr Ca $(NO_3)_2.4H_2O$

The amount of $Ca(NO_3)_2.4H_2O$ needed for each level of Al_2O_3 is illustrated in Table 3.4.

Table 3. 4. Calcium doping levels in weight ppm.

10000ppm	0.92 gr Ca $(NO_3)_2.4H_2O$
5000ppm	0.46 gr Ca $(NO_3)_2.4H_2O$
1000ppm	0.092 gr Ca $(NO_3)_2.4H_2O$
500ppm	0.046 gr Ca $(NO_3)_2.4H_2O$
200ppm	0.0184 gr Ca $(NO_3)_2.4H_2O$
100ppm	9.2×10^{-3} gr Ca $(NO_3)_2.4H_2O$
50ppm	4.6×10^{-3} gr Ca $(NO_3)_2.4H_2O$

For each calcium doping level, 20 grams of Al_2O_3 powder and a calculated amount of Ca $(NO_3)_2.4H_2O$ were weighed with a high precision balance (+0.0001gr) and put in a pre-cleaned 1-l HDPE bottle. Deflocculation of the alumina suspensions was conducted by adding a small amount (5000ppm) of analytically pure citric acid to reach very fine particles. It is seen that citric acid causes the destabilization of solutions and significantly enhances aggregation. Distilled water was poured into the bottle until half of it was filled. After putting approximately half a kilogram of alumina balls into the bottles, the lids were closed and sealed with teflon and parafilm. Mixing was performed for 6 hours using a ball-milling system without milling balls to reduce contamination. et, and then smashed using a mortar and a pestle. 7 pellets weighing around 1 gram were pressed from various calcium doping levels.

Green bodies were prepared using a uniaxial press at 25 MPa for 1 minute (Sabanci University, Istanbul, Turkey). The green compacts were discs 10 mm in diameter. During the uniaxial pressing of powders, the hardened steel die was lubricated with pure liquid paraffin (Atabay Kimya, Istanbul, Turkey) to avoid sticking powders to die surfaces.

Cold isostatic pressing of the samples was performed at the Faculty of Engineering and Natural Science, Sabanci University, Istanbul. Samples were put inside the fingers of

powder-free latex gloves and then inserted in the high-pressure resistant qualetex balloon (Aldrich). The pressure balloons were evacuated with a vacuum pump before pressing. Samples were finally isostatically pressed at 200 MPa for 2 minutes.

3.2.2. Sintering

The samples were sintered in a tube furnace at the different temperatures of 1300°C, 1400°C, and 1550°C (heating rate 10°C/min) for 10 h. Additionally, the samples were sintered at 1300°C for different durations of 1hr 2h, and 4h. The samples were layered with the same alumina powder used to form the green bodies to prevent contamination from the furnace during the sintering. After sintering, samples were furnace-cooled at 10°C/min.

3.2.3. Density Measurement

The densities of the samples were measured for all sintering times and temperatures using Archimedes' method and distilled water following ASTM standard c 20-92. Appendix A contains the details of the density measurement.

3.2.4. Microstructural Analysis

3.2.4.1. Grain Size Measurement

The number of grains (or grain boundaries) that intersected a given length of randomly oriented straight line was used to calculate grain size. The grain boundary area per unit volume S_V (total grain boundary area) can be calculated using the mean number of intercepts of random test lines with grain boundaries per unit length of test line N_L.

$$S_V = 2N_L \tag{3. 1}$$

By implying constant spherical grains and considering that each grain boundary is shared by two adjacent grains, it is possible to determine the mean grain diameter D from S_V [63].

$$2S_V = \frac{4\pi(D/2)^2}{4\pi/3(D/2)^3} \quad (3.\ 2)$$

Or

$$D = \frac{3}{S_V} = 3/2N_L \quad (3.\ 3)$$

This method is known as the mean linear intercept method for measuring particle size. The length of the line divided by the typical number of grains intersected yields the mean linear intercept length, or $\bar{L}$. Thus,

$$\bar{L} = 1/N_L \quad (3.\ 4)$$

$$Grain\ Size\ (G) = D = 1.5\bar{L} = 3/S_V \quad (3.\ 5)$$

This methodology is used for all grain size measurements in this dissertation.

3.3. Sample Characterization

Various characterization methods were used in this research to obtain structural and chemical information from the material at the micro and nano levels. The following are the methods used:

The crystal structure and phases of the powders and sintered material were identified using X-Ray Diffraction (XRD).

Scanning Electron Microscopy (SEM) was applied to evaluate the microstructure and grain sizes of powders.

Energy Dispersive Spectroscopy (EDS) was used to perform X-ray spectral measurements to get the elemental information.

Back Scattered Electron imaging (BSE) was used to discover probable second phase precipitates.

Transmission Electron Microscopy (TEM) was used to get detailed information from the materials at nanometer resolution. Crystal structure, grain boundaries, and chemical composition were all examined.

Precision Ion Polishing System (PIPS) was used to prepare an ultra-thin sample for further TEM analysis.

3.3.1. X-Ray Dffraction (XRD)

X-ray diffraction (XRD) is a widely used method for collecting qualitative and quantitative information about atomic scale structure from crystalline and non-crystalline (amorphous) materials. X-ray Powder diffraction is used to identify crystalline phases and refine crystal structures. XRD can also analyze crystallite size, lattice strain, chemical composition, and crystal orientation.

When an X-ray beam interacts with repeating planes of atoms in a crystal lattice, (1) part of the beam is transmitted, (2) part is absorbed by the sample, (3) part is refracted and scattered, and (4) a part is diffracted. The distances between the planes of the atoms in a diffracted beam can be measured using Bragg's Law, n=2d sin where n denotes the order of the diffracted beam, d refers to the distance between adjacent planes of atoms, and θ is the angle of incidence of the X-ray beam.

The presence of $CaAl_{12}O_{19}$ (CA_6) and, thus, a saturation of the alumina grains with Ca was confirmed using X-ray diffraction (XRD). At room temperature, XRD measurements were taken using a Bruker D8 Advance diffractometer utilizing Cu-Kα (λ = 0.15064 nm). The XRD was performed at 40 kV and 40 mA. Scans at the 1°/min rate with step 0.02° between 20-90° [64] .

3.3.2. Scanning Electron Microscopy (SEM)

Electrons produced at the top of the column are accelerated down in scanning electron microscopy. To produce a focused beam, it passes through condenser lenses, condenser aperture, objective aperture, and objective lens. Scan coils above the objective lens control the position of the electron beam on the sample. SEM scans a focused electron beam across a surface to create an image. When electrons in the beam interact with the sample, they generate Auger electrons, secondary electrons, backscattered electrons, and cathodoluminescence (Figure 3.4). Detectors detect these signals, which provide information about surface topography and composition [65].

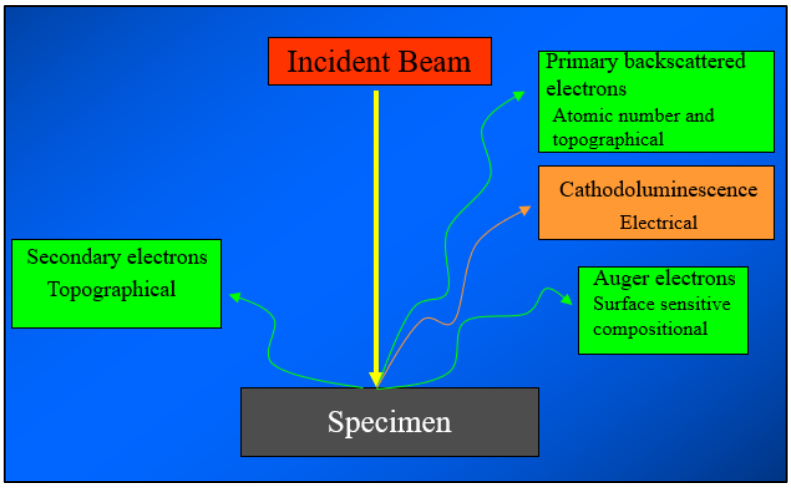

Figure 3. 1. Electron and specimen interactions.

A field-emission scanning electron microscope (FE-SEM, LEO Supra VP-55, Carl Zeiss, Germany) equipped with an energy dispersive X-ray spectrometer (EDS; QUANTAX, Xflash 6100, Bruker, Germany) was used to study the morphology and grain sizes. Chemical-elemental analyses were performed using energy-dispersive X-ray spectrometry. EDX was used to obtain an elemental mapping of the specified regions on the samples.

3.3.2.1. Sample Preparation for Microstructural Analysis in SEM

All sintered samples should be polished and etched before microstructural evaluation. A low-speed diamond saw was used to cut the samples perpendicular to the axial direction (Metkon, Bursa, Turkey). Since Si can cause contamination during sintering, the inner surfaces of the samples were polished. An automatic polisher was used in two steps to polish the surface (Metkon, Bursa, Turkey). First, various grit sizes of SiC emery papers (400, 600, 1000, 1200, 2000, 2500, 3000, and 4000) were applied, followed by diamond pastes of 9, 6, 3, and 1µ grain sizes. The polishing procedure is shown in Table 3.5.

Table 3. 5. Polishing Methods

	Step (1)	Step (2)
Abrasive	SiC	Diamond paste
Grit/Grain Size	400C, 600C, 1000C, 1200C, 2000C, 2500C, 3000C	9µ, 6µ, 3µ, 1µ
Lubricant	Water	Diamond lubricant

		(METKON)
Speed (rpm)	300	190

After polishing, grain boundaries were revealed by applying thermal etching. All the samples were thermally etched for 3 hours at 1300°C inside the covered alumina crucibles. The samples were attached to the SEM stubs using double-sticking carbon tapes, and the top surfaces of the specimens were connected to the conductive stubs using carbon dag suspension. The folded samples were coated with carbon to prevent charging under the electron beam (Agar automated SEM carbon coater).

The microstructural evaluation was carried out using a scanning electron microscope (SEM). The micrographs were acquired using a 3 KV voltage and an 9 mm working distance. Various images at different magnifications were acquired for each sample (5 kX, 7 kX, 10 KX, 15KX, 20KX, and 25KX) and an additional 30 KX from all samples to see the overall morphology. In order to establish the existence of certain phases in SEM samples, chemical analysis was performed. Micrographs were used to measure grain sizes in all samples accurately.

3.3.2.2. X-ray Spectroscopy Techniques in the SEM

The existence and quantity of elements in the specimen can be established by detecting the distinctive X-rays generated when the primary electron beam interacts with the atoms in the sample. When the electron beam hits the sample, it knocks an electron out of the inner shell of the atom. As a result, the atom is permanently ionized. The atom returns to its original state once another electron from higher energy outer shells occupies the electron vacancy. An X-ray photon will be generated to compensate for the energy of this electron transition. The technique for generating a distinctive X-ray photon because of electron beam-specimen interaction is depicted in Figure 3.5.

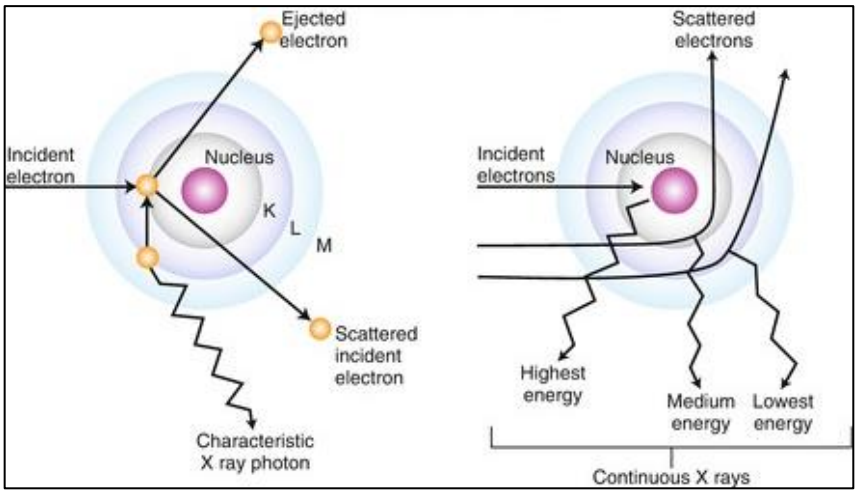

Figure 3. 2. The mechanism generates distinctive x-rays and continuous x-rays.

The difference between the energy levels of the inner and outer shell electrons determines the energy of the emitted X-ray photon. The generated X-ray is a unique identification for individual atoms. It is known as the distinctive X-ray since the difference in electron energy levels is understood for each element. Thus, the energy of the X-rays in EDS can provide qualitative and quantitative information on the chemical elements present in the material.

3.3.2.2.1. Energy Dispersive X-ray Spectroscopy (EDS)

The detection of distinctive X-rays of atoms proceeds with EDS spectroscopy by forming electron-hole pairs in a lithiated silicon detector. Because Si has a band gap of 1 eV, the number of electron-hole pairs formed is approximately equal to the energy of the incoming X-ray absorbed by the detector. The electrical current flow causes a pulse when a bias is applied across the semiconductor. The pulses are subsequently amplified and binned into several channels that reflect the X-ray energy spectrum. However, because of the existence of a thin protective window (typically composed of beryllium or carbon) at the surface of the detector, the discovery of light elements with atomic numbers less than sodium is challenging in EDS. It is because low-energy X-rays are absorbed.

Furthermore, the energy resolution of an EDS spectrum is on the scale of 100-200 eV, implying that the X-ray lines will appear as peaks of certain width in the spectrum. It is difficult to resolve the characteristic X-rays with energy differences nearing 200 eV due

to the low energy resolution. Moreover, the signal-to-noise ratio is low since X-ray detection depends on the electronics in the detector. Therefore, there is some uncertainty in the quantitative examination of the elements in the specimen [66, 67]. EDS elemental distribution mapping was performed on polished pellet samples in this study. EDS analysis was carried out at a working distance of 8 mm with a 15 kV accelerating voltage and a 30 μm objective aperture size to gather the distinctive X-rays efficiently. Depending on the average atomic number of the region being investigated, the depth of electron beam penetration into the material (depth of the interaction volume) was calculated to be between 2-3 microns. The elemental distribution maps from grains were gathered over a sufficiently enough time until the signal–to–noise ratio was satisfactory.

3.3.3. Transmission Electron Microscope (TEM)

In a transmission electron microscope (TEM), a thin sample of less than 200 nm is bombarded by an energetic beam of single-energy electrons (generally 200 kV). Electrons can transmit through the sample under high energy-thin sample conditions. Many signals were produced by the interaction of a high-energy electron beam with the specimen, as shown in Figure 3.6.

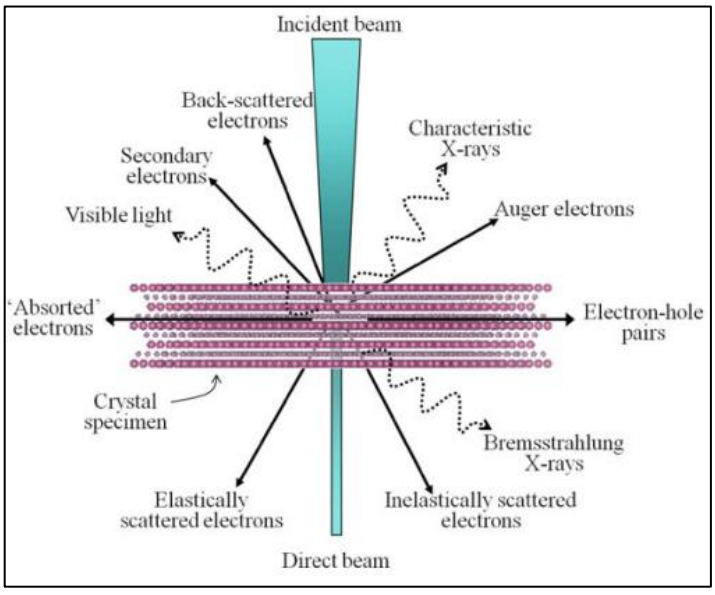

Figure 3. 3. The interaction of a high-energy electron beam with an electron-transparent (extremely thin) material generates signals. Most of them might be detected by TEM.

Electromagnetic lenses were used to magnify the signals before observing them on the phosphorous screen. Various TEM techniques are available to provide information about

the material. The crystallographic structure of a material can be determined using electron diffraction. Diffraction contrast is an amplitude-contrast imaging technique that provides information on the chemistry, microstructure, and defects of a sample. Phase-contrast imaging, such as high-resolution TEM, gives information about the microstructure of a material and its defects at an atomic resolution [65].

A parallel beam of high energy electrons (e.g., 200 kV) hits an ultrathin electron transparent specimen with a thickness of less than 100 nm in conventional TEM analysis. The interaction of the electron beam and the ultrathin specimen transmits a large portion of the beam through the specimen. Several signals are generated because of scattering events. The electron beam is converged into a probe equivalent to the size of atoms in scanning transmission electron microscopy (STEM). As a result, much localized structural information, such as atomic resolution imaging, chemical composition, dopant locations, and electronic structure of the material, is obtained at the scale of atomic columns. Conventional mechanical thinning, dimpling, and ion-milling (Gatan PIPS, Pleasanton, CA) were used to prepare TEM samples.

3.3.3.1. Sample Preparation for TEM Analysis

The traditional preparation methods used for TEM investigations aim to thin the sample into a thin slice or powder with a thickness of no more than 100 nm. Physical and chemical processes can be used to thin materials; however, mechanical techniques or ion beam ablation are the most frequent approaches. To generate a thin and well-prepared sample, a combination of various methods is commonly used [68].

The method should also be efficient, repeatable, and quick. The preparation process may cause artifacts in the measurement. Various mechanical preparation techniques can be employed depending on the material and features.

The primary techniques employed in this study for mechanical sample preparation include cutting, grinding, polishing, and dimpling. These methods create samples that can be considerably thinned using ion milling [68]. The sample is thinned using Ar^+ ions (PIPS^{TM}) to minimize preparation-induced artifacts to achieve electron transparency.

3.3.3.1.1. Ion Milling Techniques

The ion beam milling principle is based on bombarding the sample with strong ions, spilling material off its surface due to impact. This procedure happens in a gas plasma. The ions used should be inert, heavy, and not exist in the material, like argon [68].

To optimize sample thickness, the material is quickly removed from a large region at high voltage (> 4 keV) due to higher sputter rates. However, this process could result in artifacts, including redeposition, ion implantation, and the development of an amorphous layer [69].

Low-energy (3 eV) argon ions are used throughout the milling process. It improves sample quality and lessens surface damage from initial preparation steps. The following sections provide a detailed explanation of the devices used in this master thesis.

3.3.3.1.2. Precision Ion Polishing System

The Precision Ion Polishing System (PIPS^{TM}) from Gatan is a common instrument used for ion milling. Figure 3.7 displays the apparatus and a top-down perspective of the sample chamber.

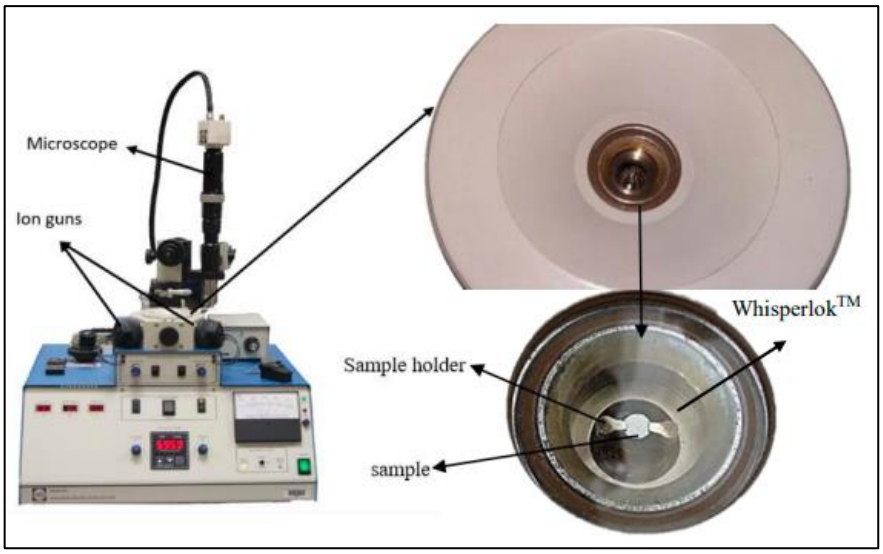

Figure 3. 4. The Whisperlok™ specimen transfer and sample holder are part of the ion milling PIPS™.

A Precision Ion Polishing System aims to ion mill samples that have already been mechanically thinned down by cutting, grinding, polishing, and dimpling procedures. The PIPS™ performs ion milling with a broad beam (> 0.01 μ) [70].

A PIPS™ consists mainly of the following parts:

Ion guns/Beam modulation

Sample holder

Vacuum system

Sample transfer lock (WhisperlokTM)

The PIPS™ "Aluminum DuoPost™" clamp-type sample holder is ideal for holding the sample at its outside edge. A rapid replacement of the sample is feasible since the WhisperlokTM technology avoids the need to vent the whole vacuum chamber. The vacuum inside the chamber is generated by a molecular drag pump supported by a diaphragm pump. The material can be removed by Ar^+ ions focused on a specific location and driven by an electric field. As a result, holes form, and the sample becomes electron transparent at its edge regions. The beam modulation can thin the sample from either one side or both. Two distinct ion guns produce Ar^+ ions with energies between 0.1 keV and 8 keV with adjustable angles from 0° to 10° to thin from both sides [70].

The milling rate is governed by parameters such as ion energy, atomic density, the incidence angle of the ion beam, and the crystalline structure of the sample. The milling rate generally increases with beam energy and angle, and more surface damage is caused by higher energy and angles.

The material and milling conditions influence the amorphous layers. Samples with more significant electron transparent regions and a thickness below 100 nm are frequently produced via PIPS^{TM} thinning. However, there is a linear relationship between the acceleration voltage and layer thickness and the incident angle and amorphous layer thickness [71].

3.3.3.2. Structural Analysis by Electron Diffraction Pattern

The crystal structure of the microstructure of the calcium-doped alumina sample was evaluated using the selected area electron diffraction pattern (SAED) approach. The different crystalline grains were slanted onto the low-indexed zone axis, and SAED patterns were acquired for each microstructural feature at a camera length of 100 cm. According to the relative size of the microstructure, a selected area aperture size between 10 and 50 μm in diameter was selected for use in the electron diffraction analysis.

The diffraction patterns were obtained from the extremely thin regions, allowing spot patterns to be formed. The spot SAED patterns in diffraction mode allowed the tilting of the crystal extremely close to the zone axis of interest. The geometry of the zone axis where the crystal was tilted was then determined using JEMS software to index the experimental SAED patterns. The phase that generated the spot diffraction pattern was determined by modeling the diffraction patterns from various crystal projections and comparing the simulated with the experimental ones.

3.3.3.2.1. Simulation of Electron Diffraction Patterns in JEMS

It is crucial to acquire the CIF files of the relevant phases to simulate the SAED patterns of the calcium hexaaluminate compounds on several zone axes. All the atoms in the spatial coordinates of the unit cell, correlating site occupancies, and Wyckoff positions are all contained in the CIF files. As shown in Figure 3.8, the CIF file was then imported into the JEMS software.

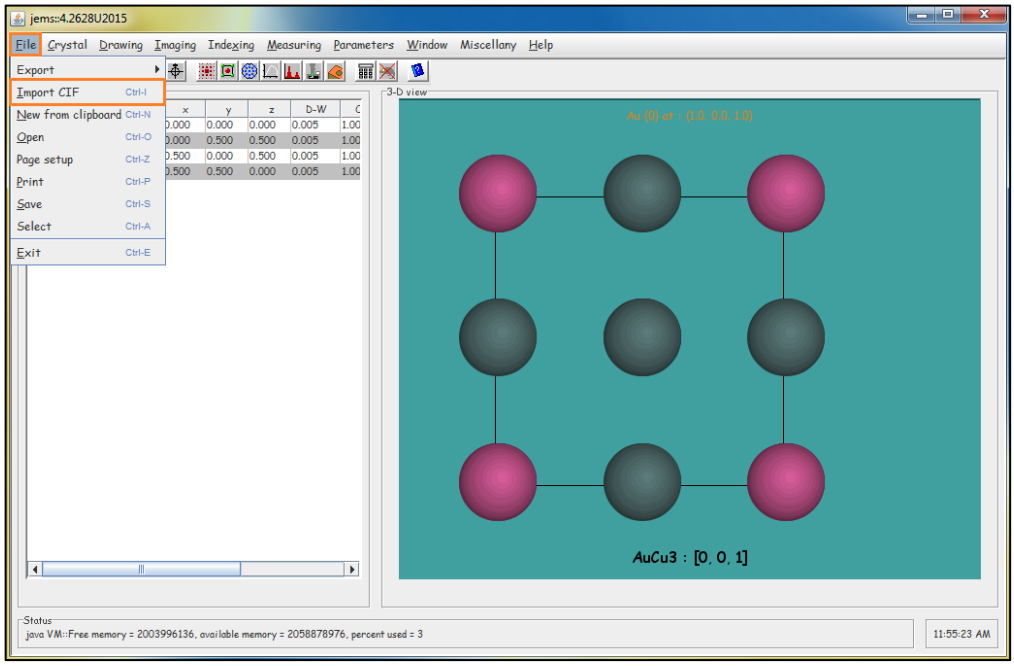

Figure 3. 5. The CIF file was loaded into the JEMS software.

The crystal structure of the phase will appear on the screen, as shown in Figure 3.9 when the CIF file of the phase of interest is imported. The CIF file for $CaAl_{12}O_{19}$ (mp-1227489) is displayed in this sample.

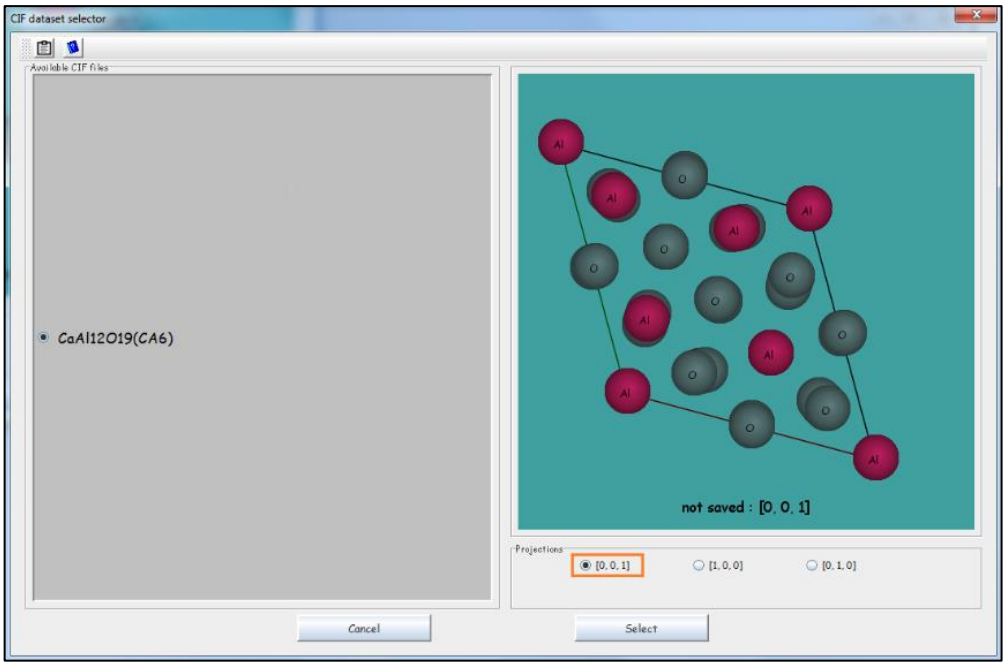

Figure 3. 6. Illustration of the crystal structure of the CA_6 phase in JEMS.

When the crystal structure was determined, the spot patterns of the imported crystal were formed along different zone axes by selecting the "draw diffraction pattern" tab. The discovery of a list of projections and their matching SAED patterns is seen in Figure 3.10. The diffraction patterns of the crystal from different zone axes can be observed through the list.

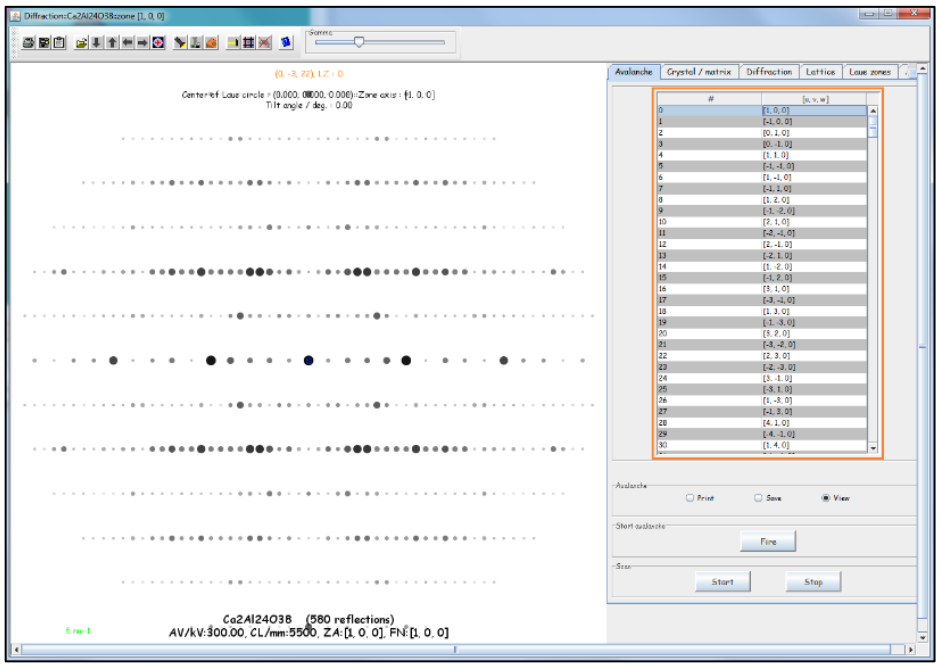

Figure 3. 7. List of various projections and their matching SAED patterns.

The observed diffraction patterns (DP) obtained at the microscope were uploaded into the software in the following step. The experimental DP was compared with simulated ones for phase analysis. In addition, the zone axis to which the crystal had been tilted was identified. After loading the experimental DP, the color of the simulated spot pattern was modified in the “Options tab” to distinguish between the experimental and simulated spots (Figure 3.11).

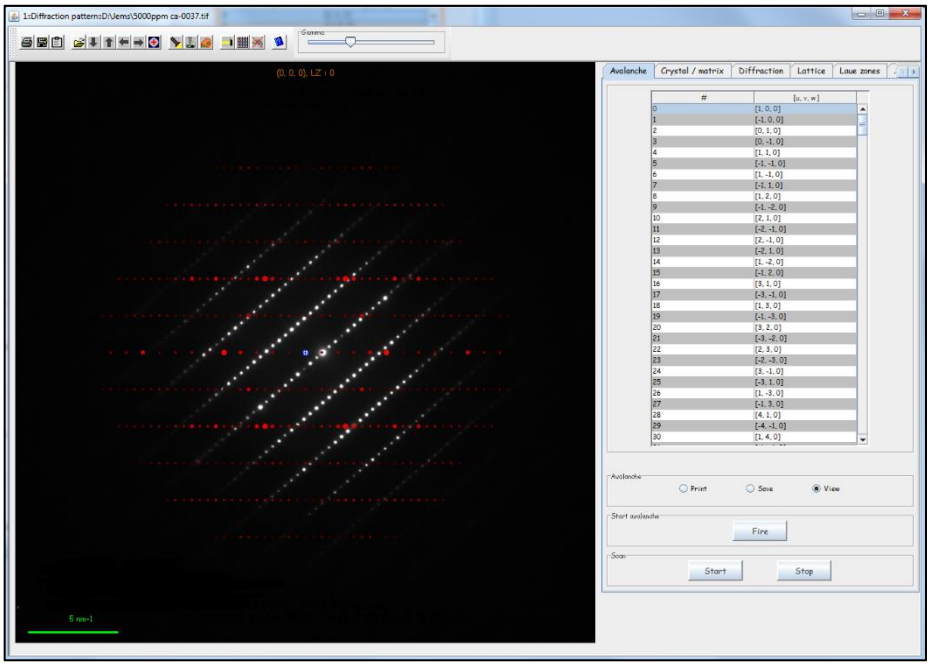

Figure 3. 8. Experimental DP overlaid on simulated spot patterns. The red dots reflect the simulated pattern.

Specifying the microscope configuration parameters, such as the accelerating voltage and the camera length by which the SAED pattern was gathered, is required. It is done in JEMS under the “Diffraction” tab, as shown in Figure 3.12.

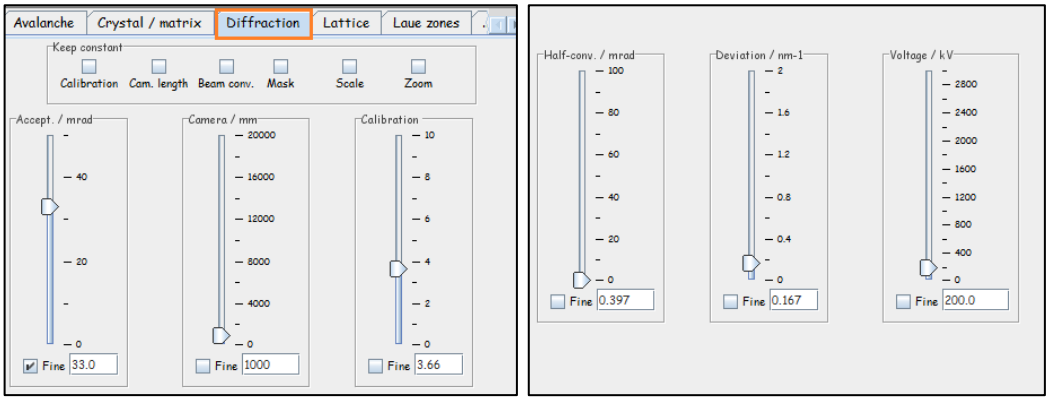

Figure 3. 9. The parameters for the microscope configuration to simulate the DP in JEMS.

The center of the two patterns (the transmitted spot) must correspond to begin the search/match. The experimental pattern was positioned above the center of the simulated patterns. Furthermore, under the “Normal tab” in JEMS, the orientation of the simulated pattern was modified to match the orientation of the experimental data, as illustrated in Figure 3.13.

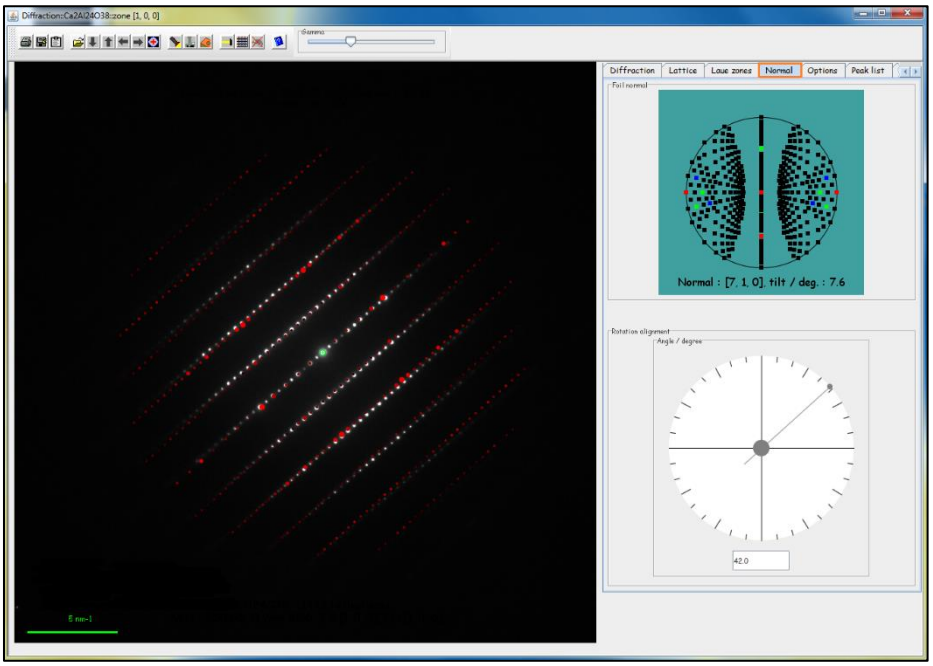

Figure 3. 10. Alignment of the simulated DP (red dots) with the experimental DP (white dots) for zone axis examination.

In order to determine the best match with the experimental DP, the simulated pattern is compared with the experimental DP, and the generated SAED patterns are examined from various zone axes of the CA_6 crystal. Figure 3.14 perfectly matches the experimental SAED pattern and the CA_6 pattern viewed from the [1 0 0] projection. It is indicated that the microstructure of the specimen that produced the SAED pattern is the CA_6 phase, which was tilted to [1 0 0] zone axis.

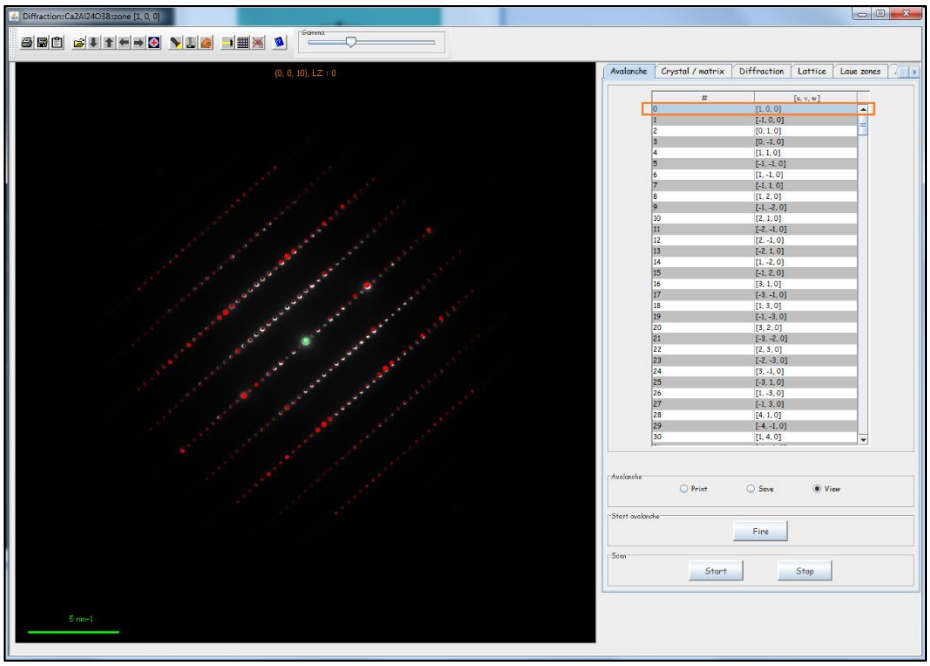

Figure 3. 11. Matching the experimental DP with simulated spot patterns in the DP database.

3.3.3.3. Atomic Resolution Imaging by Scanning Transmission Electron Microscopy (STEM)

After using an electron diffraction pattern to establish that the microstructural features are crystalline or amorphous and tilting a crystalline grain across a zone axis, the scanning mode was activated, in which the electron beam is focused to create a sub-angstrom spot size to investigate the material. Figures 3.15(a) and 3.15(b) show the signals produced due to an interaction between the electron beam with an ultrathin specimen and the relative positions of the STEM detectors, respectively. The generated signals will be scattered over a wide range of semi-angles after passing through the specimen.

The bright field detector (BF) is a solid disk that gathers the core transmitted beam with dispersed electrons scattered off-axis slightly to create bright field pictures. The intensity change in the STEM-BF image (contrast) is caused by transmitted beam absorption in the atomic positions, where the image is a dark sample on a bright background [70].

The camera length determines the inner and outer collection semi-angles for the annular dark field detectors (ADF), each ring-shaped (Figure 3.15). An annular detector below the specimen designed to gather forward-scattered electrons is used to provide dark field imaging in the STEM mode. The low-angle annular dark field (LAADF), one of two annular detectors, may also be able to catch diffracted beams when two annular detectors are provided. The diffraction amplitude determines the scale at which the intensity variation in the LAADF images changes.

The electrons are heavily scattered, inelastically off-axis of more than 50 mrad are collected by the high-angle annular dark field (HAADF) detector. The contrast of the images generated by the HAADF detector exposes information about the atomic number of the chemical elements contained in the specimen since the scattering angle, to such a high degree, is entirely proportional to the atomic number of the atoms present in the specimen [72]. The strong scatterers in a column of atoms seem bright in the HAADF image, whereas lighter components exhibit dark. The HAADF detector is not sensitive to thickness variation or phase shift between electron waves owing to the incoherent nature of the scattered electron probe [73].

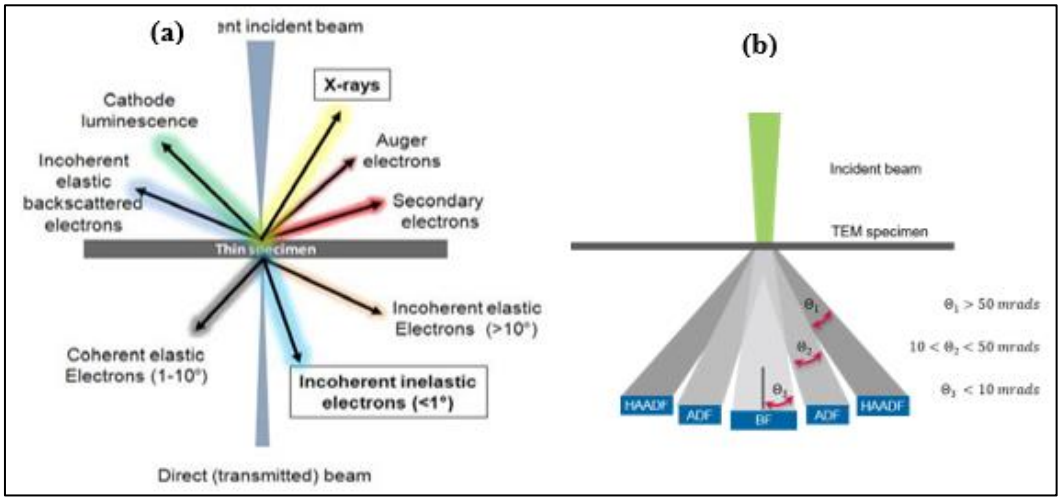

Figure 3. 12. Signal creation and detection using STEM. a) The interaction of the convergent beam with the thin specimen, b) the relative positions of the detectors in STEM.

At an accelerating voltage of 200 kV, atomic resolution STEM imaging was conducted in an aberration-corrected scanning transmission electron microscope (STEM; JEOL JEM-ARM-200CF) with a 40 µm condenser aperture and a 1Å probe size, and BF, ADF, and HAADF images were obtained.

3.3.3.3.1. Energy Dispersive X-ray Spectroscopy in STEM (STEM-EDS)

STEM-EDX analysis was used to evaluate the distribution of chemical components across the microstructure of alumina doped with 5000ppm CaO. The sintered specimens were prepared for STEM-EDX analysis using the PIPS process, as discussed in Section 3.3.4.1.2. The distribution of calcium dopant in the nanoscale within crystalline alumina grains and at grain boundaries was examined using the energy resolution in STEM-EDS analysis. An energy dispersive x-ray spectrometer and a Cs-aberration-corrected probe were used in a scanning transmission electron microscope (STEM; JEOL JEM-ARM 200CF) to map the distribution of elements with a nanoscale spatial resolution (EDXS, Jeol Centurio, 100 mm^2 EDXS detector). The probe size, accelerating voltage, and probe current were ca.2Å, 200 kV, and 700 pA, respectively.

4. RESULTS

4.1. Densification

According to Appendix A, the Archimedes method was used to calculate the densities of the sintered samples. Table 4.2 provides the %TD of the alumina samples sintered with 10,000 ppm CaO for different sintering times, and temperatures. The density of samples sintered at higher temperatures for lower times has not been evaluated in this study since the effect of sintering time and temperature is not the main focus.

Table 4. 1. Density of alumina samples doped with 10,000ppm CaO.

Sintering Time (h) / Sintering Temperature (°C)	1h	2h	4h	10h
1300°C	90.19	93.31	93.65	94.09
1400°C	-	-	-	96.58
1550°C	-	-	-	97.73

During sintering, achieving 100% density in these samples was impossible. For all densities at various sintering times and temperatures, the theoretical density of α-alumina (3.98 gr/cm^3) ranged from 90.19% to 97.73% as shown in Figure 4.1.

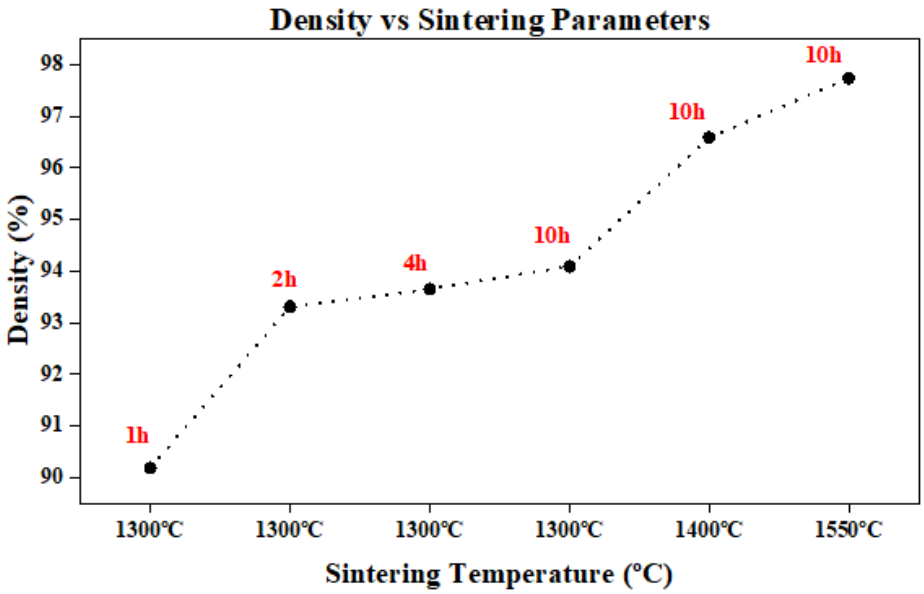

Figure 4. 1. Density measurement vs various sintering temperatures. Different sintering times were also labeled for each value.

Samples sintered at 1300°C for 1 hour had a density of around 90.19%. The density increased to 93.31%, 93.65%, and 94.09%, respectively, as the sintering time was extended to 2h, 4h, and 10h. Similar results were observed when the sintering temperature was changed. It was found that the density changes by 94.09%, 96.58%, and 97.73%, respectively, as the samples were sintered for 10h at different temperatures of 1300°C, 1400°C, and 1550°C.

4.2. XRD Measurements

Comparison patterns of XRD measurements for 10,000 ppm Ca-doped Al_2O_3 sample sintered at temperatures of 1300°C, 1400°C, and 1550°C for 10h is shown in Figure 4.2. In all these temperatures, the only phases identified by the XRD pattern are alumina (Al_2O_3) and calcium hexaaluminate (CA_6).

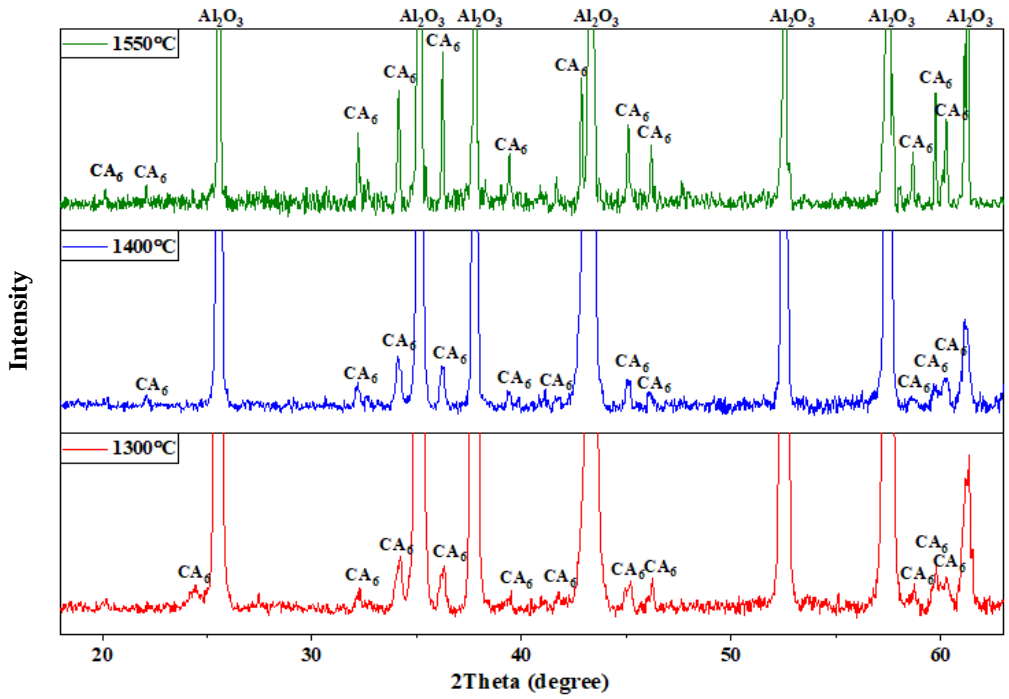

Figure 4. 2. XRD pattern indicating the presence of only calcium hexaaluminate (CA_6) and alumina confirms that the alumina grains are saturated with calcium.

To detect the early stages of CA_6 formation, different sintering times at 1300°C were tried. Comparison patterns of XRD measurements for sintered 10,000 ppm Ca-doped Al_2O_3 sample at 1300°C for various times of 1h, 2h, 4h, and 10h is shown in Figure 4.3. When the calcium doped alumina sample was sintered for 1 h, alumina (Al_2O_3) and different calcium aluminate phases like dicalcium aluminate ($Ca_2Al_2O_5$), and calcium aluminate (CA) were identified by the XRD pattern. At sintering time of 2 h, calcium dialuminate (CA_2) and alumina (Al_2O_3) became the only present phases in the sample. Finally, when the sample sintered at 1300°C for 4 h, the diffraction peaks of CA_2 and Al_2O_3 decline gradually, while the peaks of CA_6 become stronger. In 10 h, the only phases identified by the XRD pattern are alumina (Al_2O_3) and calcium hexaaluminate (CA_6) as mentioned above.

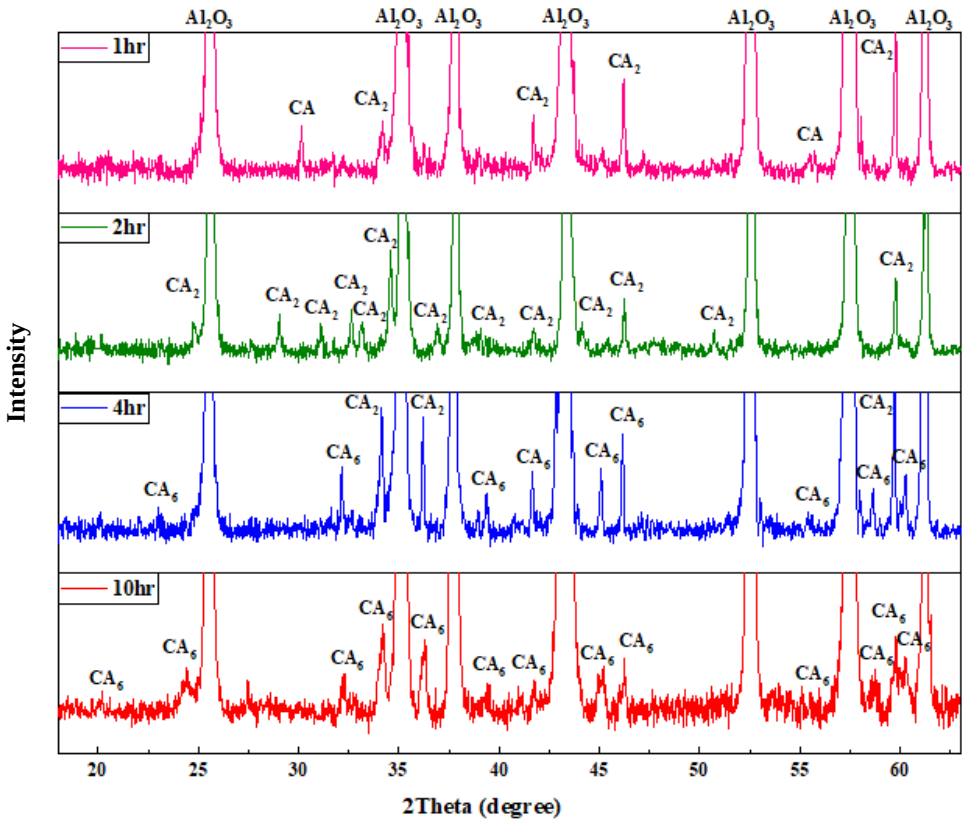

Figure 4. 3. XRD pattern indicating the presence of different calcium aluminates and alumina confirms that the alumina grains are saturated with calcium.

4.3. Microstructural Evolution

The chemical composition of the Al_2O_3 doped with 10,000 ppm CaO sample was studied at the micrometer level using an SEM (JEOL 6010 LV) equipped with an EDS detector. EDS mapping analysis, shown in Figure 4.4-4.6 are corresponded to the sintered samples for 10 h at different temperatures of 1300°C, 1400°C, and 1550°C, respectively. The Al and O distributions were homogenous, and the Ca distribution was not.

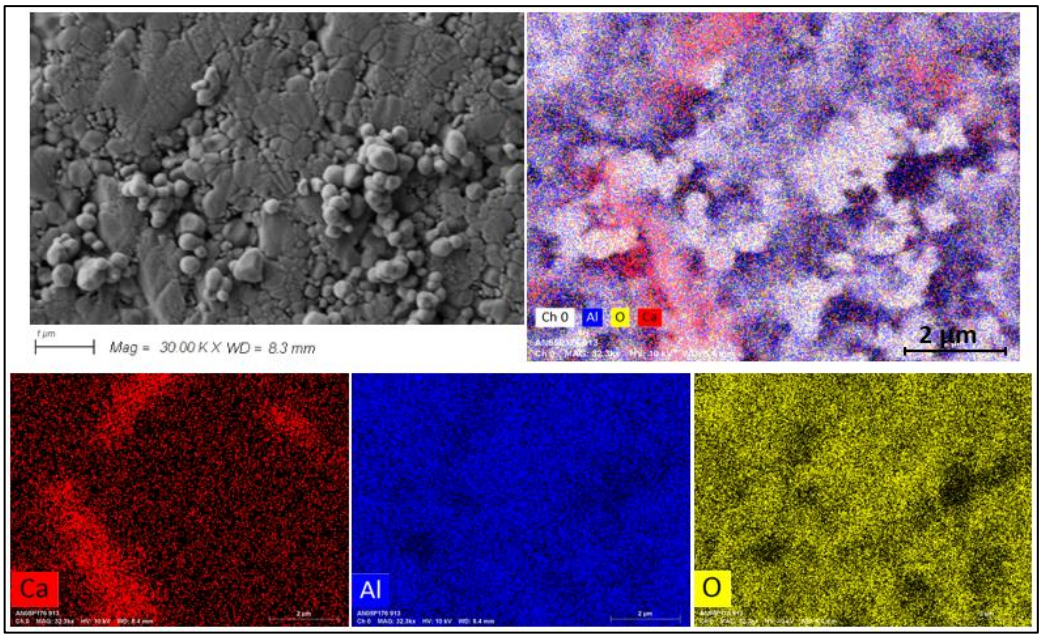

Figure 4. 4. Elemental mapping of Al, O, and Ca for Al_2O_3 doped with Ca sintered at 1300°C for 10 hours.

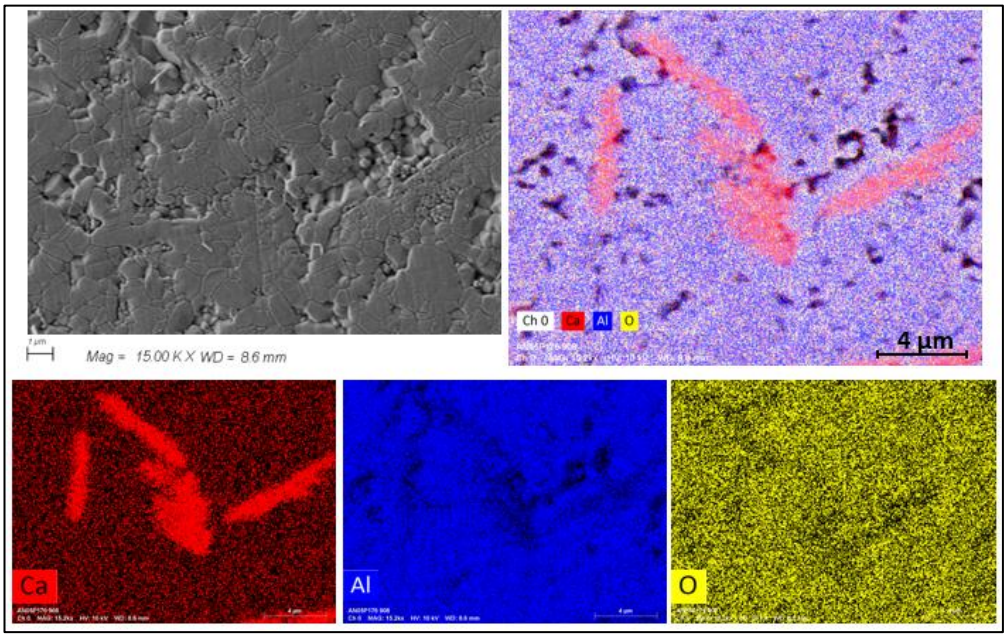

Figure 4. 5. Elemental mapping of Al, O, and Ca for Al_2O_3 doped with Ca sintered at 1400°C for 10 hours.

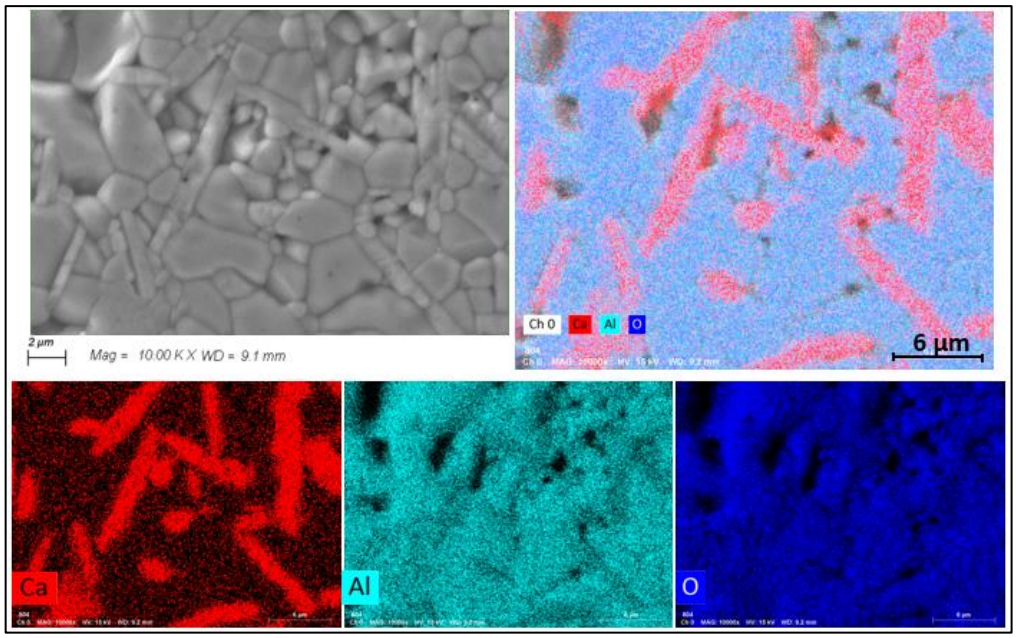

Figure 4. 6. Elemental mapping of Al, O, and Ca for Al_2O_3 doped with Ca sintered at 1550°C for 10 hours.

EDS analysis was also applied for the sintered samples at 1300°C for various times to study the calcium distribution in alumina. EDS mapping analysis, shown in Figure 4.7-4.9 are related to the sintered samples at 1300°C for 1h, 2h, and 4h, respectively.

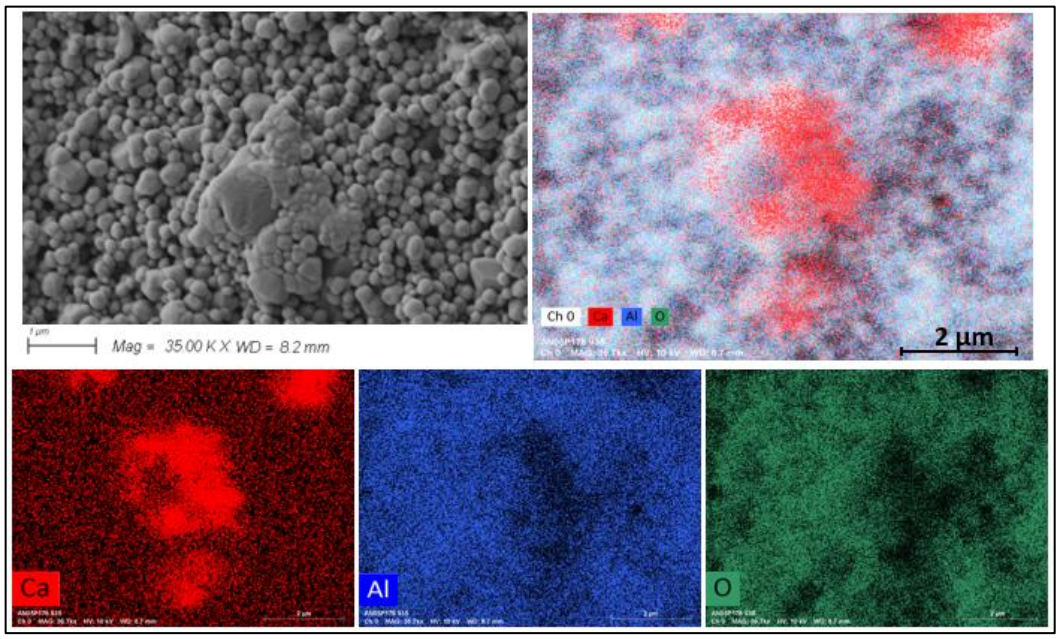

Figure 4. 7. Elemental mapping of Al, O, and Ca for Al_2O_3 doped with Ca sintered at 1300°C for 1 hour.

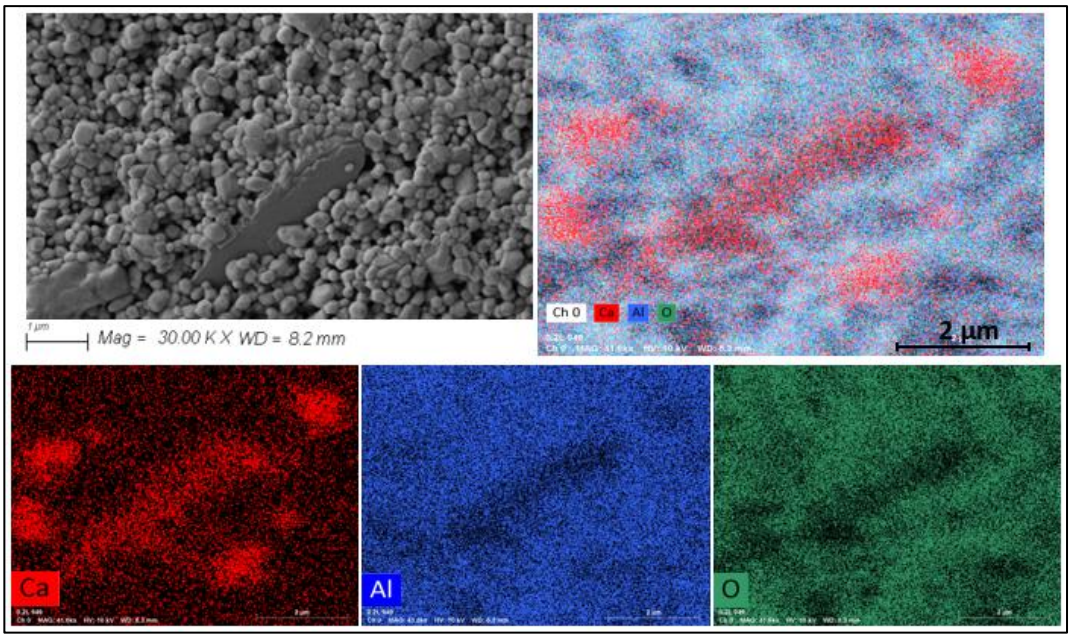

Figure 4. 8. Elemental mapping of Al, O, and Ca for Al_2O_3 doped with Ca sintered at 1300°C for 2 hours.

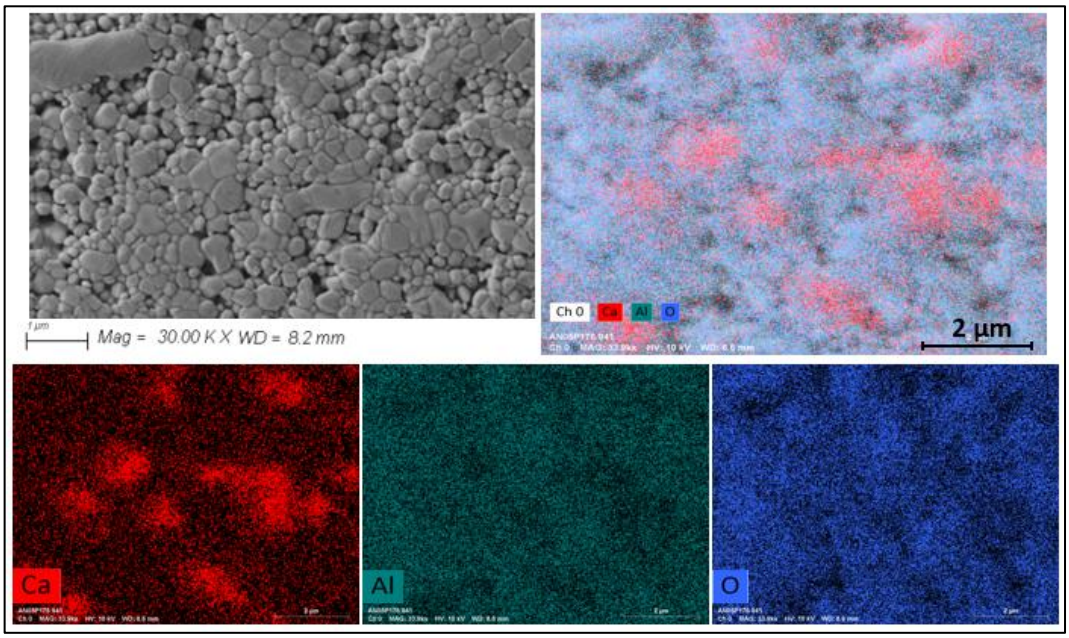

Figure 4. 9. Elemental mapping of Al, O, and Ca for Al_2O_3 doped with Ca sintered at 1300°C for 4 hours.

EDS measurements also confirmed the presence of CA_6 due to Table 4.3 and Figure 4.10. EDS analysis identified in the furnace-cooled sample confirms the XRD results in Figure

4.2 and 4.3, which show the presence of a two-phase microstructure in which the alumina is inevitably saturated with Ca.

Table 4. 2. EDS analysis of the CA_6 grains

Sintering Temperature (°C) & Time (h)	Mass Norm. (%)		
	Al	Ca	O
1300°C-1h	61.28	1.45	37.27
1300°C-2h	61.68	1.53	36.79
1300°C-4h	62.28	1.42	36.30
1300°C-10h	62.15	0.99	36.86
1400°C-10h	62.87	0.76	36.37
1550°C-10h	57.63	3.94	38.43

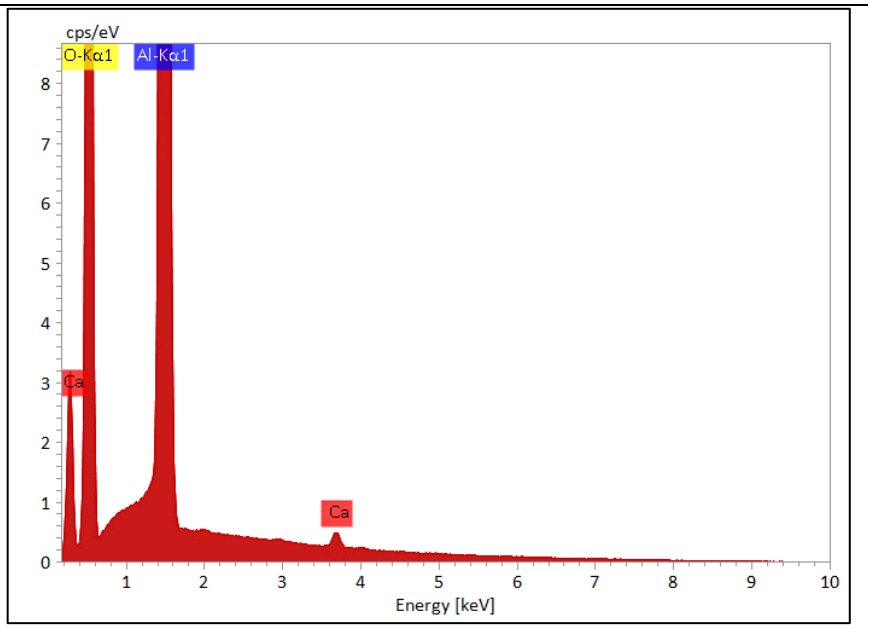

Figure 4. 10. EDS spectra from CA_6 precipitate.

A cross-section of the same sample that received thermal etching is shown in Figure 4.11 in a backscattered electron (BSE) SEM micrograph. The existence of CA_6 grains (elongated) and Al_2O_3 grains (darker contrast) can be clearly recognized as calcium-rich second-phase precipitates in this figure.

Figure 4. 11. BSE images of the Ca-saturated Al_2O_3 sample.

The formation of CA_6 precipitates can be seen clearly in Figure 4.11 as the large elongated grains with lighter contrast due to higher atomic weight (Z) of calcium atoms.
A scanning electron microscope (SEM) was applied to characterize the microstructure range magnifications.

Figure 4.12-4.14 include micrographs of the microstructure of samples sintered at different temperatures. In the initial stages of growth, the CaO-doped samples show an elongated (plate-like) morphology.

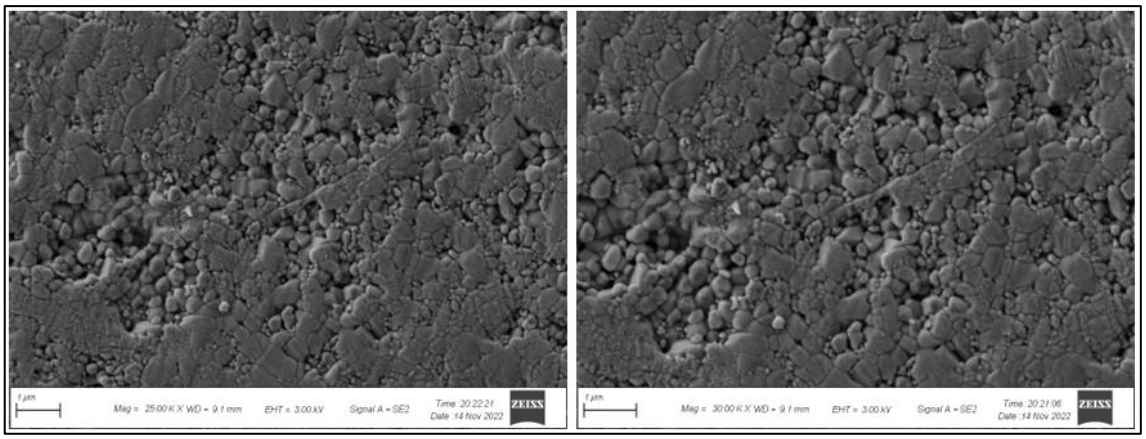

Figure 4. 12. SEM micrographs of the microstructure of Al_2O_3 doped with 10,000 ppm CaO sintered at 1300°C for 10 h.

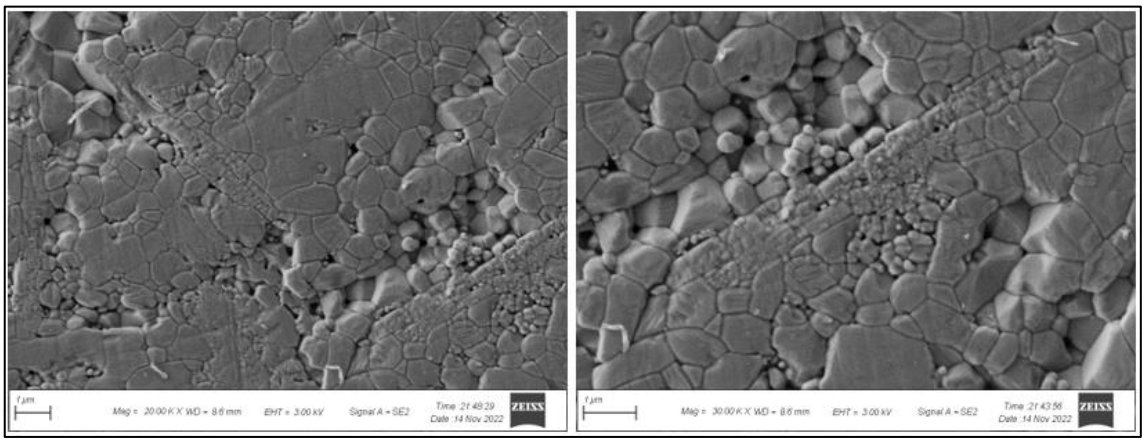

Figure 4. 13. SEM micrographs of the microstructure of Al_2O_3 doped with 10,000 ppm CaO sintered at 1400°C for 10 h.

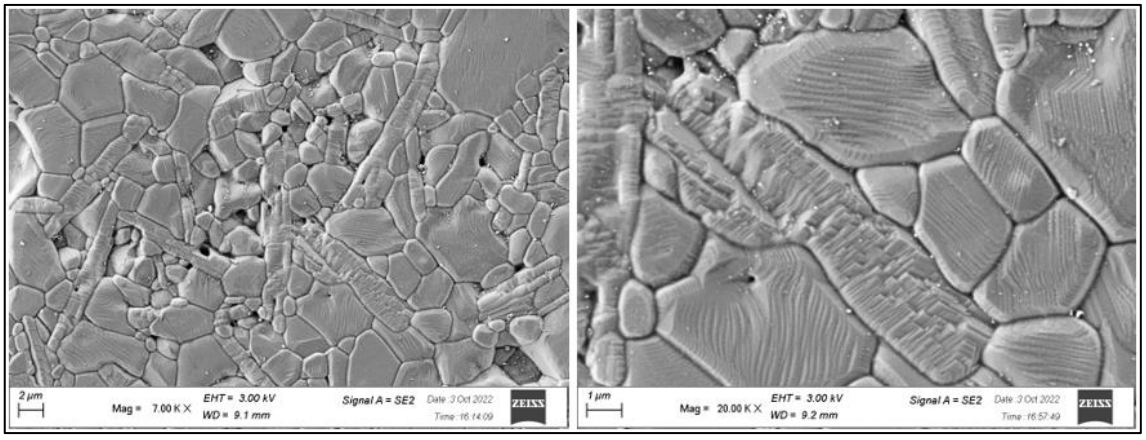

Figure 4. 14. SEM micrographs of the microstructure of Al_2O_3 doped with 10,000 ppm CaO sintered at 1550°C for 10 h.

Figure 4.12-4.14 show SEM images of the 10,000 ppm calcium doped samples that were sintered at the temperature range between 1300°C and 1550°C for 10 h. For the 1300°C sintering temperature, the grains were equiaxed with an average grain size of approximately 0.62 μm. At the sintering temperature of 1400°C, grains were mostly equiaxed in the sample and started to become elongated. In this temperature. The average grain size increased to 1.27 μm when the sintering temperature was raised to 1400°C. When the sintering temperture increased to 1550°C, grains became elongated and the average grain size increased to 3.86 μm. There was a big difference between small and large grains at this temperature. Samples in which the calcium concentration continued to be increased after precipitation showed bimodal grain size distribution. Table 4.4 shows the average grain size for small and large grains.

To find the early stage of formation of calcium precipitations, SEM was applied to characterize the microstructure of the sintered samples at 1300°C for various times. Figure 4.15-4.17 show the microstructural evolution of sintered samples at 1300°C for 1h, 2h, and 4h, respectively.

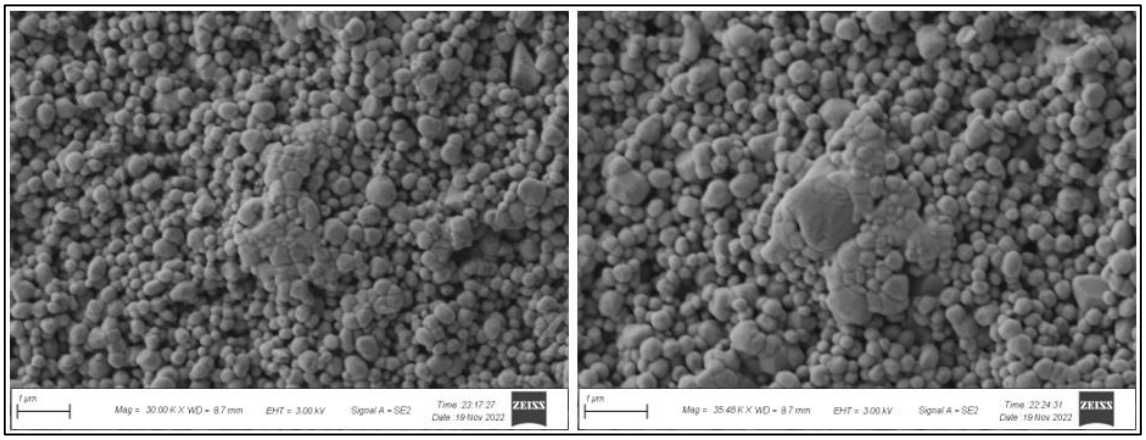

Figure 4. 15. SEM micrographs of the microstructure of Al_2O_3 doped with 10,000 ppm CaO sintered at 1300°C for 1 h.

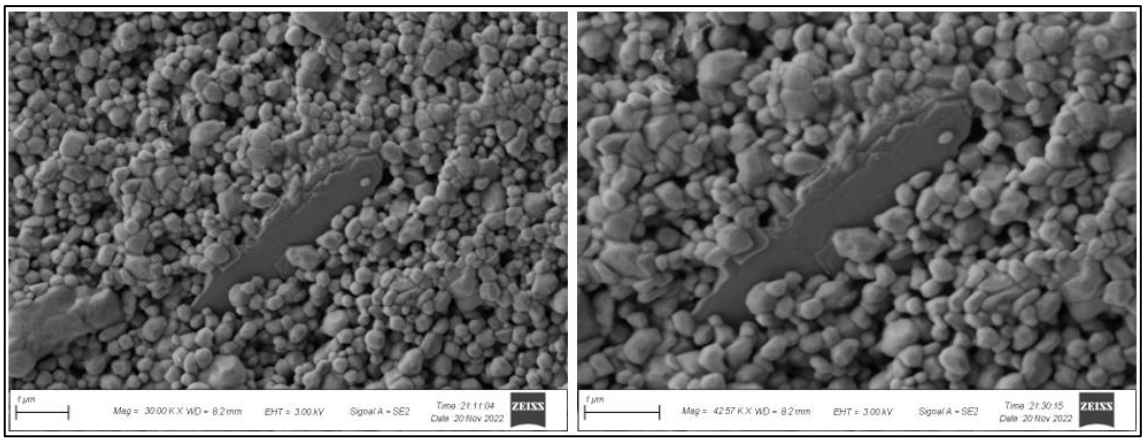

Figure 4. 16. SEM micrographs of the microstructure of Al_2O_3 doped with 10,000 ppm CaO sintered at 1300°C for 2 h.

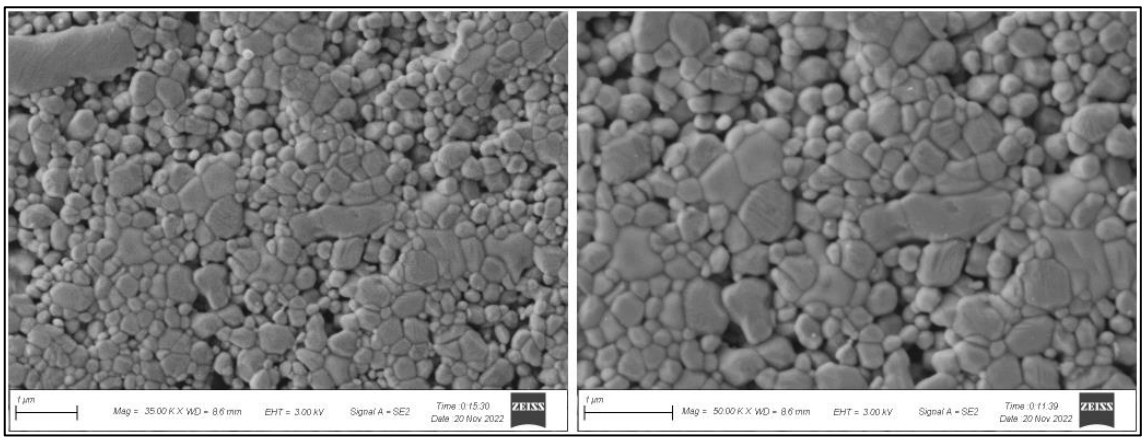

Figure 4. 17. SEM micrographs of the microstructure of Al2O3 doped with 10,000 ppm CaO sintered at 1300°C for 4 h.

The grains were equiaxed and reached an average grain size of about 0.38 μm after 1 h of sintering. Sintering for 2 h resulted in a slight increase in average grain size, which increased to 0.44 μm. The slab-like elongated grains were observed at this temperature and it is identified as a calcium percipitate. When the sintering time increased to 4 h, grains became larger again and the average grain size increased a little to 0.47 μm. The average grain size then increased since for the sintering for 10 h, the average grain size was 0.62 μm. (Figure 4.12).

The mean linear intercept technique was used to estimate the average grain sizes of the samples using these micrographs, detailed in Section 3.2.5.1. Table 4.4 provides the average grain sizes of alumina doped with calcium samples which were sintered at various conditions.

Table 4. 3. Average grain sizes of Al_2O_3 doped with calcium.

Sintering Temperature (°C) & Time (h)	Av. G of Small Grains (μ)	Av. G (μ)	Av. G of Large Grains (μ)
1300°C-1h	0.30	0.38	1.43
1300°C-2h	0.31	0.44	3.90
1300°C-4h	0.27	0.47	3.12
1300°C-10h	0.28	0.62	5.17
1400°C-10h	0.52	1.27	7.07
1550°C-10h	1.21	3.86	18.93

The grain sizes are reported in three columns in Table 4.4. In addition to the total average, the average size for both small and large grains (abnormally grown, elongated) are given for all samples.

Some impurity ions, like calcium, segregate strongly to grain boundaries in α-Al_2O_3. As a result, when calcium is added to alumina, the microstructure of the alumina changes, and this change is caused by an excess of calcium at the grain boundaries rather than a distribution of bulk calcium concentrations among the lattice and the grain boundaries. The mean linear intercept method can be used to predict calcium segregation in polycrystalline α-alumina. The following equation provides this concept:

$$\frac{\Gamma}{\Gamma_0-\Gamma} = K(X_t - \Gamma S_v \Omega) \tag{4.1}$$

Where Γ and Γ_0 represent the planar density of Ca at the boundary and accessible grain boundary adsorption sites, respectively. K indicates the partition coefficient, X_t is the total atomic concentration of calcium in the sample, S_v represents the entire grain boundary area per unit volume, and Ω denotes the volume per cation in α-Al_2O_3 equal to 0.0212 nm^3/cat.

The calcium coverage was anticipated to develop with rising total atomic calcium concentration in alumina during the calculations, and no second phase precipitate formation occurred. Therefore, Γ_{Ca} measurements that show multi-layer coverage at the boundaries can be identified, demonstrating that calcium can be absorbed at grain boundaries without saturation. Consequently, the approximations for the diluted concentrations are as follows:

$$\Gamma >> \Gamma_0 \text{ and } K >> 1$$

$$\Gamma = \frac{X_t}{S_v \Omega} = \frac{X_t G}{3\Omega} = \frac{X_t \bar{L}}{2\Omega} \tag{4.2}$$

G and $\bar{L}$ represent the grain size and the length of average grain size, respectively.

The values obtained using ICP-OES analysis were evaluated to determine X_t for the samples. Then, using these X_t values, Γ_{Ca} values were calculated, as displayed below:

$$AW_{Ca}=40.08 \text{ gr/mole}$$

$$AW_{Al}=26.98 \text{ gr/mole}$$

$$MW_{Al2O3}= 101.96 \text{ gr/mole}$$

According to the chemical analysis results, the X_t of the sample that contains 10,000 ppm (µg/g) calcium is:

$$X_t = \frac{Ca\ atoms}{Al\ atoms} = \frac{\frac{NA\left(Ca\frac{atoms}{mole}\right)\times 10000(gr\ Ca)}{AW_{Ca}\left(\frac{gr}{mole}\right)}}{\frac{NA\left(Al\frac{atoms}{mole}\right)\times 10^6(gr\ Al_2O_3)}{MW_{Al_2O_3}\left(\frac{gr}{mole}\right)}} \quad (4.3)$$

$$= \frac{\frac{6.02\times 10^{23}\left(Ca\frac{atoms}{mole}\right)\times 10000(gr\ Ca)}{40.08\left(\frac{gr}{mole}\right)\ Ca}}{\frac{2\times 6.02\times 10^{23}\left(Al\frac{atoms}{mole}\right)\times 10^6(gr\ Al_2O_3)}{101.96\left(\frac{gr}{mole}\right)\ Al_2O_3}} = 1.27\times 10^{-2}$$

Table 4.4 shows the results of the sintered samples at 1550 °C for 10 hours for 10,000 ppm Ca doped sample:

$$\text{Average grain size}=3.86\mu$$

Thus;

$$\Gamma_{Ca} = \frac{X_t G}{3\Omega} = \frac{3.86\times 10^3\times 1.27\times 10^{-2}}{3\times 2.12\times 10^{-2}} = 771.53 \text{ Ca/nm}^2$$

For all sintering temperatures and times, the calcium excess at the grain boundaries was computed and is shown in Table 4.5. The overall average grain size was employed for all calculations.

Table 4. 4. Calcium excess concentration.

Sintering Temperature (°C) & Time (h)	Γ_{Ca} (Ca atoms/nm^2)
1300°C-1h	77.23
1300°C-2h	87.91

1300°C-4h	93.36
1300°C-10h	124.45
1400°C-10h	252.71
1550°C-10h	771.53

Grain size versus Γ_{Ca} was plotted in order to study the sintered samples at various temperatures and times (Figure 4.18.).

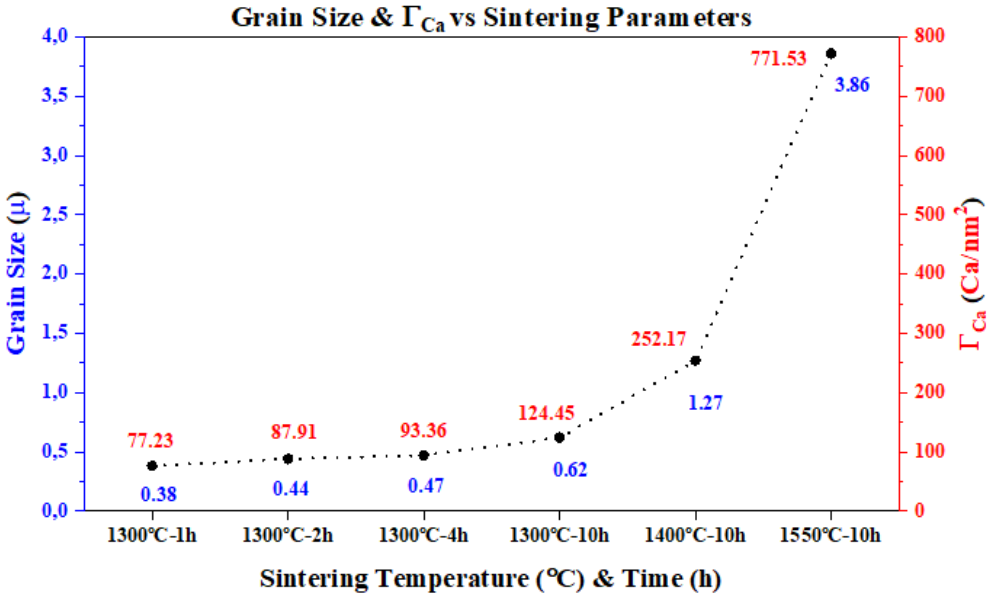

Figure 4. 18. Grain size versus Γ_{Ca} plot sharing the changes in the overall average grain sizes as a function of calcium excess concentrations at the grain boundaries three different temperatures and four different sintering times at 1300°C.

4.4. Grain Boundary Excess of Ca

The 2-D structure of a grain boundary and the amount of chemical excess determine the complexion of a grain boundary. Analytical TEM was performed on CaO-doped polycrystalline alumina to confirm the quantity of equilibrium Ca excess at the grain boundaries. Since the sample that was chosen had been sintered at 1550°C for 10 h, these precipitates were recognized as CA_6 by TEM. The selected-area diffraction (SAED) pattern recorded with the electron beam parallel to two zone axises of the CA_6 precipitate. Figure 4.19 displays the bright field TEM image of a PIPS specimen which was prepared.

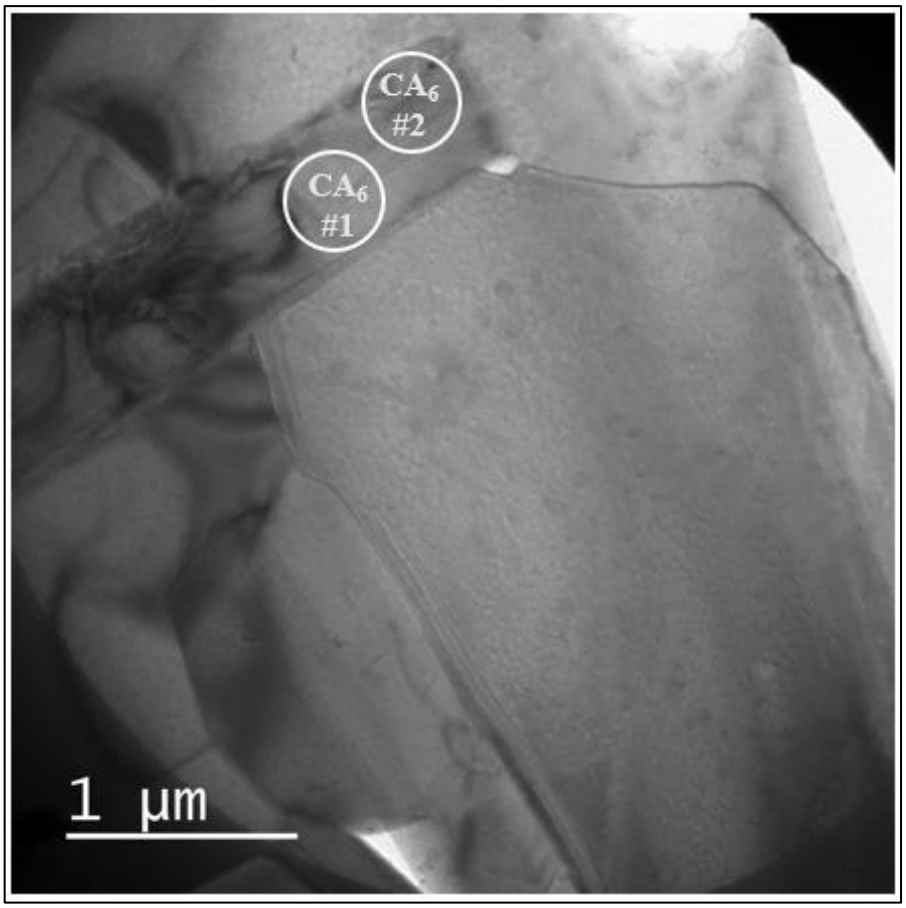

Figure 4. 19. Bright-field TEM micrograph of CA_6 precipitate.

Two diffraction patterns were identified and labeled as CA_6#1 and CA_6#2 for performing selected area electron diffraction (SAED) pattern analysis. The presence of CA_6 was confirmed by both EDS measurements in TEM and two selected area diffraction (SAD) patterns. The results of SAED pattern analysis of the microstructural features are shown in Figure 4.20. The labled zones were identified as CA6 based on the examination of the d spacings and the angles between the systematic rows of reflections observed in the DP images. The electron diffraction patterns of the crystalline grains were indexed by using JEMS software as described in section 3.3.4.2.1. The diffraction pattern attributed to CA_6#1 (Figure 4.20 (a)) was indexed to CA_6 phase when the grain is tilted to [1 0 0] zone axis. SAED pattern corresponding to CA_6#2 (Figure 4.20 (b)) is attributed to the zone axis of $[2\ \bar{3}\ 2]$ of CA_6 phase.

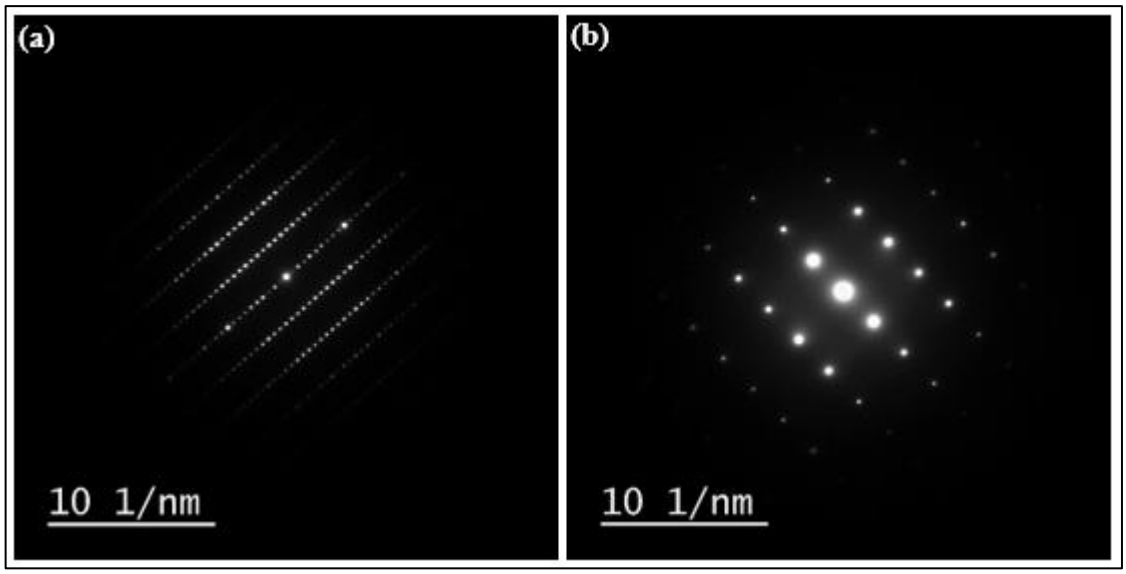

Figure 4. 20. SAED pattern analysis of the microstructural features corresponding to a) CA_6#1 and b) CA_6#2 in figure 4.18.

Figure 4.21 shows the comparison between the experimental and simulated electron diffraction patterns from both [1 0 0] and [2 $\bar{3}$ 2] projections. It was observed that there is a good fit between the experimental data and simulated point pattern (red dots).

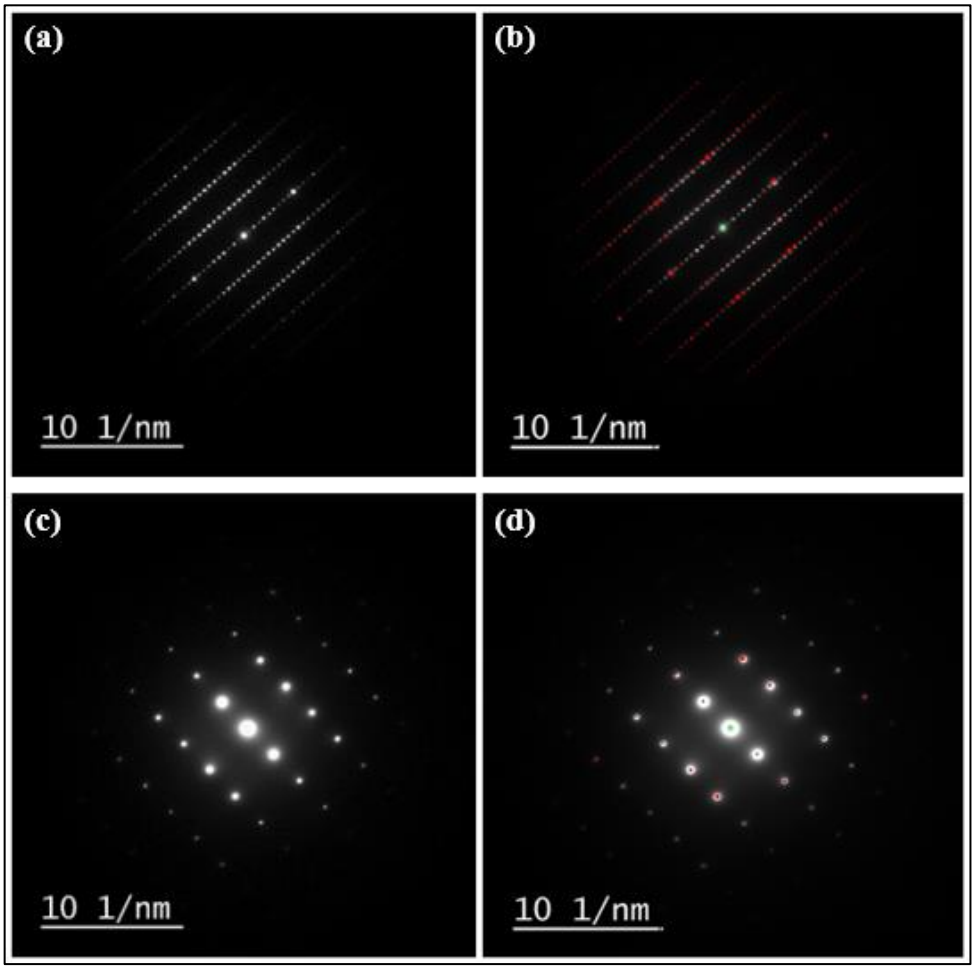

Figure 4. 21. Selected area electron diffraction pattern: a) experimental DP tilted to [1 0 0] projection, b) superimposition of simulated DP (red dots) on the experimental DP tilted to [1 0 0] projection, c) experimental DP tilted to [2 $\bar{3}$ 2] projection, and d) superimposition of simulated DP (red dots) on the experimental DP tilted to [2 $\bar{3}$ 2] projection.

EDS mapping analysis, shown in Figure 4.22 are related to an alumina doped sample with 5000 ppm calcium which is sintered at 1550°C for 10 h. The Al and O distributions were homogenous, and the Ca distribution was not. The EDS mapping indicates that the elongated grains have a microstructure with Ca-rich regions.

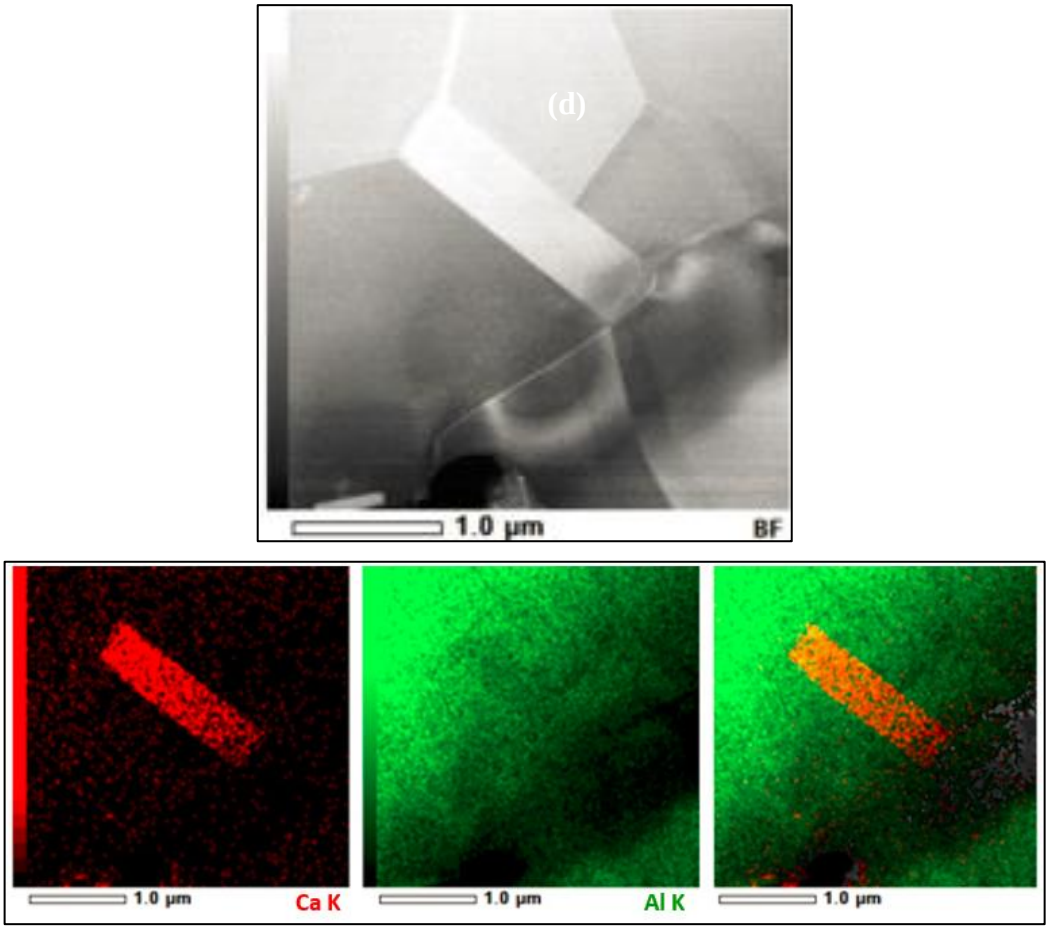

Figure 4. 22. STEM-EDS mapping analysis of 5000 ppm calcium doped alumina sintered at 1550°C for 10h.

In the STEM-HAADF image, some of the grain boundaries of alumina grains are observed with lighter contrast (Figure 4.23 (a)). To determine the excess of Ca at the grain boundary EDS measurements were conducted while rastering the electron beam over a constant area of the sample as shown in Figure 4.23 (b). EDS spectra in Figure 4.23(c)

also confirmed the presence of calcium at the grain boundary due to Table 4.6. It is shown the presence of Ca in around 1.89%.

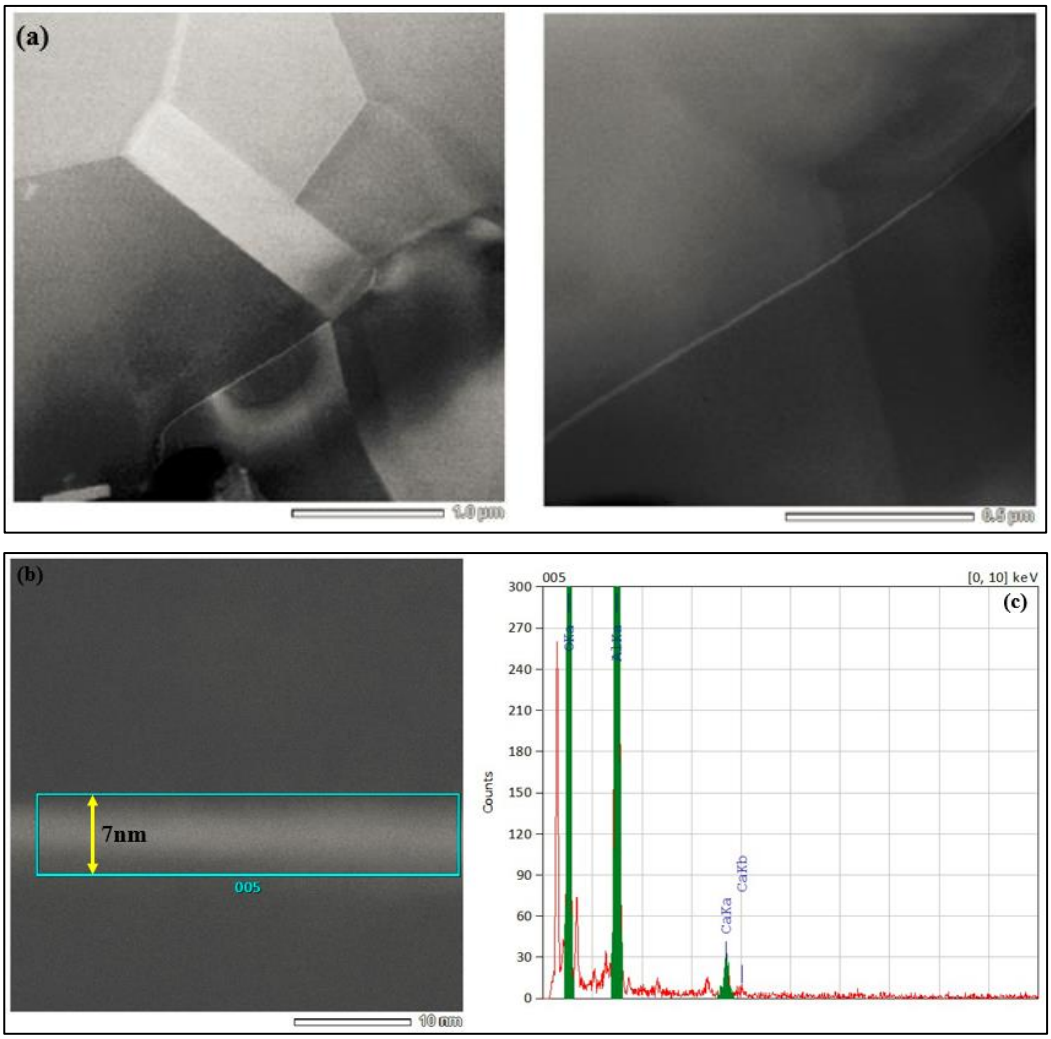

Figure 4. 23. a) STEM-HAADF image of a grain boundary showing lighter contrast. b) STEM-EDS area analysis from a grain boundary of 5000 ppm calcium doped alumina sintered at 1550°C for 10h. c) EDS spectra acquired from the interface region.

Table 4. 5. EDS analysis of the interface region

Element	Mass Norm. (%)
Al	98.11
Ca	1.89

5. DISCUSSION

The theoretical density of α-alumina for all densities in different sintering times and temperatures is shown in Figure 4. 1. It is identified that when sintering time and temperature increase, the density of the samples also rises.

During sintering, achieving 100% density in these samples was impossible. However, sintering temperature and time have significantly affected this value. Several aspects of the ultraclean sample processing might be identified as potential causes for the noticeably low final densities.

1. The powders used were extremely pure. To improve densification, liquid phase sintering was not used in this work.
2. No lubricants were employed to facilitate particle packing to prevent any contamination of the powders. During uniaxial pressing, the die walls were lubricated with pure liquid paraffin.
3. Before sintering, the dry compacts could not be packed to better green densities due to insufficient cold isostatic pressing pressure.

Figure 4. 2 illustrates the XRD results for the samples sintered for 10h at temperatures between 1300°C and 1550°C. In all samples, the only phases are CA_6 and Al_2O_3. XRD analysis for different sintering times were also tried at 1300°C (Figure 4. 3). The phases present in the sample sintered for 1h are CA, CA_2 and Al_2O_3. After being Sintered for 2h, a large quantity of CA_2 forms. Finally, in the sample sintered for 4h, the diffraction peaks of CA_2 and Al_2O_3 decline, while the peaks of CA_6 gradually become sharper. Thus, it can be inferred from the indicated XRD patterns and the crystal morphologies of the samples that the predominant reaction occurs between 1300°C and 1400°C and is $CA_2 + Al_2O_3 \rightarrow$

CA_6, which indicates that CA_6 is mainly generated at these temperatures. The CA_2-Al_2O_3 system has a primarily solid reaction in this temperature range based on the ion diffusion between reactants. As a result of the ion diffusion between the reactants, the CA_2-Al_2O_3 system undergoes a mostly solid reaction in this temperature range [73]. Two types of ion diffusions can be observed in the experiment: first, the diffusion of Al^{3+} in Al_2O_3 towards CA_2 lattices, and second, the diffusion of Ca^{2+} in CA_2 towards Al_2O_3 lattices. According to the CaO-Al_2O_3 phase diagram, if the Ca^{2+} diffuses into Al_2O_3 grains, it will generate a poor calcium phase, like CA_6 in the first steps. However, due to the XRD results, the rich calcium phases such as CA and CA_2, were formed foremost. This is only possible if the Al^{3+} in Al_2O_3 diffuses into CA_2 lattices. The crystal structure data and atomic locations of CA_2 are provided in Table 1. 3-Table 1. 4. The crystal structure of CA_2 contains two types of Al ions, four types of O ions, and one type of Ca ion. The coordination number of both types of Al ions is 4, while for Ca ions is 6. The CA_6 crystal structure has one Ca ion type and five different Al ions. Three are found in the trigonal bipyramidal voids, one in the octahedral voids and the other in the tetrahedral voids. Table 1. 5-Table 1. 6 display the atomic locations and crystal structure data for CA_6. When CA_2 combines with Al_2O_3 to generate CA_6, if Al^{3+} in Al_2O_3 diffuses into CA_2 lattices, the coordination number of Al changes from 4 to 6, while that of Ca changes from 6 to 12. This results in a change in the crystal structure. From the perspective of structural stability, once the coordination increases, the cations need more anions to coordinate, and the anions are also adjusted. This indicates that along with the diffusion of Al^{3+} towards CA_2 , more O^{2-} will move to Al^{3+} and Ca^{2+}, consuming much energy.

According to the EDS mapping analysis (Figure 4. 4-Figure 4. 9), the distribution of Al and O was homogenous, and the Ca distribution was not. It is observed that all the elongated grains have a microstructure of Ca-rich regions. Due to EDS measurements also confirmed the presence of CA6 due to Table 4.3 and Figure 4.10. EDS analysis identified in the furnace-cooled sample confirms the XRD results in Figure 4.2 and 4.3, which show the presence of a two-phase microstructure in which the alumina is inevitably saturated with Ca.

Table 4. 2 and Figure 4. 10, the alumina is inevitably saturated with Ca, and the presence of a two-phase microstructure was confirmed. When the calcium precipitates grow with the increase in the sintering temperature and time, it is evident from BS-SEM images (Figure 4. 11). The samples contain second-phase precipitates and elongated alumina grains.

The SEM micrographs were used to measure the average grain size for each sample Table 4. 3). The average grain size was applied to calculate the excess calcium concentrations (Γ_{Ca}) to compare the sintered samples at various temperatures and times (Table 4. 4). It can be seen that by increasing the sintering time the grain size increases. Morever, by increasing the sintering temperature the grain size increases as it was expected. The excess calcium concentrations where the elongated, anisotropic grain morphology, rapid grain growth, and second-phase precipitation started were identified using the micrographs. Moreover, Figure 4. 18 shows the average grain size (G) vs. excess calcium concentration (Γ_{Ca}) for the samples sintered at different sintering times and temperatures. The curve also indicated that the grains get coarser as the sintering temperature and time increase. The degree of calcium segregation is significantly influenced by grain size. According to equation 4.1, the predicted calcium concentration rises as the grain size grows. Several facts can be inferred using the curve in Figure 4. 18 and the corresponding micrographs:

i. Equiaxed grains were formed with low calcium excess concentrations at low sintering time and temperature of 1300°C and 1 h.
ii. As the time increased to 2 h, the grain morphology began to convert from equiaxed to elongated.
iii. The average grain size started to increse sharply when the sintering time was increased to 4h and 10h. This increse in average grain size ought to be connected to the number of calcium precipitates in the alumina matrix.
iv. When the sintering temperature was raised to 1400°C and 1550°C, the average grain size grew again. The equiaxial grain morphology began to change into an elongated grain morphology. Small grains were observed in the samples, which showed abnormal grain growth. The alumina grains were surrounded by these small anisotropic grains. Due to the EDS analysis, these tiny grains were detected as calcium-rich regions. These small grains should be connected to the formation of various calcium-rich films and layers at the grain boundaries.
v. Calcium aluminate precipitates were detected at all sintering temperatures. Calcium excess concentration were seen in the range of Γ_{Ca} =77.23 Ca atoms/nm^2 and Γ_{Ca} =771.53 Ca atoms/nm^2 since it was above its solubility limit. These calcium excess concentrations correlate to the calcium excess concentrations at which the grain morphology changed from equiaxed to elongated.

In a study that Altay and Gülgün conducted [74], some second phase precipitates with the chemistry of calcium hexa aluminate (CA_6) were generated when the calcium doping level was raised to exceed Γ_{Ca} ~ 20 Ca atoms/nm^2 or above Γ_{Ca} ~ 30 Ca atoms/nm^2. However, in addition to CA_6, calcium monoaluminate (CA) and calcium dialuminate (CA_2) phases were detected in this investigation. Because the morphology of these precipitates was indistinguishable from that of alumina grains, the solubility limit at the grain boundaries of Ca atoms/nm^2 calculated by Altay is most likely an overestimation and should be considerably lower. As a result, all of the calcium excess quantities found in this study exceed the saturation limit.

As was previously indicated, the CA_2 film reacts with the alumina substrate to produce CA_6. Since the sample that was heated to 1550°C for 10 h was chosen for TEM observations, CA_2 did not exist in the sample, and the only phase present was CA_6. Two diffraction patterns confirmed the presence of CA_6 precipitates (Figure 4. 20) and EDS mapping measurements in TEM (Figure 4. 22). The elongated grains have a calcium-rich microstructure. In a STEM-HAADF image of the general specimen morphology (Figure 4. 23 (a)), some of the grain boundaries were found to contain a crystalline intergranular film of thickness on the order of 7 nm (Figure 4. 23 (b)). EDS area analysis was conducted on the same interface. Figure 4. 23 (c) shows the EDS spectra acquired from this interface region by rastering the beam over a 7×36 nm^2 area. Ca is visible, with a peak significantly above the background level. Quantification of EDS (Table 4. 5) resulted in a thin film containing around 1.89% calcium indicates a two-phase microstructure in which the alumina grains are inevitably saturated with Ca.

6. CONCLUSION

One of the primary concerns in creating the required features is microstructural evolution of a material. It is important to control the effects of impurities in a material to maintain the grain structure. The influence of calcium on the structure of alumina sintered at various temperatures and times was investigated in this thesis. The grains were uniformly shaped and small for low calcium levels at all sintering conditions. The grains elongated only when the sintering time and temperture increased. The calcium segregation in the alumina matrix is thought to be the cause of the elongated morphology. The samples sintered at 1550°C exhibited abnormal grain growth having elongated morphology. In these samples, high grain size caused a significant increase in calcium concentration. Despite the elongated grains, the samples sintered at 1400°C displayed no abnormal grain growth. Only a few grains had abnormal growth, which had no effect on the overall average grain size. The elongated grain morphology in α-alumina is therefore explained by the presence of calcium above a specific concentration.

Calcium is one of the most prevalent impurities identified in commercial Al_2O_3. Calcium atoms strongly segregate to grain boundaries and form CA_6 second-phase precipitates, as explained in chapter 4. To study the formation of these CA_6 precipitates, the structure of the interface between the Ca-containing phase and the Al_2O_3 during the reaction was also examined. A small amount of CA_6 is produced by the reaction system between CaO and Al_2O_3 in samples sintered at 1300°C for 4 hours, while a significant amount is produced in samples sintered at 1300°C and above for 10 hours. CA_6 is formed through the process $CA_2 + 4Al_2O_3 \rightarrow CA_6$. There is a diffusion process of Al^{3+} in Al_2O_3 towards

calcium lattices in which the calcium rich phases (CA, CA_2) were first formed. Poor calcium phase (CA_6) was developed as the amount of Al diffusion increased.

FUTURE WORK

More experiments should be done on the effects of calcium on alumina grain boundary mobility and the transitions that occur as sintering time and temperature increase. In the future, it may be possible to get TEM observations of other calcium aluminate phases, particularly CA_2. HRTEM results should be also done when both CA_2 and CA_6 phases are present and the discussed reaction between CA_2 and Al_2O_3 occurs. Some new techniques are necessary to study the calcium vs. aluminum distribution profile in calcium aluminate phases since it appears to be going against the phase diagram.

7. REFERENCES

1. Powers, J. and A. Glaeser, *Grain boundary migration in ceramics.* Interface Science, 1998. **6**(1): p. 23-39.
2. Villars, P. and L. Calvert, *Pearson's handbook of crystallographic data for intermediate phases.* American Society of Metals, Cleveland, OH, 1985.
3. Levin, I. and D. Brandon, *Metastable alumina polymorphs: crystal structures and transition sequences.* Journal of the american ceramic society, 1998. **81**(8): p. 1995-2012.
4. Kronberg, M., *Plastic deformation of single crystals of sapphire: basal slip and twinning.* Acta Metallurgica, 1957. **5**(9): p. 507-524.
5. Lee, W. and K. Lagerlof, *Structural and electron diffraction data for sapphire (α-al2o3).* Journal of electron microscopy technique, 1985. **2**(3): p. 247-258.
6. Swanson, H.E., *Standard X-ray diffraction powder patterns*. Vol. 25. 1953: US Department of Commerce, National Bureau of Standards.
7. Handwerker, C.A., P.A. Morris, and R.L. Coble, *Effects of chemical inhomogeneities on grain growth and microstructure in Al2O3.* Journal of the American Ceramic Society, 1989. **72**(1): p. 130-136.
8. Bae, S.I. and S. Baik, *Determination of critical concentrations of silica and/or calcia for abnormal grain growth in alumina.* Journal of the American ceramic society, 1993. **76**(4): p. 1065-1067.
9. Berry, K.A. and M.P. Harmer, *Effect of MgO solute on microstructure development in Al2O3.* Journal of the American Ceramic Society, 1986. **69**(2): p. 143-149.
10. Bennison, S.J. and M.P. Harmer, *Effect of MgO solute on the kinetics of grain growth in A12O3.* Journal of the American Ceramic Society, 1983. **66**(5): p. C-90-C-92.
11. Özgür, Ü., V. Avrutin, and H. Morkoç, *Zinc oxide materials and devices grown by molecular beam Epitaxy*, in *Molecular Beam Epitaxy*. 2018, Elsevier. p. 343-375.
12. Kitayama, M. and A.M. Glaeser, *The Wulff shape of alumina: III, undoped alumina.* Journal of the American Ceramic Society, 2002. **85**(3): p. 611-622.
13. Lagerquist, V. and S. Wallmark, *AZ "Westgren; X-Ray Study of the System CaO-Al2O3-SiO2"(in Ger) Anorg.* Chem, 1937. **234**: p. 1-16.

14. Goldsmith, J.R., *The Compound CaO· 2Al₂O₃.* The Journal of Geology, 1948. **56**(1): p. 80-81.
15. Boyko, E. and L. Wisnyl, *The optical properties and structures of CaO. 2Al2O3 and SrO. 2Al2O3.* Acta Crystallographica, 1958. **11**(6): p. 444-445.
16. Cockayne, B., D.S. Robertson, and W.E. Bardsley, *Growth defects in calcium tungstate single crystals.* British Journal of Applied Physics, 1964. **15**: p. 1165-1169.
17. Goodwin, D. and A. Lindop, *The crystal structure of CaO. 2Al2O3.* Acta Crystallographica Section B: Structural Crystallography and Crystal Chemistry, 1970. **26**(9): p. 1230-1235.
18. Gross, S., *The Mineralogy of the Hatrurim Formation Israel*. 1977: Geological Survey of Israel.
19. Weber, D. and A. Bischoff, *The occurrence of grossite (CaAl4O7) in chondrites.* Geochimica et Cosmochimica Acta, 1994. **58**(18): p. 3855-3877.
20. Weber, D. and A. Bischoff, *Grossite (CaAl4O7)-a rare phase in terrestrial rocks and meteorites.* European Journal of Mineralogy, 1994: p. 591-594.
21. Nurse, R., J. Welch, and A.J. Majumdar, *The CaO-Al 2 O 3 system in a moisture-free atmosphere.* BRIT CERAM SOC TRANS, 1965. **64**(9): p. 409-418.
22. KATO, K., *Verfeinerung der Kristallstruktur von CaO 6Al_2O_3.* N. Jb. Miner. Abh., 1968. **109**(3): p. 192-200.
23. Collongues, R., et al., *Magnetoplumbite-related oxides.* Annual Review of Materials Science, 1990. **20**(1): p. 51-82.
24. Braun, P.B., *The crystal structures of a new group of ferromagnetic compounds.* Philips Res. Rep., 1957. **12**: p. 491-548.
25. Beevers, C. and M.A. Ross, *The crystal structure of "beta alumina" Na2O· 11Al2O3.* Zeitschrift für Kristallographie-Crystalline Materials, 1937. **97**(1-6): p. 59-66.
26. Iyi, N., S. Takekawa, and S. Kimura, *Crystal chemistry of hexaaluminates: β-alumina and magnetoplumbite structures.* Journal of Solid State Chemistry, 1989. **83**(1): p. 8-19.
27. Utsunomiya, A., et al., *Structure refinement of CaO· 6Al2O3.* Journal of Solid State Chemistry, 1988. **75**(1): p. 197-200.
28. Kang, S.-J.L., *Sintering: densification, grain growth and microstructure*. 2004: Elsevier.
29. Barsoum, M., *Fundamentals of ceramics*. 2019: CRC press.
30. Kingery, W.D., H.K. Bowen, and D.R. Uhlmann, *Introduction to ceramics*. Vol. 17. 1976: John wiley & sons.
31. Voorhees, P.W., *The theory of Ostwald ripening.* Journal of Statistical Physics, 1985. **38**(1): p. 231-252.
32. Hillert, M., *On the theory of normal and abnormal grain growth.* Acta metallurgica, 1965. **13**(3): p. 227-238.
33. Mullins, W.W., *Two-dimensional motion of idealized grain boundaries.* Journal of Applied Physics, 1956. **27**(8): p. 900-904.
34. Gibbs, J.W., *On the equilibrium of heterogeneous substances.* 1879.
35. Intrater, J., *A Review of: "Sintering of Ceramics, M. N. Rahaman".* Materials and Manufacturing Processes, 2007. **23**(1): p. 111-112.
36. Manassidis, I. and M.J. Gillan, *Structure and energetics of alumina surfaces calculated from first principles.* Journal of the American Ceramic Society, 1994. **77**(2): p. 335-338.

37. Chiang, Y.-M., D.P. Birnie, and W.D. Kingery, *Physical ceramics: principles for ceramic science and engineering*. Vol. 409. 1997: Wiley New York.
38. Laplace, P.S. and H.H. Harte, *A treatise of celestial mechanics*. 1805: R. Milliken.
39. Burke, J. and D. Turnbull, *Recrystallization and grain growth.* Progress in metal physics, 1952. **3**: p. 220-292.
40. Rahaman, M., *Sintering of ceramics. 2008*. Boca raton, Florida, USA: CRC Press Taylor & Francis Group.
41. Brook, R., *Pore-Grain Boundary Interaction and Grain Growth.* Journal of the American Ceramic Society, 2006. **52**: p. 56-57.
42. Gülgün, M.A., et al., *Cation segregation in an oxide ceramic with low solubility: yttrium doped α-alumina.* Interface Science, 2002. **10**(1): p. 99-110.
43. Bae, I. and S. Baik. *Abnormal grain growth in alumina*. in *Materials Science Forum*. 1996.
44. Coble, R.L., *Transparent alumina and method of preparation*. 1962, Google Patents.
45. Bennison, S.J. and M.P. Harmer, *Grain-Growth Kinetics for Alumina in the Absence of a Liquid Phase.* Journal of the American Ceramic Society, 1985. **68**(1): p. C-22-C-24.
46. Gluzer, G. and W.D. Kaplan, *Particle occlusion and mechanical properties of Ni–Al2O3 nanocomposites.* Journal of the European Ceramic Society, 2013. **33**(15-16): p. 3101-3113.
47. Gavrilov, K.L., et al., *Silica and magnesia dopant distributions in alumina by high-resolution scanning secondary ion mass spectrometry.* Journal of the American ceramic society, 1999. **82**(4): p. 1001-1008.
48. Baik, S. and C.L. White, *Anisotropic calcium segregation to the surface of Al2O3.* Journal of the American Ceramic Society, 1987. **70**(9): p. 682-688.
49. Mukhopadhyay, S., et al., *Segregation of Magnesium and Calcium to the () Prismatic Surface of Magnesium-Implanted Sapphire.* Journal of the American Ceramic Society, 1988. **71**(5): p. 358-362.
50. Kaplan, W.D., et al., *Ca Segregation to Basal Surfaces in α-Alumina.* Journal of the American Ceramic Society, 1995. **78**(10): p. 2841-2844.
51. Cook, R.F. and A. Schrott, *Calcium segregation to grain boundaries in alumina.* Journal of the American Ceramic Society, 1988. **71**(1): p. 50-58.
52. Dillon, S.J. and M.P. Harmer, *Relating grain-boundary complexion to grain-boundary kinetics I: calcia-doped alumina.* Journal of the American Ceramic Society, 2008. **91**(7): p. 2304-2313.
53. Dillon, S.J. and M.P. Harmer, *Relating grain boundary complexion to grain boundary kinetics II: silica-doped alumina.* Journal of the American Ceramic Society, 2008. **91**(7): p. 2314-2320.
54. Park, C.W. and D.Y. Yoon, *Effects of SiO2, CaO2, and MgO additions on the grain growth of alumina.* Journal of the American ceramic society, 2000. **83**(10): p. 2605-2609.
55. Avishai, A. and W.D. Kaplan, *Intergranular films in metal-ceramic composites and the promotion of metal particle occlusion.* International Journal of Materials Research, 2004. **95**(4): p. 266-270.
56. Akiva, R., A. Katsman, and W.D. Kaplan, *Anisotropic grain boundary mobility in undoped and doped alumina.* Journal of the American Ceramic Society, 2014. **97**(5): p. 1610-1618.

57. Avishai, A. and W.D. Kaplan, *Intergranular films at metal–ceramic interfaces: Part II–calculation of Hamaker coefficients.* Acta materialia, 2005. **53**(5): p. 1571-1581.
58. Gottstein, G. and L. Shvindlerman, *On the retardation of grain boundary motion by small particles.* Scripta Materialia, 2010. **63**(11): p. 1089-1091.
59. Altay, A. and M.A. Gülgün, *Microstructural evolution of calcium-doped α-alumina.* Journal of the American Ceramic Society, 2003. **86**(4): p. 623-29.
60. Taylor, H.F., *Cement chemistry*. Vol. 2. 1997: Thomas Telford London.
61. Yi, H., et al., *Preparation of calcium aluminate matrix composites by combustion synthesis.* Journal of materials science, 2002. **37**(21): p. 4537-4543.
62. Akiva, R., A. Berner, and W.D. Kaplan, *The solubility limit of CaO in α-alumina at 1600° C.* Journal of the American Ceramic Society, 2013. **96**(10): p. 3258-3264.
63. Bacon, D. and G.E. Dieter, *Mechanical Metallurgy*. 1988, McGraw-Hill Education.
64. Cullity, B.D., *Elements of X-ray Diffraction*. 1956: Addison-Wesley Publishing.
65. Brandon, D. and W.D. Kaplan, *Microstructural characterization of materials*. 2013: John Wiley & Sons.
66. Goldstein, J.I., et al., *Scanning electron microscopy and X-ray microanalysis*. 2017: Springer.
67. Goodhew, P.J., J. Humphreys, and R. Beanland, *Electron microscopy and analysis*. 2000: CRC press.
68. Ayache, J., et al., *Sample preparation handbook for transmission electron microscopy: techniques*. Vol. 2. 2010: Springer Science & Business Media.
69. Barna, A., B. Pécz, and M. Menyhard, *Amorphisation and surface morphology development at low-energy ion milling.* Ultramicroscopy, 1998. **70**(3): p. 161-171.
70. Williams, D.B., C.B. Carter, and C.T.E. Microscopy, *A textbook for Materials Science.* Transmission Electron Microscope, 2009.
71. Süess, M., E. Mueller, and R. Wepf, *Minimization of amorphous layer in Ar+ ion milling for UHR-EM.* Ultramicroscopy, 2011. **111**(8): p. 1224-1232.
72. Pennycook, S.J. and P.D. Nellist, *Scanning transmission electron microscopy: imaging and analysis*. 2011: Springer Science & Business Media.
73. Voyles, P., et al., *Atomic-scale imaging of individual dopant atoms and clusters in highly n-type bulk Si.* Nature, 2002. **416**(6883): p. 826-829.
74. Altay, A. and M.A. Gülgün. *Calcium in alpha-alumina: the myth and some EM observations*. in *Key Engineering Materials*. 2004. Trans Tech Publ.

APPENDIX A

A.1. Density Measurement

The size, morphology, distribution, and porosity can all be determined by the microstructure. The apparent density (total weight/total volume, including pores) is compared to true density (total weight/volume of solids) to determine the total porosity of sample.

The true density of a single-phase material is easily determined. The density of a crystalline material can be estimated using the crystal structure and lattice parameters since the atomic weight of each component is specified. True density can also be estimated by analyzing pore-free samples with a liquid having known density. This can be done for single crystals by weighing the material in air, suspending it in a liquid, and then using Archimedes' method to get the volume. The pycnometer method must be used to calculate the density of complex mixtures and porous substances after the sample has been thoroughly pulverized up to remove closed pores. After the sample has been weighed in a Pycnometer bottle with a known volume, the liquid is applied to produce a known volume of liquid plus solid, and a new weight is then obtained. Both the specimen and liquid must be boiled in vacuum to ensure that the solid penetrates all particles. The volume of solid sample can be estimated from the weight differences acquired, which also provide the liquid volume. If the sample is weighed in air initially (W_a), then heated in boiling water for 2 hours to fill the open pores completely with water, total porosity and open-pore volume can be determined simultaneously. The weight of the saturated piece is defined after cooling (i) suspended in water (W_{sus}) and (ii) in air (W_{sat}). The sample volume is obtained by subtracting these two values. The open-pore volume is also determined by the difference between saturated and dry weights [5].

The Archimedes' method was performed to estimate the densities of the samples. The wetting liquid was distilled water at 21°C. The masses of the compacts were weighed first in air, secondly in distilled water, and the densities were determined using ASTM standard c 20-92:

$$\rho_{spec} = \frac{mass_{air} \times \rho_{water}}{mass_{air} - mass_{water}} \quad \text{(A.1.1)}$$

Where ρ_{water} is the theoretical density of water which is 1 gr/cm^3. The percentage theoretical densities (%TD) were then determined:

$$\%TD = \frac{\rho_{spec}}{\rho_{alumina}} \times 100 \quad \text{(A.1.2)}$$

Where $\rho_{alumina}$ is the theoretical density of alumina which is 3.97 gr/cm^3.

A.2. Grain Size Measurements

A.2.1. Determination of Average Grain Size Using the Mean Linear Intercept Method

In the shown micrograph, there are 66 grains that intersected the randomly drawn lines. (See Figure A.2.1. 1) There are 4 lines in all, each measuring 7.7 cm. Thus;

7.7 × 4 = 30.8 cm total length of the lines

30.8 / 66 = 0.466 cm/cut

According to the SEM image:

10 microns = 1.8 cm

So;

L = 0.466 × (10 / 1.8) = 2.59 micron

Average grain size =L × 1.5 = 3.88 microns

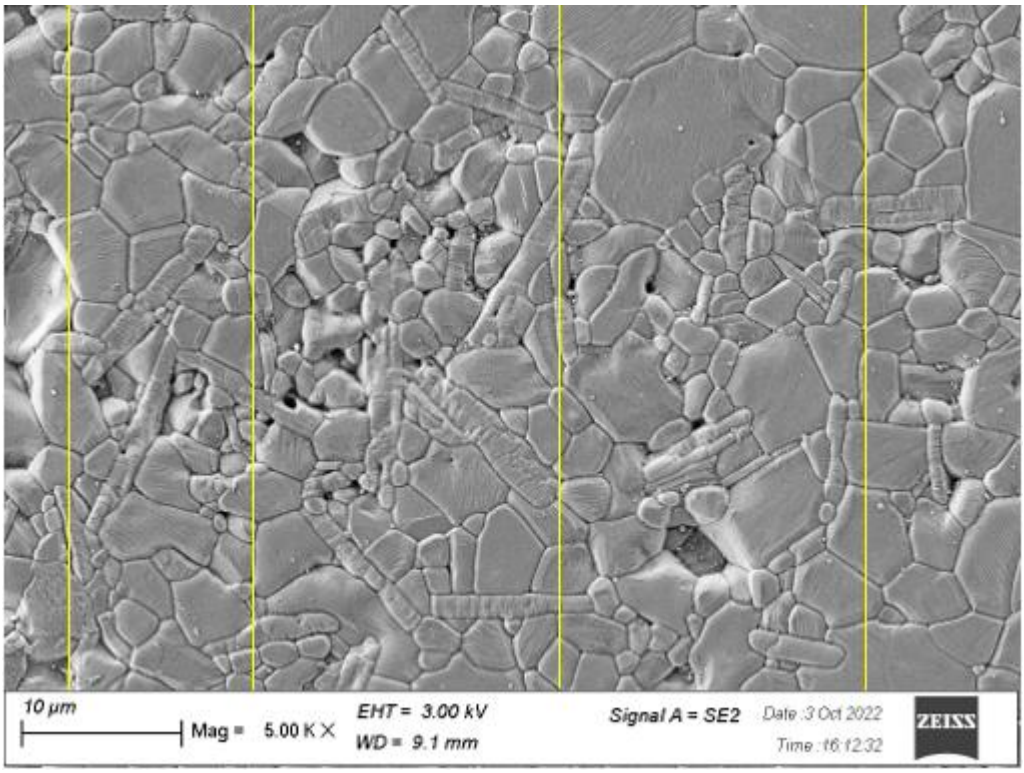

Figure A.2.1. 1. Determination of the average grain size of Ca doped sample sintered at 1550°C for 10 h.

A.2.2. Determination of Small and Large Grain Average Grain Size

The mean linear intercept approach, which is described in Appendix A.2, was used to determine the average grain size of small grains. The total number of small grains intersected by the yellow lines drawn at randomly on the displayed image in Figure A.2.2. 1 is 42. Total length of the lines is 8.9 cm. Therefore;

8.9 / 42 = 0.211 cm / cut

From the SEM image:

10 microns = 1.8 cm

So;

$\bar{L}_{\text{small grains}}$ = 0.211× (10 / 1.8) = 1.17 microns

Average grain size $_{\text{small grains}}$ =$\bar{L}$ ×1.5 = 1.76 microns

The numerical average was calculated after measuring the grain sizes of the large grains one by one. The grain size of large grains was always determined by the largest dimension

of the anisotropic grains. Figure A.2.2. 1 shows that there are 8 large grains (red lines), with a combined grain size of 17.8 cm. Thereby;

17.8 / 8 = 2.23 cm / large grain

From the SEM micrograph:

10 microns = 1.8 cm

$\bar{L}_{\text{large grains}}$ =2.23× (10 /1.8) = 12.4 microns

Average grain size $_{\text{large grains}}$ =$\bar{L}$. 1.5 = 18.6 microns

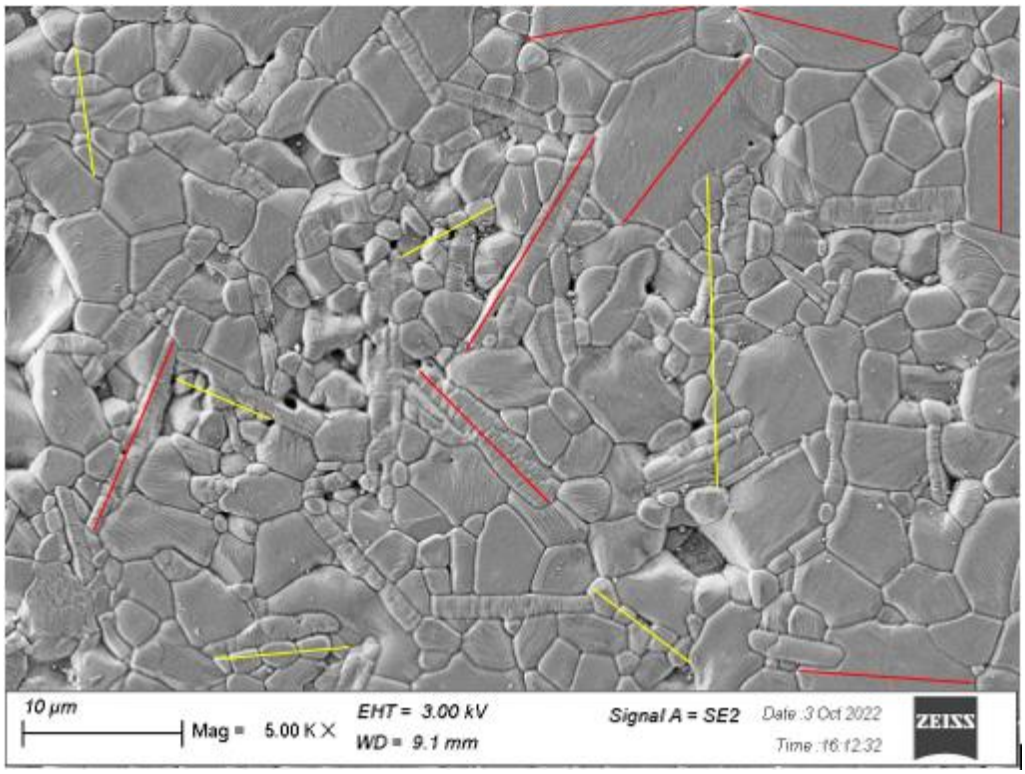

Figure A.2.2. 1. Measurement of the average grain size of small and large grains of Ca doped sample sintered at 1550°C for 10 h.

APPENDIX B

In this section, sem micrographs of the calcium-doped α-Al_2O_3 samples sintered at various temperatures for various times are exhibited in various magnifications.

B.1. Micrographs of the calcium doped α-Al_2O_3 sintered at 1300°C for 1 hours

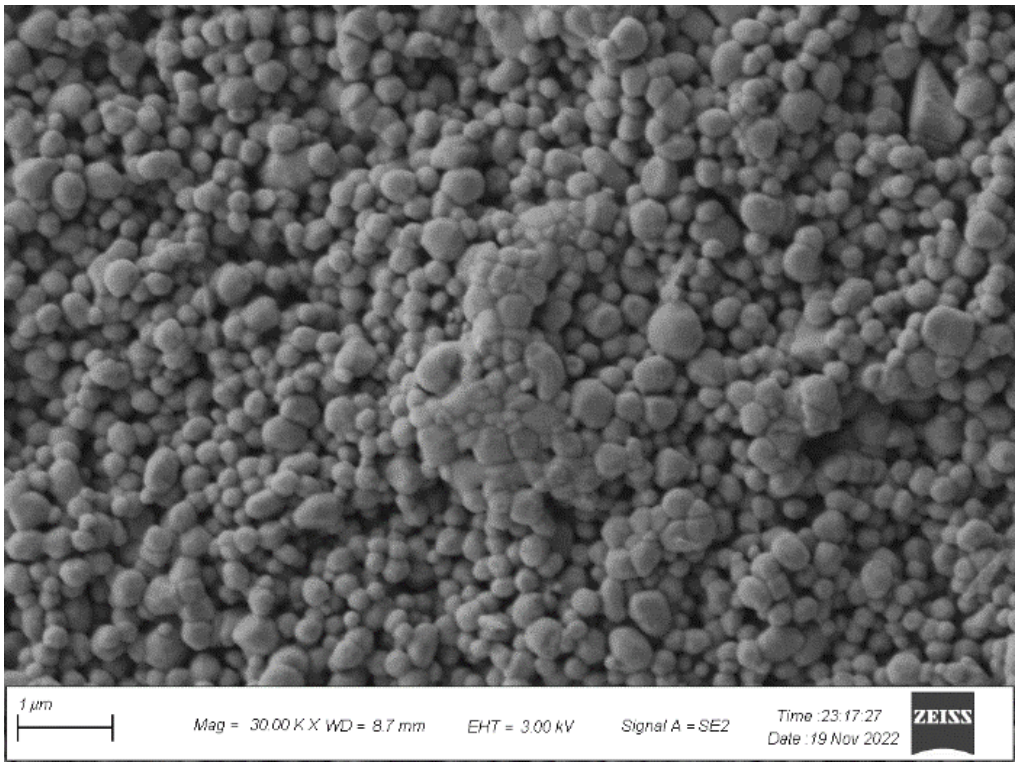

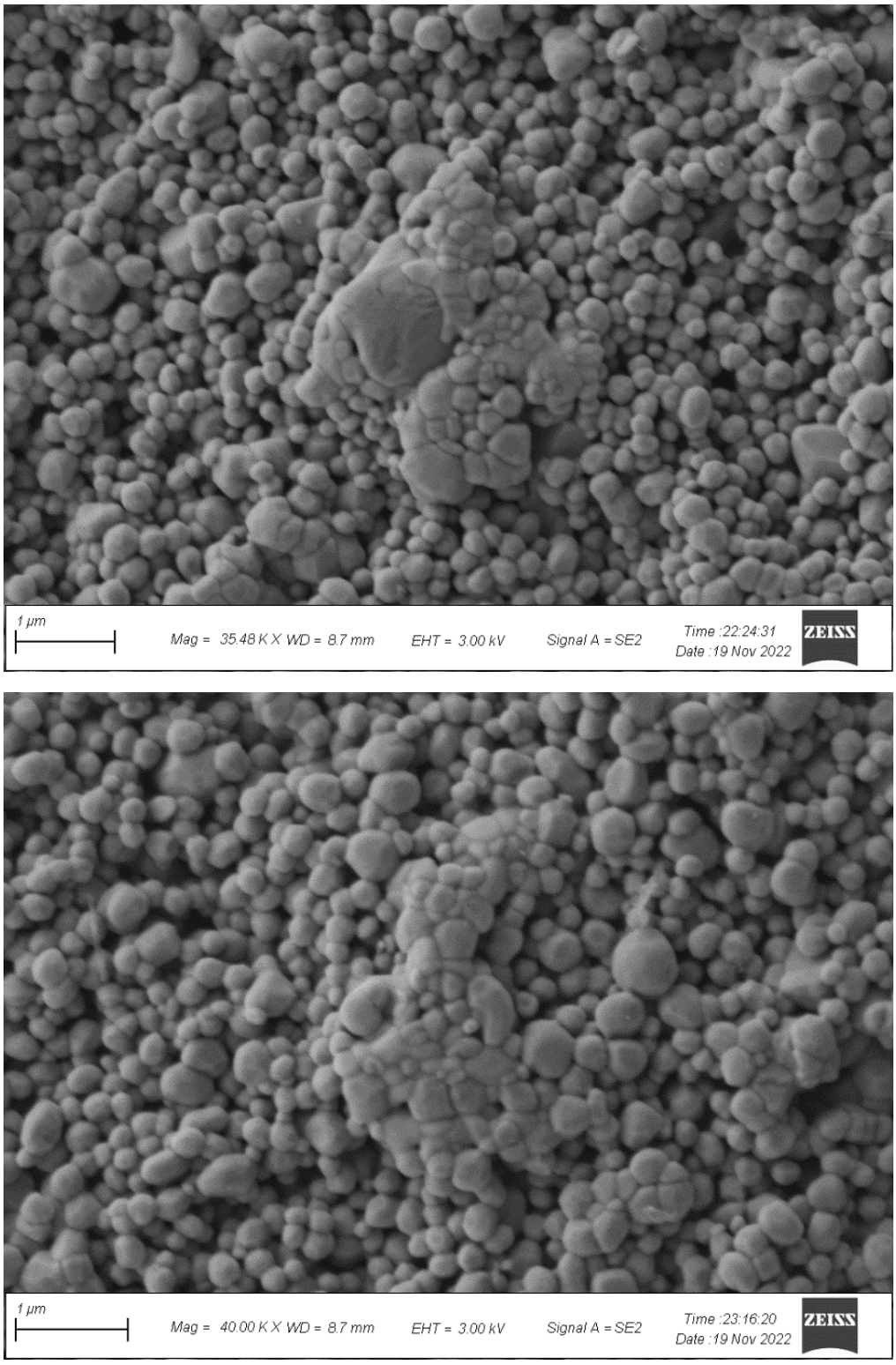

Figure B. 1. Al_2O_3 doped with 10,000 ppm CaO in different magnification sintered at 1300°C for 1 h.

B.2. Micrographs of the calcium doped α-Al_2O_3 sintered at 1300°C for 2 hours

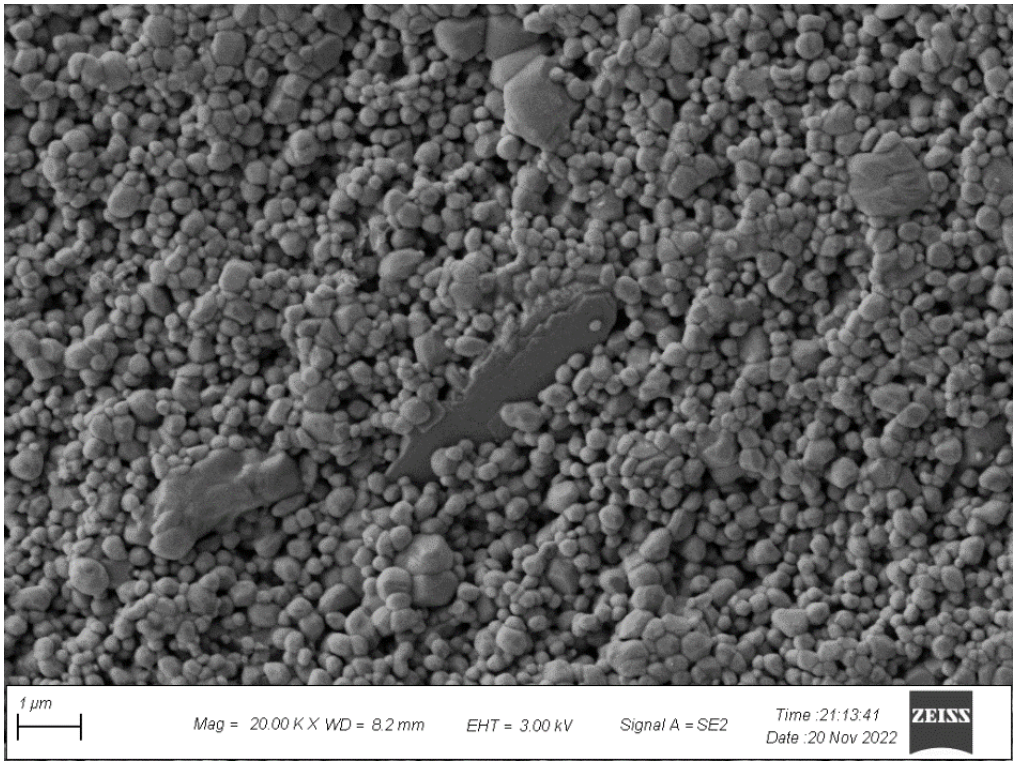

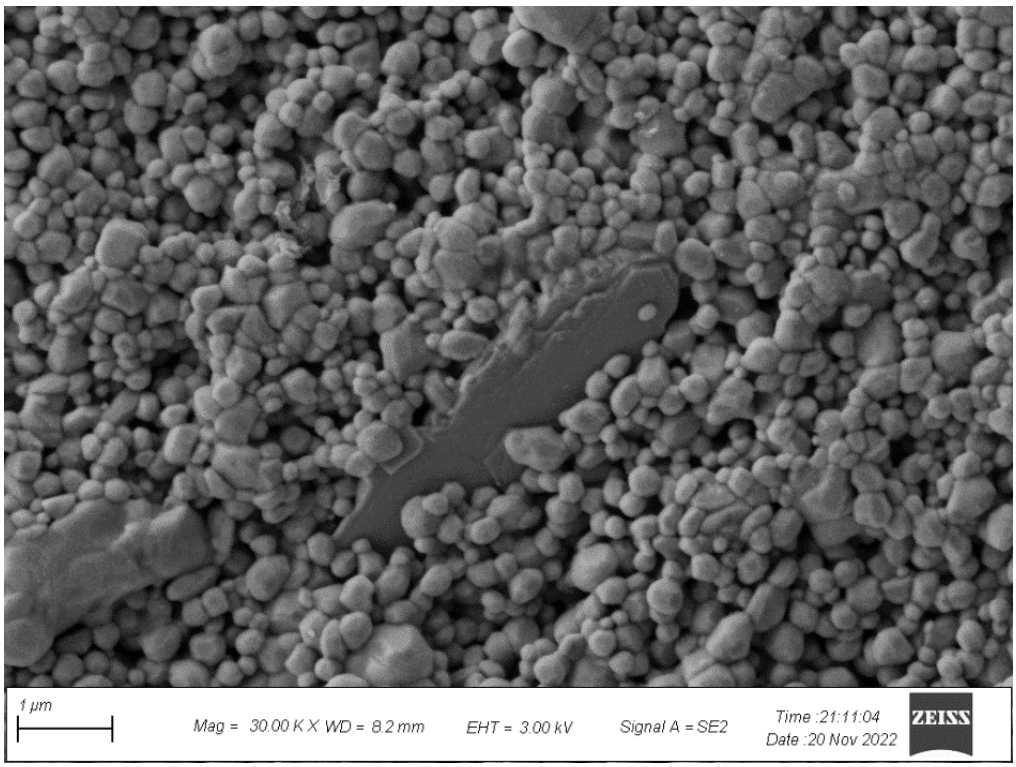

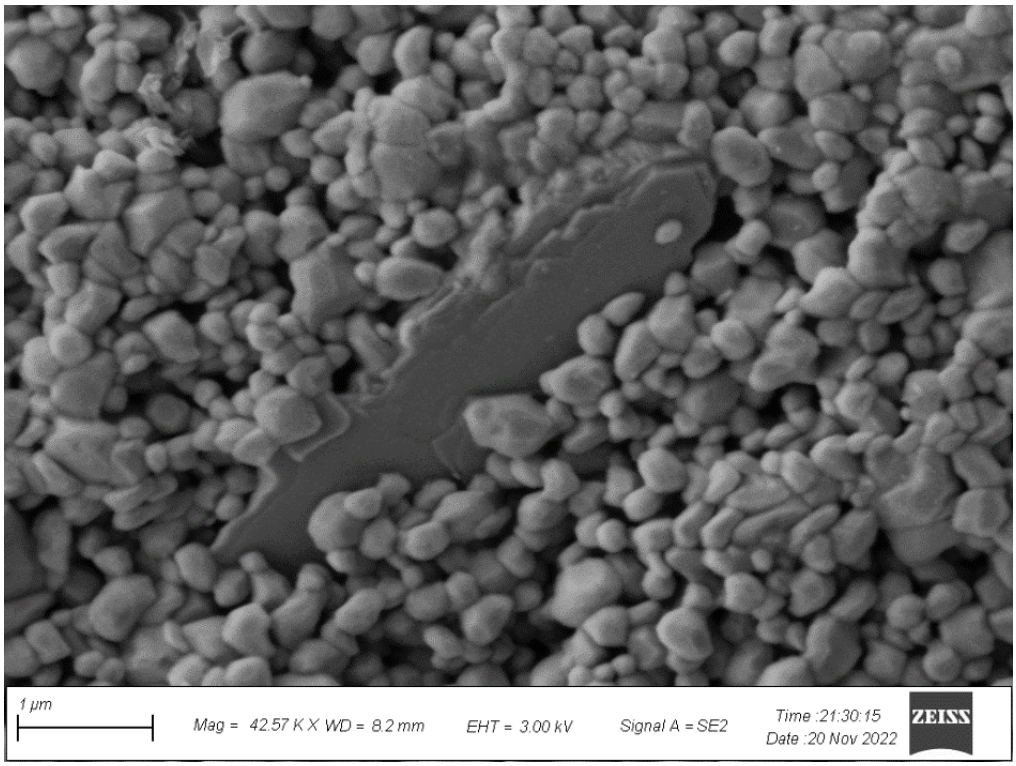

Figure B. 2. Al_2O_3 doped with 10,000 ppm CaO in different magnification sintered at 1300°C for 2 h.

B.3. Micrographs of the calcium doped α-Al_2O_3 sintered at 1300°C for 4 hours

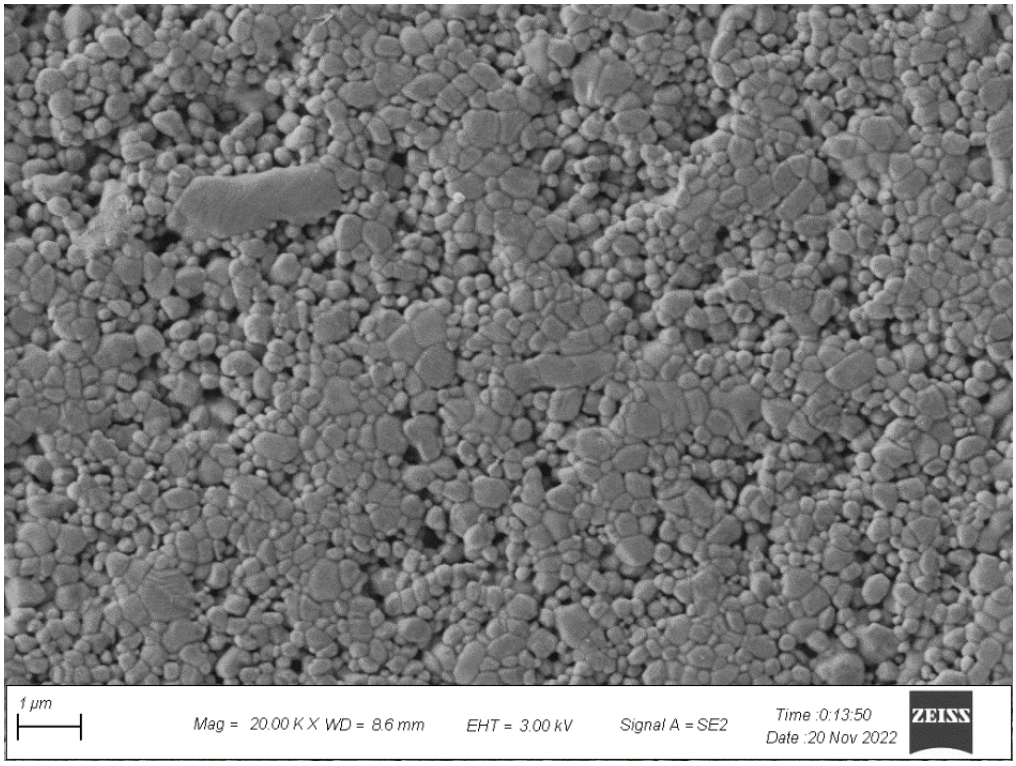

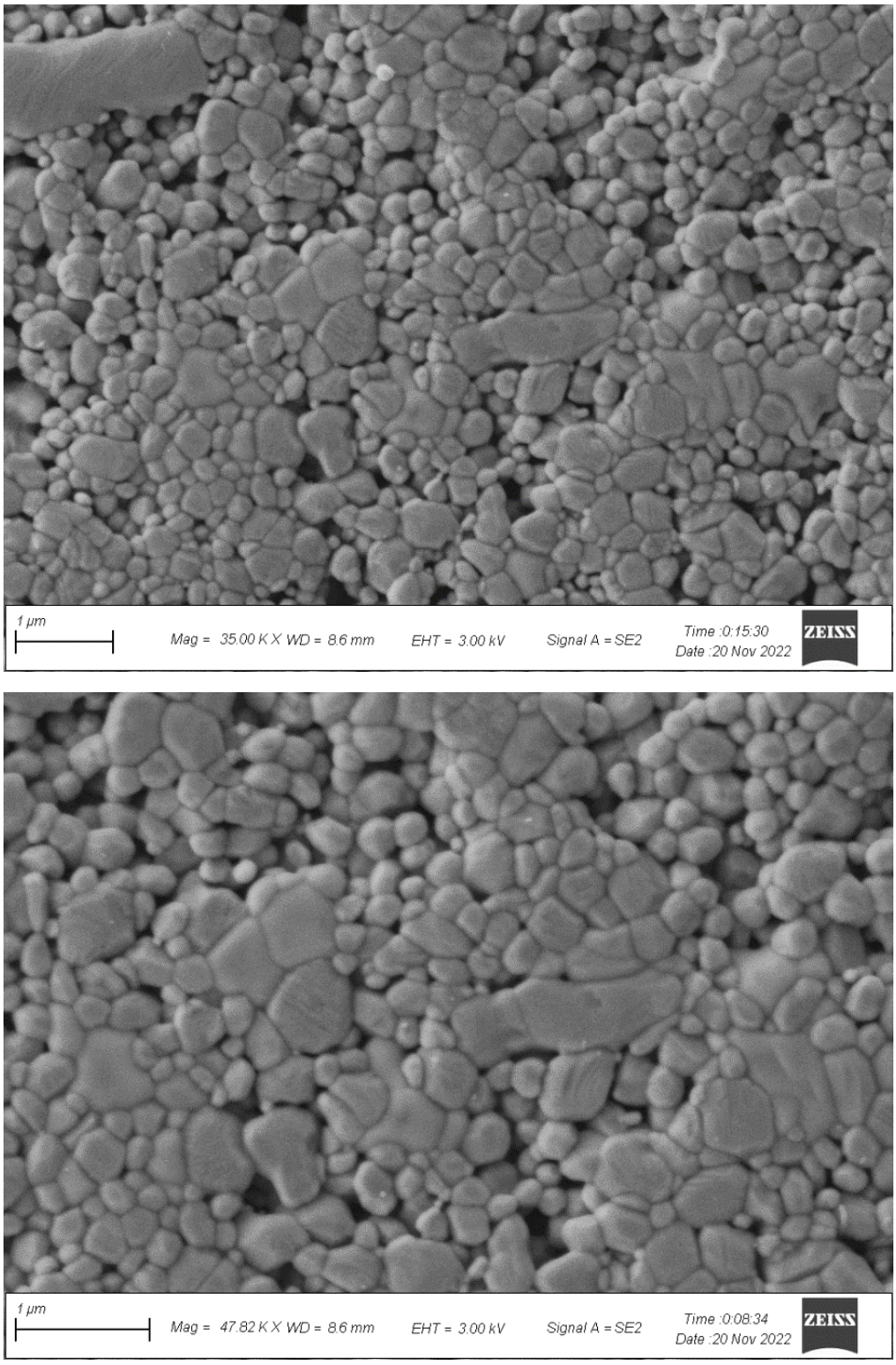

Figure B. 3. Al_2O_3 doped with 10,000 ppm CaO in different magnification sintered at 1300°C for 4 h.

B.4. Micrographs of the calcium doped α-Al_2O_3 sintered at 1300°C for 10 hours

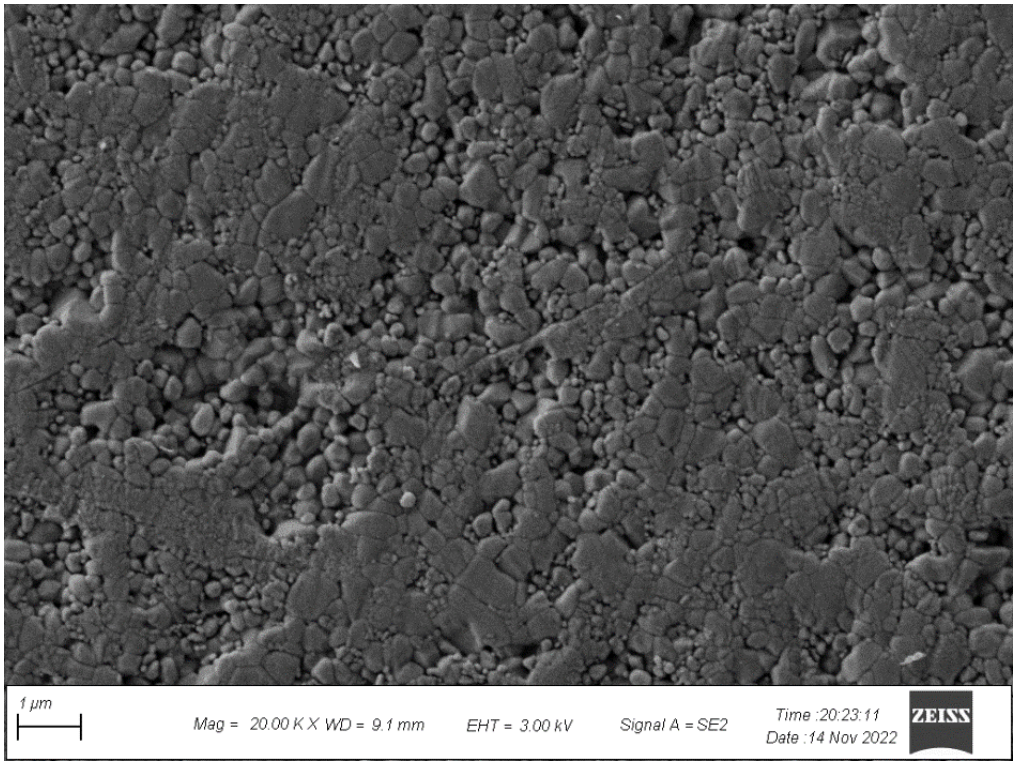

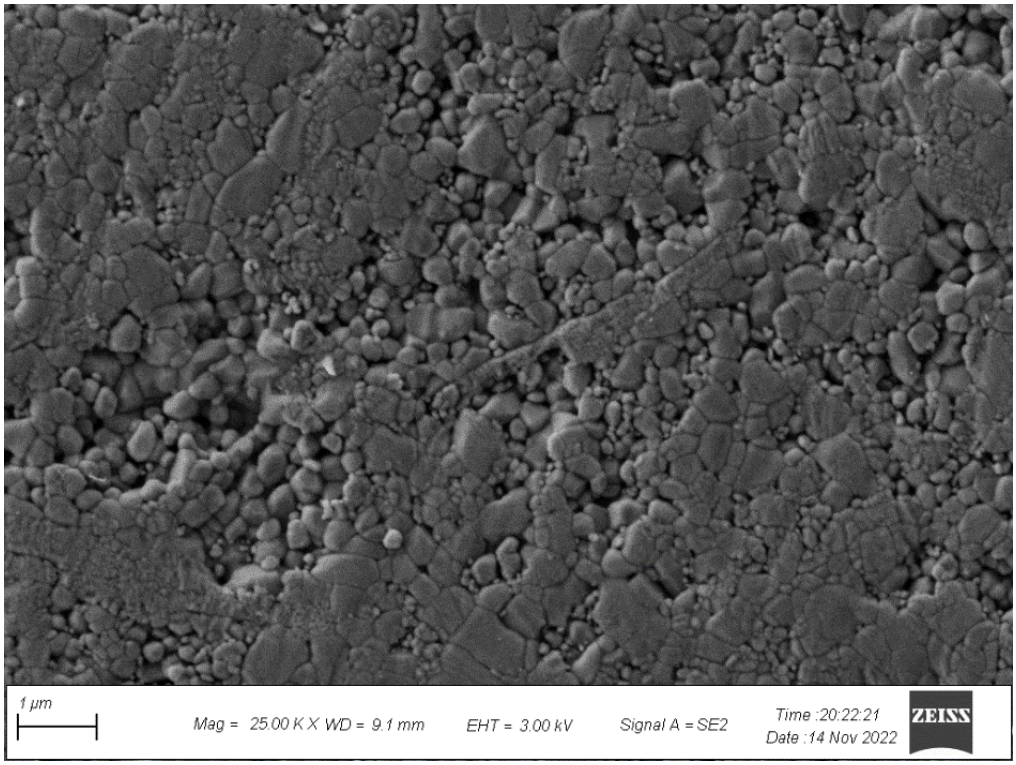

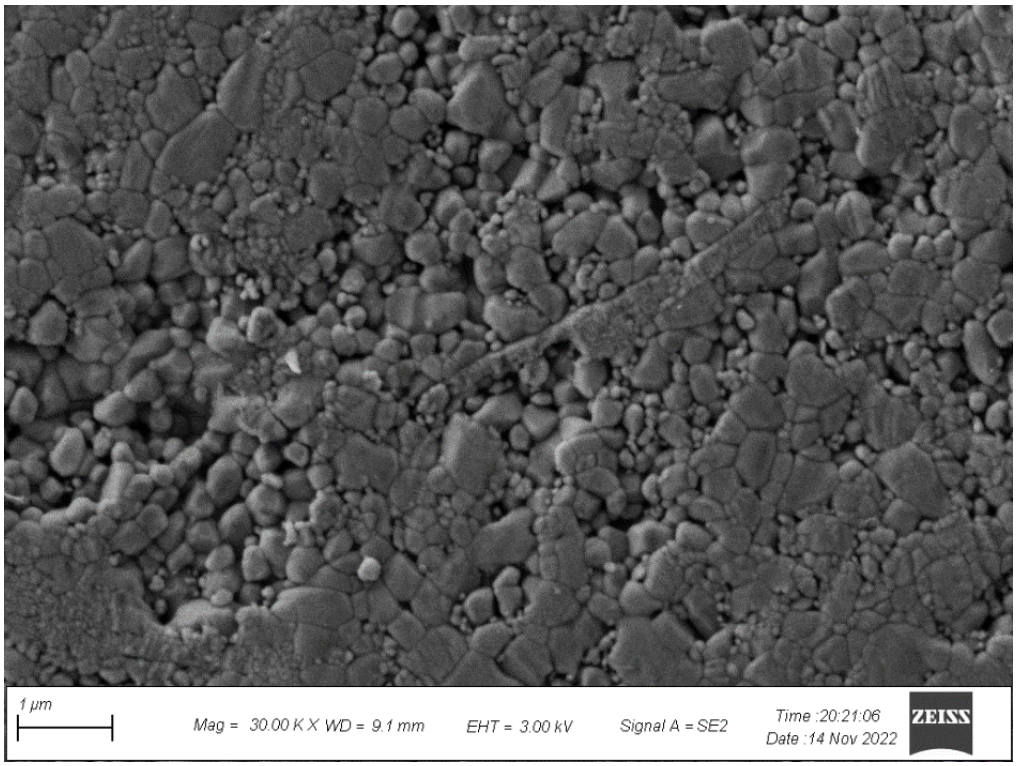

Figure B. 4. Al_2O_3 doped with 10,000 ppm CaO in different magnification sintered at 1300°C for 10 h.

B.5. Micrographs of the calcium doped α-Al2O3 sintered at 1400°C for 10 hours

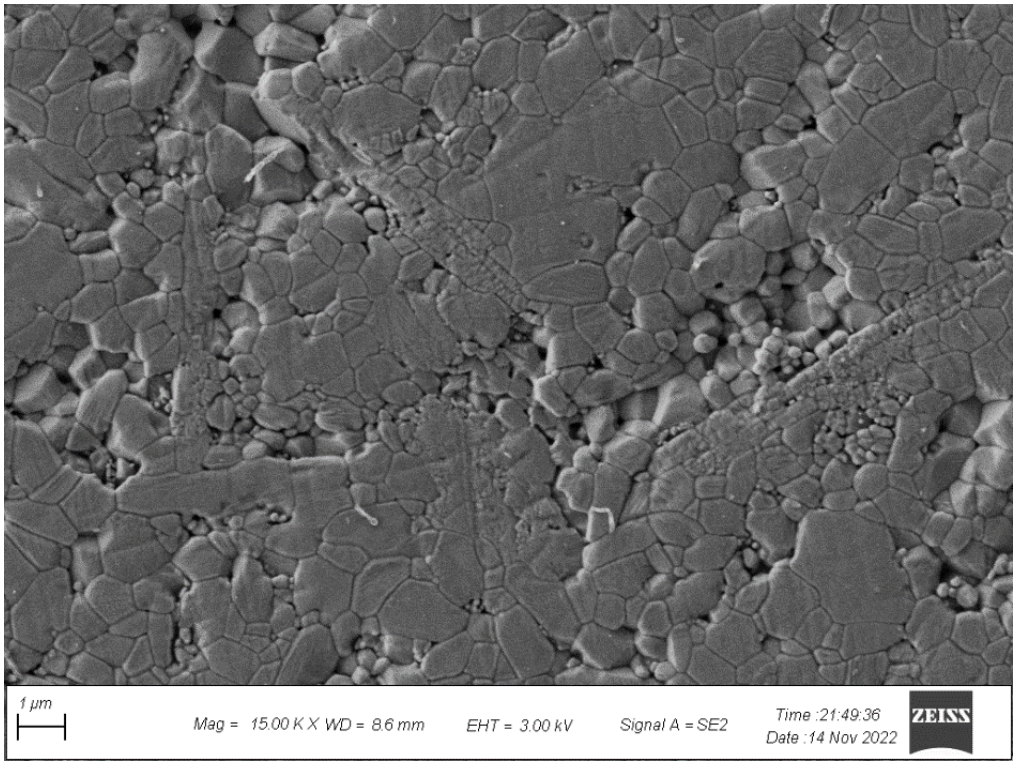

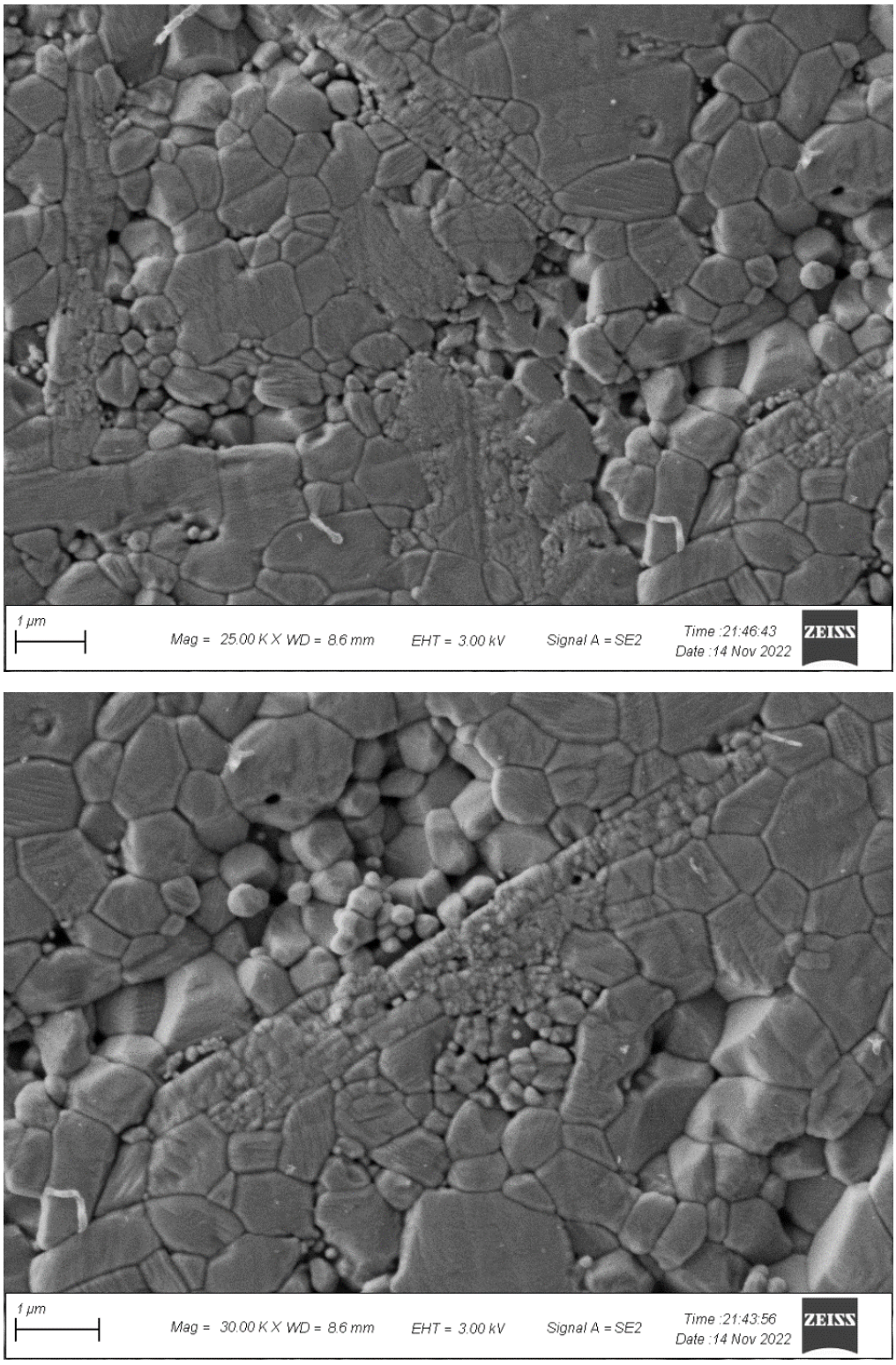

Figure B. 5. Al_2O_3 doped with 10,000 ppm CaO in different magnification sintered at 1400℃ for 10 h.

B.6. Micrographs of the calcium doped α-Al_2O_3 sintered at 1550°C for 10 hours

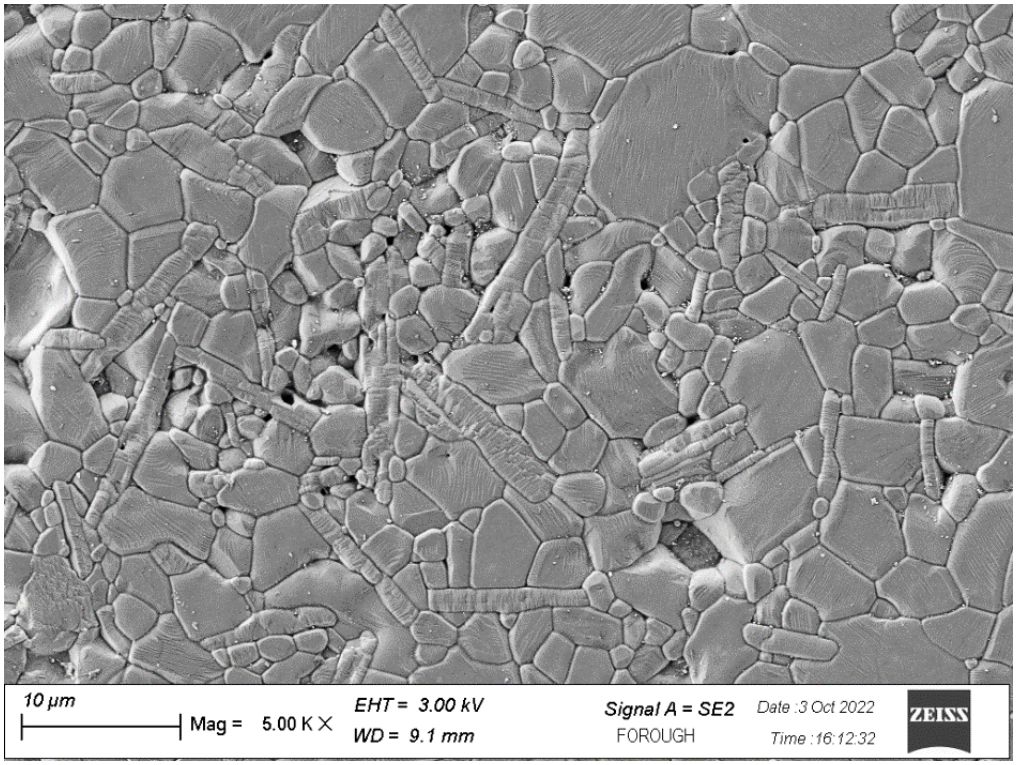

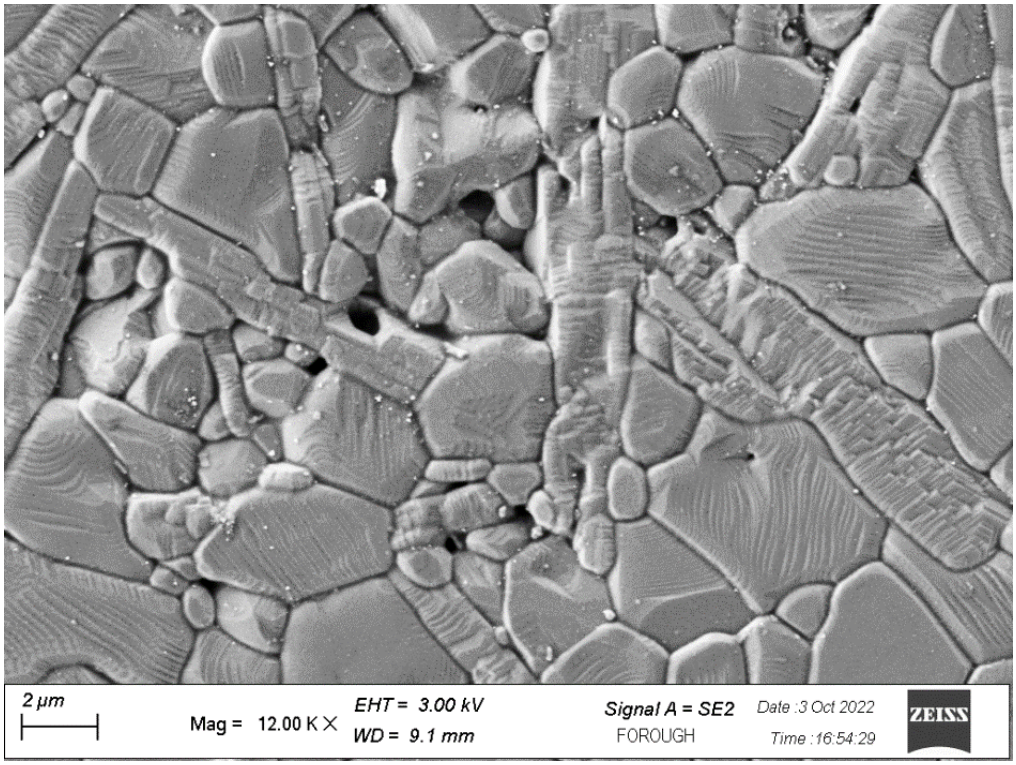

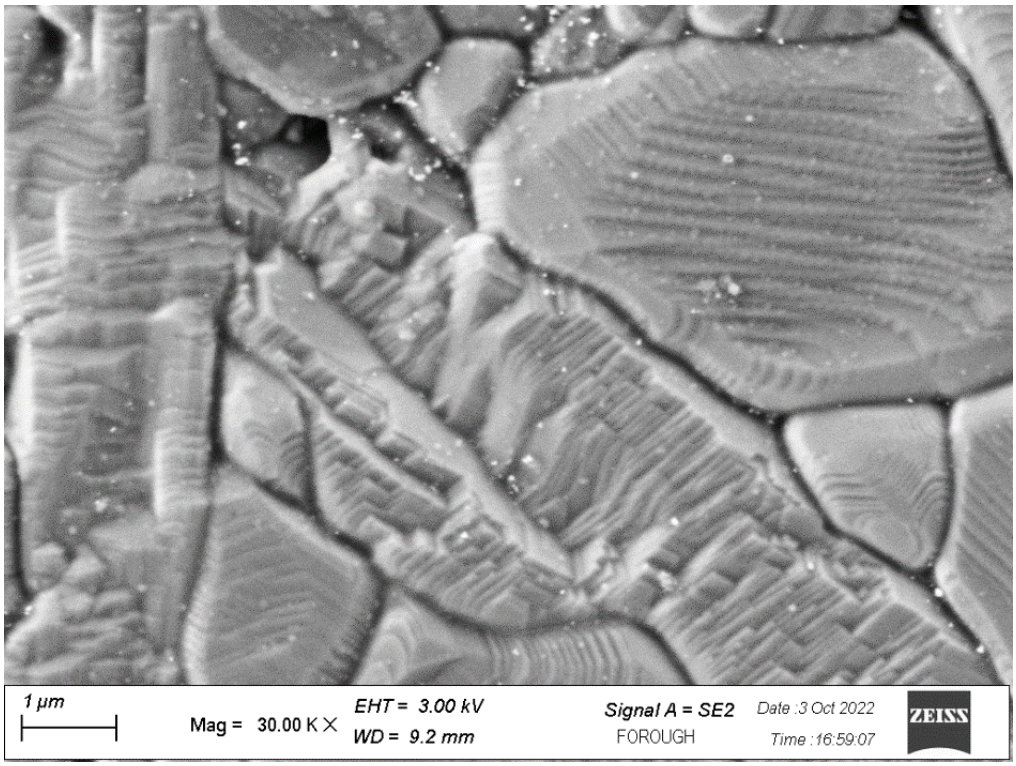

Figure B. 6. Al_2O_3 doped with 10,000 ppm CaO in different magnification sintered at 1550°C for 10 h.